Studies on Prediction of Gas Entrainment Inception in Hot Pool of Liquid Metal Fast Reactors

By

KAMALAKANTA SATPATHY

Enrolment number: PHYS02200704003

Indira Gandhi Center for Atomic Research, Kalpakkam, India

A thesis submitted to the Board of Studies in Physical Sciences
In partial fulfillment of requirements
For the Degree of

DOCTOR OF PHILOSOPHY

of

HOMI BHABHA NATIONAL INSTITUTE
MUMBAI, INDIA

July, 2012

HOMI BHABA NATIONAL INSTITUTE

Recommendations of the Viva Voce Board

As members of the Viva Voce Board, we certify that we have read the dissertation prepared by **Mr. Kamalakanta Satpathy** entitled **"Studies on Prediction of Gas Entrainment Inception in Hot Pool of Liquid Metal Fast Reactors"** and recommend that it may be accepted as fulfilling the dissertation requirement for the Degree of Doctor of Philosophy.

____ Date: **4th Jan 2013**

Chairman: **Dr. R.S. Keshavamurthy**

____ Date: **4th Jan 2013**

Guide/Convener: **Dr. K. Velusamy**

____ Date: **4th Jan 2013**

Member 1: **Dr. B.P.C. Rao**

____ Date: **4th Jan 2013**

Member 2: **Dr. P.Ch. Sahu**

____ Date: **4th Jan 2013**

External Examiner: **Prof.T. Sundararajan,**
Head, Mech. Engg. Dept., IIT-Madras

Final approval and acceptance of this dissertation is contingent upon the candidate's submission of the final copies of dissertation to HBNI.

I hereby certify that I have read this dissertation prepared under my direction and recommend that it may be accepted as fulfilling the dissertation requirement.

Date:

Place: Indira Gandhi Centre for Atomic Research (IGCAR) **Dr. K. Velusamy**
Kalpakkam **(Guide)**

STATEMENT BY AUTHOR

This dissertation has been submitted in partial fulfillment of requirements for an advanced degree at Homi Bhaba National Institute (HBNI) and is deposited in the library to be made available to borrowers under rules of the HBNI.

Brief quotations from this dissertation are allowable without special permission, provided that accurate acknowledgement of source is made. Requests for permission for extended quotation from or reproduction of this manuscript in whole or in part may be granted by the Competent Authority of HBNI when in his or her judgment the proposed use of the material is in the interests of scholarship. In all other instances, however, permission must be obtained from the author.

Kalpakkam **(Kamalakanta Satpathy)**

July 2012

DECLARATION

I, hereby declare that the investigation presented in the thesis has been carried out by me. The work is original and has not been submitted earlier as a whole or in part for a degree / diploma at this or any other Institution / University.

Kalpakkam **(Kamalakanta Satpathy)**
July 2012

Dedicated to

My Beloved Parents

A space for

My Brother, Sisters & friend Sanjit

ACKNOWLEDGEMENT

Every piece of work done by an individual is a result of direct or indirect support and help of many others. I take this opportunity to acknowledge the people who helped me during my doctoral studies. First and foremost, I would like to express my deep and sincere gratitude to my guide **Dr. K. Velusamy**, *Head, Mechanics and Hydraulics Division, Reactor Design Group, IGCAR* for his constant encouragement, caring, and insightful guidance in all the ways leading to the completion of my PhD work. His intellect and friendliness have made my research life more smooth and enjoyable. I specially thank him a lot and place my admiration on record.

I would like to acknowledge and extend my heartfelt gratitude to **Dr. B.S.V. Patnaik,** *Associate Professor, Dept. of Applied Mechanics, IIT-Madras* for his consistent and invaluable guidance through out the thesis period without which I couldn't have learnt and he never accepted anything less than my best efforts.

I convey my sincere gratitude to **Dr. P. Chellapandi**, *Director, RDG* for his constant support throughout the research. I thank **Shri S.C. Chetal**, *Director*, *IGCAR* for providing me the opportunity to continue the research work at IGCAR. I do appreciate the amenities and environment created by *former Director* **Dr. Baldev Raj,** towards pursuing high-end research. I thank **Shri P. Selvaraj**, *Associate Director, RAG* for facilitating the official activities. I convey my sincere thanks to **Dr. M. Sai Baba**, *Associate Director*, *RMG* for his support and constant encouragement.

I am deeply indebted to my *DC Members* (**Dr. B.P.C. Rao, Dr. R.S. Keshavmurthy, Dr. P. Ch. Sahu, Dr. P. Mohankrishnan, and Dr. P.V. Sivaprasad**) towards timely reviewing the thesis work and giving insightful suggestions and advice. I would like to express my deep thanks to **Mr. M. Asokkumar**, *SO(G), THS* for his suggestions, advices and timely tough warnings. I would like to thank **Dr. D.K. Mohapatra** for his friendly support and advice.

I express my sincere gratitude to all the teachers taking classes during the course work. Especially my sincere thanks to **Prof. T. Sundararajan** (*IIT-Madras*), **Dr. S. Tiwari** (*IIT-Madras*), **Mr. M. Valsakumar**, **Dr. H.K. Sahu**, **Dr. S.B. Koganti**, **Mr. S. Kanmani**, **Dr. S. Sivakumar** and **Dr. R. Harish**.

I gratefully acknowledge **Mr. M. Rajendrakumar, Mr. Juby Abraham** and **Mr. R. Arul Bhaskar** for their valuable contributions. I sincerely appreciate their kind help and sharing their scientific and technical knowledge through discussions and suggestions.

I thank to all members of Thermal Hyadraulics Section especially **Mr. Ram Kumar Maity, Mr. N. Govinda Rasu, Mr. L. Ravi, Shri G.R. Raviprasan, Mr. T. Ramakrishna** and **Mr. Chetan Verma** for their help. I owe a lot to my friends **Gagan, Som, Hemant, Patidar** and **Sajith** for their intuitive observations and support. I also thank my friends **Sridhar, Prakash, Amit, Vijay, Sam, Hanuma, Manish, Paresh, Sourabh, Vittal** and **Rajesh Panda** for their kind help during my stay at IIT-Madras.

I would also like to acknowledge **Smt. R. Vijayashree** and **Mr. P.A. Sasidharan** for providing the advanced computational facility at Samdo Lab, RDG. I am also thankful to **Mr. A. Satyamurty**, *Head, Computer Division*, for the High Performance Scientific Computing facility. I also got full support from library and computer center staffs.

My special thank to **Asit, Alok, Baban, Bishnu, Biranchi, Jayaganesh, Kalpataru, Mahendra, Padhy, Prasana, Pravat, Pradeep, Satyaprakash, Satendar, Saratchandra, Srinivas and Sunasira**. My sincere gratitude to all my former and present fellow research scholars for making my life more cheerful during my stay at JRF Enclave, Kalpakkam.

Last but not the least, I would like to express my heartiest gratitude and honor to my family members and friends who are with me during the ups and downs of my life. Finally I thank the Almighty for His blessings bestowed on me which enabled to complete the thesis.

Kamalakanta Satpathy

CONTENTS

Title	Page No
SYNOPSIS	v - vii
LIST OF FIGURES	viii - xi
LIST OF TABLES	xii
CHAPTER 1 INTRODUCTION	**1 - 12**
1.0 FOREWORD	2
1.1 NEED FOR FAST BREEDER TECHNOLOGY	3
1.2 DESCRIPTION OF POOL TYPE LMFBR	4
1.3 THERMAL HYDRAULICS ISSUES OF LMFBR	7
1.4 MOTIVATION FOR THE PRESENT RESEARCH	10
1.4.1 Difficulties in Numerical Prediction	10
1.4.2 Difficulties in Experimental Simulation	10
1.5 OBJECTIVE AND SCOPE OF THE PRESENT WORK	11
1.6 ORGANIZATION OF THE THESIS	12
CHAPTER 2 LITERATURE REVIEW	**13 - 23**
2.0 FOREWORD	14
2.1 FUNDAMENTAL EXPERIMENTS	14
2.1.1 Liquid-Fall Induced Entrainment	14
2.1.2 Formation of Drain-Type Vortices	15
2.1.3 Vortex Activated Entrainment	17
2.1.4 Shearing of Free Surface	18
2.2 NUMERICAL STUDIES	21
2.3 CLOSURE	23
CHAPTER 3 MATHEMATICAL FORMULATION	**24 - 42**
3.0 FOREWORD	25
3.1 OVERVIEW OF COMPUTATIONAL FLUID DYNAMICS (CFD)	25
3.2 GOVERNING EQUATIONS	26
3.3 AN OVERVIEW OF TURBULENCE MODELS	27
3.3.1 Filtering	28
3.3.2 Reynolds Averaging	28
3.3.2.1 Eddy-Viscosity Model	28
3.3.2.2 Reynolds Stress Models	30
3.3.2.3 Detached Eddy Simulation (DES)	30
3.3.2.4 Reynolds Averaged Equations For Turbulent Flow	30

3.3.2.4.1 The Standard k-ε model 31
3.3.2.4.2 RNG k-ε model 33
3.3.2.4.3 k-ω turbulence model 33
3.3.2.4.4 Shear stress transport (SST) k-ω model 34
3.4 FREE SURFACE MODELLING 35
3.4.1 Methods for Solving Free Surface Phenomena 36
3.4.1.1 Surface Height Method 36
3.4.1.2 Marker and Cell (MAC) Method 37
3.4.1.3 Level Set Method 38
3.4.1.4 Front Tracking Method 39
3.4.1.5 Volume-Of-Fluids (VOF) Method 39
3.4.1.6 Line Interface Technique 41
3.5 BOUNDARY CONDITIONS 41
3.6 GRID INDEPENDENCE TEST AND CONVERGENCE 42
3.7 CLOSURE 42

CHAPTER 4 NUMERICAL STUDIES ON LIQUID FALL INDUCED GAS ENTRAINMENT 43 - 60
4.0 FOREWORD 44
4.1 SOLUTION METHODOLOGY 45
4.1.1 Governing Equations 45
4.1.2 Validation for the interface dynamics 48
4.2 ESTABLISHMENT OF FREE SURFACE VELOCITY LIMIT 50
4.2.1 A 2-D Model Problem 50
4.2.2 Dynamic Evolution of Gas Entrainment 52
4.2.3 Inception of Entrainment 53
4.2.4 End of Entrainment 55
4.2.5 Parameters Influencing Gas Entrainment 56
4.3 SENSITIVITY ANALYSIS 57
4.4 VERIFICATION OF THE CRITERION IN FIXED GRID SIMULATION 57
4.5 SIMULATIONS ON 3-D MODELS 59
4.6 CLOSURE 60

CHAPTER 5 IDENTIFICATION OF A PASSIVE DEVICE FOR REACTOR HOT POOL 61 - 75
5.0 FOREWORD 62
5.1 COMPUTATIONAL MODEL PFBR HOT POOL 63
5.2 COMPUTATIONAL DETAILS 64
5.3 GRID INDEPENDENCE STUDY 65

5.4	VALIDATION AGAINST EXPERIMENTS	65
5.5	SODIUM FLOW DISTRIBUTION IN PFBR HOT POOL	68
5.6	MITIGATION STRATEGY FOR GAS ENTRAINMENT	70
5.7	CLOSURE	75
CHAPTER 6	**FLOW PAST A FINITE SIZED CIRCULAR CYLINDER MOUNTED ON A FLAT PLATE**	**76 - 107**
6.0	FOREWORD	77
6.1	OVERVIEW OF FLOW AROUND A CIRCULAR CYLINDER	78
6.1.1	Vortex Shedding and Strouhal Number	80
6.1.2	Drag and Lift Coefficients	80
6.1.3	Pressure Coefficient	82
6.2	SIMULATION OF FLOW PAST A CIRCULAR CYLINDER AT LOW REYNOLDS NUMBER	83
6.2.1	Governing Equations	85
6.2.2	Initial and Boundary Conditions	85
6.2.3	Numerical Approach	87
6.3	RESULTS AND DISCUSSION	88
6.3.1	Simulation of Flow Past a Circular Cylinder	88
6.3.2	Grid Sensitivity Check	88
6.3.3	Validation of Unsteady Wake Characteristics	90
6.4	FINITE ASPECT RATIO EFFECTS OF FLOW PAST A CIRCULAR CYLINDER	91
6.4.1	Forces on the Circular Cylinder	92
6.4.2	Capturing Horseshoe Vortex	96
6.4.3	Suppression of Vortex Shedding	101
6.5	FLOW PAST 3D CYLINDER WITH ACCELERATED BOTTOM	103
6.6	CLOSURE	106 - 107
CHAPTER 7	**INVESTIGATION OF TURBULENT VORTEX SHEDDING PAST A FINITE CIRCULAR CYLINDER MOUNTED ON A FLAT PLATE**	**108 - 120**
7.0	FOREWORD	109
7.1	SOLUTION METHODOLOGY	112
7.1.1	Governing Equations	112
7.1.2	Initial and Boundary Conditions	112
7.2	RESULTS AND DISCUSSION	113
7.2.1	Simulation of 2D Flow past a Circular Cylinder	113
7.2.2	Grid Sensitivity Check	113
7.2.3	Validation of Unsteady Wake Characteristics	114
7.2.4	Finite Aspect Ratio Effects of Flow past a Circular Cylinder	116

7.2.4.1 Forces on the Circular Cylinder 116
7.2.4.2 Vorticity Contours 117
7.2.4.3 Capturing Horseshoe Vortex 118
7.3 CLOSURE 120

CHAPTER 8 INVESTIGATION OF GAS ENTRAINMENT IN THE HOT POOL FREE SURFACE DURING CROSS FLOW OVER A CYLINDRICAL COMPONENT 121 - 134
8.0 FOREWARD 122
8.1 GOVERNING EQUATIONS 124
8.1.1 Validation of VOF Problem 124
8.1.2 Initial and Boundary Conditions 126
8.2 RESULTS AND DISCUSSION 127
8.2.1 Flow past a Free Surface Piercing Circular Cylinder 127
8.2.2 Grid Sensitivity Check 127
8.2.3 Dynamics of Free Surface Characteristics 129
8.2.3.1 Interface Interactions 129
8.2.3.2 Time Average 130
8.3 CLOSURE 133 - 134

CHAPTER 9 CONCLUSIONS AND SCOPE FOR FUTURE STUDIES 135 - 139
9.0 FOREWORD 136
9.1 NUMERICAL STUDIES ON LIQUID FALL INDUCED GAS ENTRAINMENT 136
9.2 IDENTIFICATION OF A PASSIVE DEVICE FOR REACTOR HOT POOL 136 - 137
9.3 LAMINAR FLOW PAST A FINITE SIZED CIRCULAR CYLINDER MOUNTED ON A FLAT PLATE 137
9.4 TURBULENT VORTEX SHEDDING PAST A FINITE CIRCULAR CYLINDER MOUNTED ON A FLAT PLATE 137 - 138
9.5 INVESTIGATION OF GAS ENTRAINMENT IN THE HOT POOL FREE SURFACE DURING CROSS FLOW OVER A CYLINDRICAL COMPONENT 138
9.6 SCOPE FOR FUTURE WORK 138 - 139
REFERENCES 140 - 151
NOMENCLATURES 152-153
PUBLICATIONS 154 - 155

SYNOPSIS

In Fast Breeder Reactor (FBR), the sodium pool is blanketed by inert argon cover gas, to avoid deleterious effects. Due to compact layout of reactor system, sodium velocity in the pool is generally high. This results in a local fluid swell in the pool and vortex formation around reactor components that are partially submerged in sodium and partially exposed to argon gas. These are the primary sources of argon entrainment into liquid sodium, which is an important safety problem in nuclear industry. The major focus of the present work is to identify the free surface criteria for onset of gas entrainment and its mitigation.

Governing mass, momentum conservation equations are solved using Computational Fluid Dynamics (CFD) tools to investigate both ideal and practically relevant hot pool models. To investigate the dynamics of free surface and argon gas entrainment, Volume of Fluids (VOF) method has been employed. By performing systematic 2-D and 3-D VOF simulations, liquid fall induced entrainment is found to depend on the free surface velocity, re-submergence angle and a modified Froude number (Fr^*). It was found that, gas entrainment into reactor hot pool is possible, if the value of Fr^* exceeds 2.0. The free surface velocity in sodium to avoid gas entrainment during liquid fall is found to be ~ 0.41 m/s.

Following 2-D studies, 3-D CFD studies have been carried out on reference reactor hot pool and the highest free surface velocity has been estimated to be about 1.15 m/s. As, such a high free surface velocity is conducive to argon gas entrainment, steps to mitigate this value have been proposed. To this end, a horizontal circumferential baffle plate has been proposed as a passive solution. A systematic study of baffle depth and width was conducted and an optimal configuration was reached for a baffle width of 0.5

m, at a depth of 1.3 m from the free surface. The suggested configuration has brought down the free surface velocity, to within acceptable limit. The CFD results are validated against published 1/4th scale water model tests.

In order to understand the gas entrainment due to vortex activation, laminar flow past circular cylinder mounted on a flat or an accelerated bottom plate is numerically investigated. The influence of bed friction on the junction flow between the plate and the circular cylinder results in the formation of horseshoe vortex system. Streamwise and transverse forces on the cylinder are determined to study the finite size effects, for different liquid depths. Parametric study is conducted for cylinder aspect ratios (H/D) = 0.5, 1.0, 2.0, 5.0, and 10.0 at Re = 200. Vortex shedding is completely suppressed for cylinder heights below H/D ≤ 1.0, due to interaction between the horseshoe vortex at the junction and vortex formation region of the cylinder. Although horseshoe vortex is present for all H/D values, the unsteady wake characteristics are not affected for H/D ≥ 2.0, where vortex shedding still prevails at different spanwise heights. Accelerated bottom wall is seen to increase the free surface velocity without affecting the vortex shedding process. Subsequently, turbulent vortex shedding past cylindrical bodies is investigated by various turbulence models and the SST k-ω model is seen to perform better than the other competing models that were tested.

Interactions between free surface waves and underlying viscous wake are investigated for a turbulent flow past a free surface piercing circular cylinder for different ranges of Reynolds and Froude numbers, using the SST k-ω model and the VOF technique. The computational results show that the free surface inhibits the vortex generation in the near wake thereby reducing the vorticity and vortex shedding near the interface for all range of Froude numbers. Organized vortex shedding, which is very similar to that from an infinitely long cylinder in a single phase flow, is observed in the deep flows. For various inflow velocities, the re-submergence angle and the free surface velocity at the point where the surface slope changes abruptly are measured. It is found that, for $Fr_D \leq 0.5$, there is no risk of entrainment due to vortex activation

LIST OF FIGURES

Figure No	Figure Title	Page No
1.1	Flow sheet of pool type fast breeder reactor.	4
1.2	Vertical section of reactor assembly of LMFBR.	5
1.3	Different parts of Control Plug.	8
1.4	Schematic of various types of gas entrainment mechanisms that may occur in nuclear reactor: (a) vortex activated gas entrainment, (b) liquid fall induced gas entrainment, (c) drain-type gas entrainment and (d) shear induced gas entrainment.	9
3.1	Various discretisation methods.	26
3.2	An overview of various turbulence models.	27
3.3	Schematic representation of marker and cell (MAC) mesh layout [12].	37
3.4	Volume fraction on a discrete mesh [15].	39
3.5	Various line interface techniques, (a) a true interface, (b) SLIC and (c) PLIC [78].	41
4.1	Computational domain.	47
4.2	Computed pressure jump.	47
4.3	Schematic of the broken dam problem.	49
4.4	Water-air interface at various time steps.	49
4.5	Reduction of water level on the left boundary as a function of time.	50
4.6	Distance traveled by the interface front.	50
4.7	Idealized flow domain of interest with geometric details for 2-D studies.	51
4.8	Different phases of gas entrainment. Air-water interface is captured using VOF technique: (a) Initial time, (b-c) gas entrainment and (d) no entrainment case.	53
4.9	Dependence of re-submergence angle on free surface velocity.	55
4.10	Variation of re-submergence angle as a function of Fr^*.	56
4.11	Sensitivity analysis for liquid properties.	57
4.12	Velocity vectors at the inception of entrainment (a) fixed grid simulation and (b) 2-D VOF simulation.	58
4.13	Velocity vectors at the end of entrainment (a) fixed grid simulation and (b) 2-D VOF simulation.	58
4.14	3-D numerical simulations using VOF method (a) front face, (b) middle face and (c) rear face of the rectangular tank indicating gas entrainment into the liquid.	59

5.1	3-D computational domain and global grid pattern of 90° sector model of PFBR hot pool: (a) isometric view and (b) sectional front view (red dotted line shows the ideal slab model considered for 2-D simulation). Note in particular, the location of a circumferential baffle.	64
5.2	Velocity (m/s) distribution at the free surface for 1/4th scale model (a) present numerical simulation and (b) experimental measurements of Banerjee et al., [87].	66
5.3	Cross flow velocity distribution along IHX inlet window at various reference locations: (a) 0°, (b) 90°, (c) 180° and (d) 270°.	67
5.4	Measurement locations around IHX inlet window and side view indicate the height along IHX inlet window.	67
5.5	Sodium velocity in PFBR hot pool (m/s): (a) at the free surface and (b) at a section through IHX.	68
5.6	Vertical distribution of resultant velocity along IHX inlet window at an angle of 225°.	69
5.7	(a) Turbulence kinetic energy (m^2/s^2) and (b) eddy viscosity (N-s/m^2) at the free surface of PFBR hot pool.	69
5.8	Hot pool velocity field with 125 mm baffle positioned at different depths from the free surface: (a) at free surface (b) at a depth of 0.5 m from free surface and (c) at 1.3 m depth from the free surface.	71
5.9	Baffle width effect on the velocity field in the hot pool when it is located at a depth of 1.3 m from the free surface: (a) 250 mm baffle (b) 500 mm and (c) 750 mm baffle.	72
5.10	Effect of free surface velocity against baffle width depicts possible optimal (as shown dotted lines) width for the configuration under investigation.	73
5.11	(a) Turbulence kinetic energy (m^2/s^2) and (b) eddy viscosity (N-s/m^2) for 0.5 m baffle width located at a depth 1.3 m from the free surface.	73
6.1	Development of three dimensional flows in the wake region [93]	79
6.2	Experimental visual of flow past a circular cylinder [94] at Re = 140, (T = time period).	80
6.3	Lift coefficient acting on a cylinder.	81
6.4	Drag coefficient of the flow around a circular cylinder [95].	81
6.5	Measured pressure coefficient distribution on the cylinder surface [95].	82
6.6	Flow past a pillar, depicting finite size effects (from Kawamura et al. [109]). In the junction between wake and boundary layer, a necklace vortex is formed. This vortex system interacts with the trailing edge vortices for shorter heights.	85
6.7	Flow domain of interest with boundary conditions.	86
6.8	Typical global grid pattern around the cylinder adopted for numerical simulation: (a). a view of the top surface and (b). close-up view that	89

depicts an O-type grid around the periphery of the cylinder.

6.9 Temporal variation of drag force coefficients to study grid sensitivity. 90

6.10 Instantaneous vorticity contours depicting one complete shedding cycle at Re = 200 (a-c) present simulation; (d-f) (Kalita & Ray [111]). 90

6.11 Temporal variation of drag and lift force coefficients after an organized, steady shedding is established. The simulations are performed for Re = 200. 91

6.12 Evolution of lift force coefficients on the cylinder for (a) H/D = 0.5, (b) H/D = 2, (c) H/D = 5 and (d) H/D = 10. 94

6.13 Evolution of drag force coefficients on the cylinder for (a) H/D = 0.5, (b) H/D = 2, (c) H/D = 5 and (d) H/D = 10. 95

6.14 Mean pressure coefficient at three different spanwise heights viz., z/D = 0.15, 0.35 and 0.94 for (a) H/D = 1 and (b) H/D = 2. 96

6.15 Streaklines at various span wise positions for H/D = 1 (left) and H/D = 2 (right): (a) z/D = 0.02, (b) z/D = 0.05, (c) z/D = 0.1, (d) z/D = 0.2, (e) z/D = 0.5, (f) z/D = 1 and (g) z/D = 1.95. 97

6.16 Horseshoe vortex visualized by hydrogen bubble visualization technique in (a) and (b) (source: Sumer & Fredsøe [120]), show a good comparison with the present numerical simulations in (c). 98

6.17 Time average velocity vectors along the vertical plane (y/D = 0) through the cylinder for H/D = 10, flow from left to right: (a) present simulation Re = 200 and (b) Marakkos & Turner [121] for Re = 5140. 99

6.18 Pathlines in a vertical plane (y/D = 0.01) on the upstream of the cylinder for H/D = 10: left (present simulation) and right (Marakkos & Turner [121] for Re = 5140). 100

6.19 Time averaged velocity distribution at various span wise positions for H/D = 10: (a) z/D = 0.01, (b) z/D = 0.02, (c) z/D = 1 and (d) z/D = 9. 101

6.20 3D streaklines along various span wise heights demonstrating vortex shedding suppression at H/D = 1.0. 101

6.21 3D streaklines along various spanwise heights demonstrating the presence of vortex shedding for H/D = 10. 102

6.22 Power Spectral Density from the fluctuating lift coefficient histories for different values of H/D. 102

6.23 Instantaneous static pressure distribution for different H/D values: (a) H/D = 1, (b) H/D = 2, (c) H/D = 5 and (d) H/D = 10 at same span wise location z/D = 0.25. Note in particular the absence of vortex shedding for H/D = 1. 103

6.24 Flow domain considered to access the effect of accelerated bottom. 104

6.25 Vorticity contours at different span wise positions along the axial length of the circular cylinder with bed friction for aspect ratio H/D = 10. 104

6.26	Comparison of velocity contours in a vertical plane (y/D = 0) through the cylinder for H/D = 10 (with bed friction) at Re = 200.	105
6.27	Streak lines released from different span wise heights (H/D=10). Left side represents the streak visualization for accelerated bottom where as right side represents for flat bottom (a) & (d) Z/D = 0.01, (b) & (e) Z/D =5 and (c) & (f) Z/D = 10.	106
7.1	Computational domain to study 3-D vortex shedding.	112 - 113
7.2	Typical global grid pattern around the cylinder adopted for numerical simulation: (a) a view of the top surface and (b) close-up view around the periphery of the cylinder.	114
7.3	Time averaged mean pressure coefficient distribution around the cylinder for different turbulence models.	115
7.4	Temporal variation of drag and lift force coefficients for Re = 4×10^4 (SST k-ω model).	117
7.5	Contours of voriticity at different spanwise heights at Re = 2×10^4 using different turbulence models.	117
7.6	Flow visualization: (a) Baker [107] at Re = 1.1×10^5 and (b) present streakline visualization for Re = 4×10^4 using SST k-ω model.	118
7.7	Time average velocity vectors along the vertical plane (y/D = 0) through the cylinder for H/D = 2, Re = 2×10^4.	119
7.8	Velocity vectors at Re = 2×10^4 predicted by SST k-ω model: (a) z/D = 1.95 and (b) z/D = 0.05.	120
8.1	Flow past a horizontal circular cylinder placed in a partially filled channel (b) streaklines around the cylinder at the interface for $h^* = 0$ and (c) velocity field for $h^* = 0.3$.	125
8.2	Flow domain for partially submerged vertical cylinder.	127
8.3	Temporal evolution of drag and lift force coefficients at Re_D = 12,500.	128
8.4	Instantaneous water–air interface elevation.	129
8.5	Contours of the instantaneous vorticity magnitude for $Re_D = 2.7\times10^4$ (a) on the plane adjacent to the bed (b) at the mid plane and (c) near the free surface: (left) present simulation and (right) Yu et al., [149].	130
8.6	Time-averaged air-water interface for volume fraction of 0.5 at $Re_D = 2.7\times10^4$ (left) Yu et al [149] and (right) present simulation (total height of the cylinder is 3D).	131
8.7	Time-averaged streamwise velocity contours at various positions.	132
8.8	Time-averaged pressure distribution on the plane 3.4D above the bed.	133

LIST OF TABLES

Table No	Table Title	Page No
3.1	Comparison between the *k*-ω and *k*-ε model.	34
4.1	Parametric studies considered for the 2D VOF simulations.	52
4.2	Determination of the inception of gas entrainment through parametric studies.	54
4.3	Parameters at the end of gas entrainment. The values of θ_{ss} and V_{ss} below refer to re-submergence angle and free surface velocity at the end of entrainment.	55
5.1	Effect of baffle width on free surface velocity at different depths.	74
6.1	Grid sensitivity study for Re=200.	89
6.2	Comparison of Strouhal number, drag coefficient and fluctuating lift coefficient for flow past a circular cylinder at Re = 200.	91
7.1	Grid sensitivity study for Re = 5×10^4.	114
7.2	Comparison of Strouhal number and drag coefficient for flow past a circular cylinder at Re = 5×10^4.	115
7.3	Lift and drag force coefficients for Re = 2×10^4 and 4×10^4 in 3D flow past a circular cylinder.	116
8.1	Comparisons of flow angles (α_1) and (α_2) against published data.	126
8.2	Grid sensitivity study at Re = 12,500, Fr = 0.3.	128
8.3	Comparison of Strouhal number, drag coefficient and fluctuating lift coefficient for flow past a circular cylinder at Re = 12,500.	129
8.4	Measured submergence angles and free surface velocity at different Froude numbers.	131

CHAPTER 1

INTRODUCTION

1.0 FOREWORD

The per capita electricity consumption of a country is regarded as a measure of its economic condition. India has about 128 GW of installed capacity comprising thermal, hydro and nuclear power plants with the share of nuclear power being ~ 3 %. In spite of this large installed capacity, the per capita consumption is only ~ 615 kWh/a. This is about 40 times less than the consumption of North American countries and about 8 times less than the world average. With increase in population, tremendous pressure is being exerted on increasing electricity production due to rapid growth in urbanization and industrialization.

Today, nuclear power is providing ~ 17% of electricity supply in the world. About 75%, 30% and 22% of the power requirements of France, Japan and USA respectively are met by nuclear energy. While the energy requirement of developed countries has almost stagnated, the demand is high in the developing countries like India. The projected minimum additional capacity requirement is about 200,000 MW by the year 2020. The choice of the source of electricity will depend in each country on the availability and cost of fuel, availability of capital funds and political decisions. But the resources of fossil fuel are finite and they have other non-electrical uses. Hence countries like India need to consider nuclear energy in a big way. Unfortunately, in the public mind, nuclear power is always associated with the nuclear holocaust such as Hiroshima and Nagasaki subjected to a sub-conscious aversion. In recent years, many factors have led to a fresh look at the nuclear option.

(i) Awareness of global warming being caused by the (emission of green-house gases) fossil fuel. Among the conventional sources of energy, nuclear power is free from green-house gas emission.

(ii) After the end of cold war, large amounts of fissile materials from thousands of undetonated nuclear weapons have to be utilized for peaceful purposes.

(iii) The amount of spent fuel that has been accumulating world wide as a result of operation of about 400 nuclear power reactors for nearly 6 decades, have to be disposed safely now. The safest way to dispose such large inventory of fissile material will be to burn them in power reactors for power generation.

1.1. NEED FOR FAST BREEDER TECHNOLOGY

Uranium (U), plutonium (Pu) and thorium (Th) are the basic elements of nuclear fission energy. Natural uranium has mainly two isotopes, U-235 and U-238. Of these, the percentage of U-235 is only 0.7% whereas the percentage of U-238 is 99.3%. U-235 can be fissioned by neutrons of all energy levels and the release of energy by such a fission is ~ 200 MeV. This is orders of magnitude larger than that released by burning of a carbon atom, (2-4 eV). India has a reserve of 70,000 tones of natural uranium and 360,000 tones of thorium, which perhaps is the largest thorium resource in the world.

The Indian nuclear power programme has been envisaged to have three stages for judicious utilization of limited uranium and vast thorium resources. In the first stage, Pressurized Heavy Water Reactors (PHWR) are deployed which use natural uranium as fuel and generate Pu-239 as a by product, which is fissile. Utilization of uranium in this type of reactors is < 3%. In order to utilize the rest of uranium, the second stage is envisaged. In the second stage, Liquid Metal cooled Fast Breeder Reactors (LMFBR) are deployed. In LMFBR, the Pu generated in the first stage of reactors is used as fuel for fission energy. The core of LMFBR is surrounded by natural or depleted uranium as fertile blanket material which in due course gets converted to Pu-239. The plutonium thus generated in a LMFBR is more than that used for fission leading to breeding ratio > 1. Towards the end of the second stage, thorium will be used as fertile material which gets converted to U-233 (another fissile isotope of uranium). The U-233 thus bred will be used as fissile fuel and thorium as blanket in the third stage of breeder reactors. The Indira Gandhi Centre for Atomic Research (IGCAR) is entrusted with the responsibility of developing fast breeder reactor technology for India. Already a loop type Fast Breeder Test Reactor (FBTR) of 40 MW thermal energy, is under operation at this centre and as a natural extension of FBTR, a larger capacity (500 MW) pool type LMFBR known as Prototype Fast Breeder Reactor (PFBR) is in an advanced stage of construction [1].

1.2. DESCRIPTION OF POOL TYPE LMFBR

The flow sheet of a pool type LMFBR is shown in Fig. 1.1.

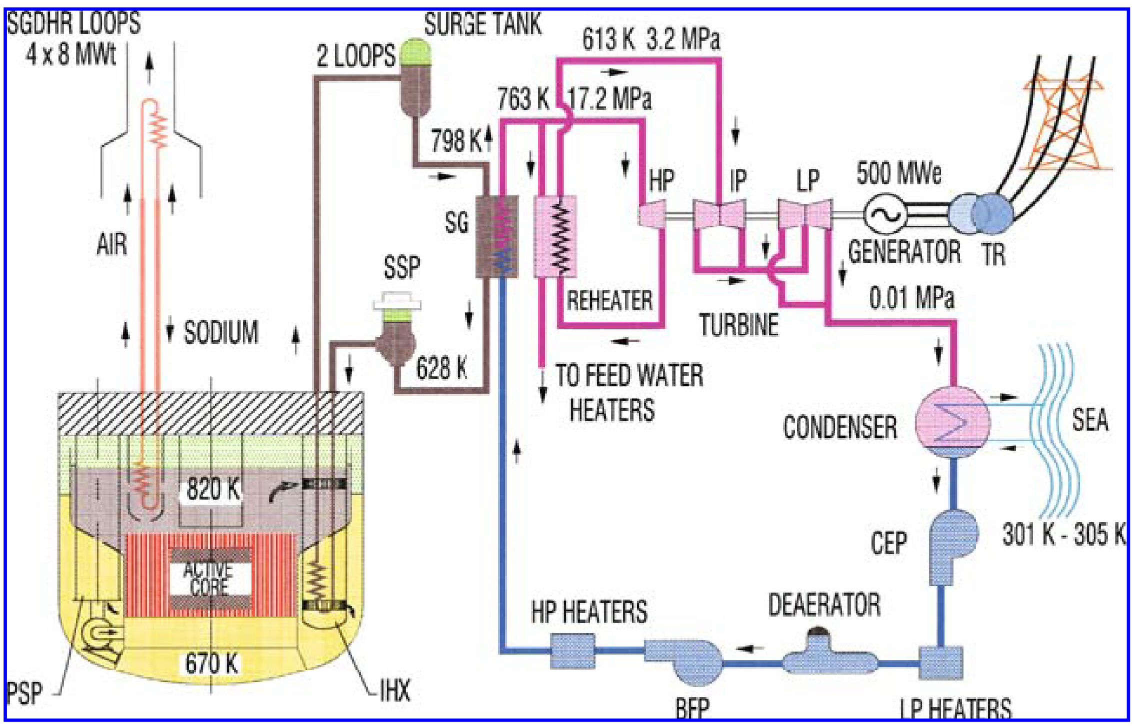

Fig. 1.1: Flow sheet of pool type fast breeder reactor (PFBR).

In an LMFBR, nuclear heat generated in the subassemblies of the core is removed by circulating sodium through the core. This sodium is radioactive and is known as primary sodium, which transfers heat to a non-radioactive secondary sodium through intermediate heat exchangers (IHX). The secondary sodium transfers the heat to water in steam generators to generate steam for electricity production. The schematic vertical section of a typical pool type LMFBR is shown in Fig. 1.2.

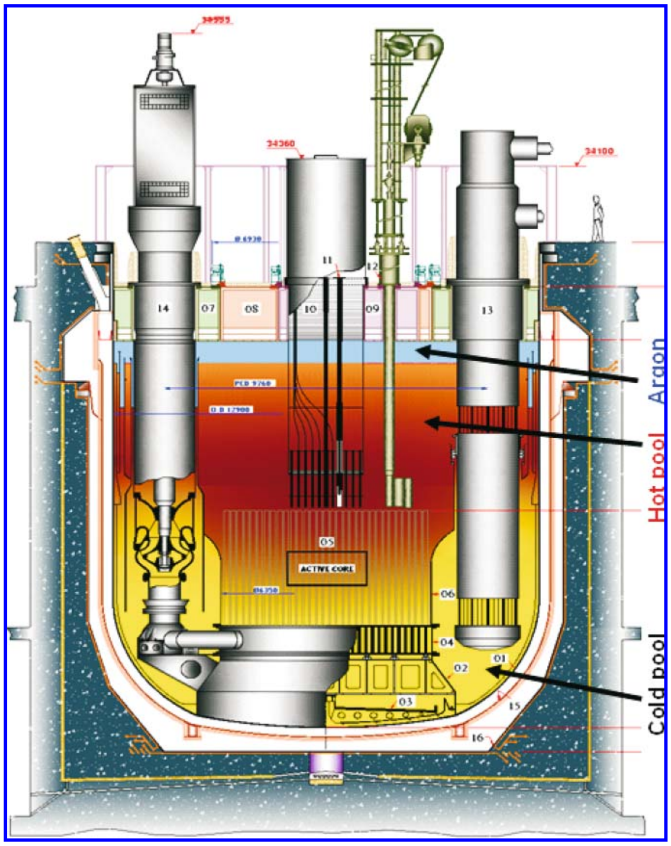

LEGEND	
01	Main Vessel
02	Core Support Structure
03	Core Catcher
04	Grid Plate
05	Core
06	Inner Vessel
07	Roof Slab
08	Large Rota table Plug
09	Small Ratable Plug
10	Control Plug
11	Control & Safety Rod Mechanism
12	In-Vessel Transfer Machine
13	Intermediate Heat Exchanger
14	Primary Sodium Pump
15	Safety Vessel
16	Reactor Vault

Fig. 1.2: Vertical section of reactor assembly of LMFBR.

In this type of reactors, the entire primary circuit consisting of reactor core, control plug (CP), IHX, decay heat exchangers (DHX), primary sodium pumps (PSP), grid plate and core support structure are immersed in a pool of liquid sodium. The grid plate is a high pressure plenum which feeds cold primary sodium to various subassemblies of the core. The core subassemblies and the grid plate are supported by core support structure which rests on the main vessel. The sodium pool is divided into hot pool and cold pool by a thin structure known as inner vessel. The IHX and pumps penetrate the inner vessel. Hot primary sodium from hot pool enters the IHX, exchanges heat with the secondary sodium and flows down to the cold pool, from where it is pumped back to core via grid plate by the primary sodium pumps. The main vessel which holds the sodium pools is an important structure and is a primary boundary for preventing any radioactivity release to the surroundings, apart from clad. Sodium being a liquid metal, having a very high heat transfer coefficient (~25,000 W/m^2K in highly turbulent forced convection regime), is the natural choice as heat transport medium. This is essential to remove very high heat flux values (~ 1.5 MW/m^2) encountered in the core. Another favorable point for the selection of sodium is its high boiling point (888 ^0C), so that the systems need not be pressurized to achieve high temperature. Hence, the main load on the structures is the thermal load arising out of high operating temperature (creep), large temperature gradient (thermal stress) and large number of cyclic variations in temperature (thermal fatigue) due to various incidents taking place in the plant.

The main drawback of sodium is its violent chemical reaction with air and water. Hence, in all the sodium systems, inert argon gas is maintained above the sodium free surfaces to avoid sodium-air contact. Secondary sodium circuits are employed to avoid entry of hydrogenous materials into the primary sodium. To enhance the safety and to contain primary sodium in an unlikely event of main vessel leak, a safety vessel is provided surrounding the main vessel. The roof slab forms the top cover for the main vessel which is filled with concrete for the purpose of nuclear radiation shielding. It has many narrow penetrations for the purpose of inserting components like primary pumps, IHX, control plug etc. The main vessel, the roof slab and the safety vessel are supported on the reactor vault, which is a concrete structure of about 2m thickness, cooled by water. The annular gaps between the main vessel, safety vessel and the reactor vault are filled with inert nitrogen gas.

1.3. THERMAL HYDRAULICS ISSUES OF LMFBR

In an LMFBR, argon blanket gas is maintained above the sodium free surface to accommodate volume changes of sodium as a result of its thermal expansion, due to various operating conditions of the reactor, as well as to avoid sodium-air contact through the numerous penetrations in the roof slab, as it reacts violently with air. Hence, a large sodium surface, which interfaces with argon, is formed. Reducing the size of the reactor vessel offers significant economic incentives. However, the reduction has a large impact on the thermal hydraulics of the hot pool. The thermal hydraulic parameters which are affected by the hot pool volume are: (i) attenuation of thermal transients to the hot pool structures arising out of reactor scram, pump trip etc. and (ii) agitation of sodium free surface. The agitation of free surface due to large convective velocities can lead to entrapment of argon gas within high velocity sodium and its transportation to IHX, if the drag force on the argon bubbles is higher than the buoyancy force. The argon bubbles, thus entering the IHX can reach the suction of the primary sodium pump, if they do not bubble out to the cover gas in the cold pool, which depends on the velocity of sodium prevailing in the cold pool. Passage of argon through the core leads to reactivity oscillations. In large size LMFBR like PFBR, if the gas passes through the central part of the active core, it leads to positive reactivity while its passage through the peripheral part of the active core leads to negative reactivity. Presence of a large quantity of argon in sodium can lead to inception of cavitation in the sodium pump and poor heat transfer in core and in IHX. Hence, adequate care needs to be taken in the design to avoid any entrainment of argon, in terms of adequate submergence of IHX primary inlet windows and lower levels of velocity close to the free surface. It may be mentioned that argon dissolves in sodium and its dissolution increases with temperature. The equilibrium concentration of argon in the hot pool, when the sodium temperature is 820 K is ~$7.5\text{x}10^{-2}$ g/m^3 [2]. Similarly, the equilibrium concentration of argon in the cold pool maintained at a temperature of 670 K is 0.5×10^{-2} g/m^3. Because of this, some quantity of argon is bound to be present in sodium. However, the dissolved argon is not expected to cause any reactivity perturbations in the core. But argon bubbles, which are entrained by physical mechanisms stay as separate phase and have a potential to cause reactivity perturbations.

In the hot pool, the control plug, which houses the control rod drive mechanisms, core monitoring thermocouples, failed fuel location modules etc., is positioned just above the fuel subassemblies (SA), to avoid formation of sodium hump at the free surface (Fig. 1.3).

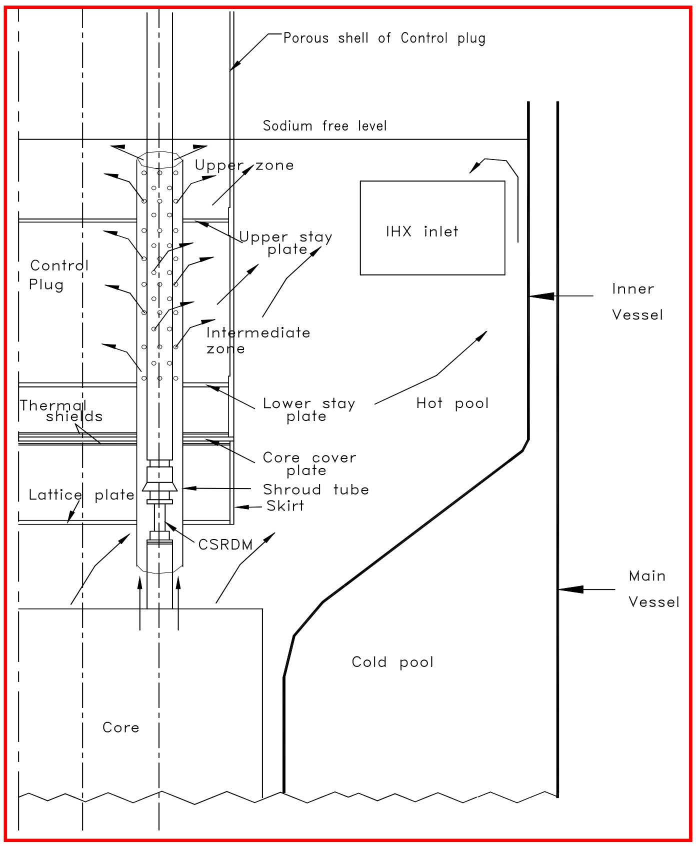

Fig. 1.3: Different parts of Control Plug.

The geometry of control plug has a direct bearing on the velocity distribution of sodium that enters the hot pool below the core cover plate (CCP) of the control plug. The concept of storing the spent fuel inside the main vessel (till its decay power reduces below a specific value conducive for handling in argon) and presence of blanket subassemblies lead to thermal stratification in the bottom zones of hot pool. Stratification is detrimental to the redan of inner vessel due to the instability of stratified sodium layers. The strength of this stratification is further enhanced by the heat loss from hot pool to cold pool, through inner vessel. To overcome the detrimental effect of stratification, a cylindrical skirt known as anti stratification skirt [3] is provided below the CCP surrounding the core monitors. This skirt increases the radial velocity of sodium entering the hot pool and is thus expected to enhance the velocity level within the hot pool and affect the free level calmness. Other zones prone to gas entrainment risks in the primary sodium circuit are: (i) the free fall of main vessel cooling flow in the collection plenum and (ii) the sodium free level around the rotating shaft of sodium pump. From the literature, it is found that, four types of gas entrainment mechanisms are possible in nuclear reactors. They are: (i) vortex activated gas entrainment [4, 5], (ii) liquid fall induced gas entrainment [6, 7], (iii) formation of drain-type vortex [8, 9] and (iv) shear induced gas entrainment [10, 11]. The graphical representation of various mechanisms of gas entrainment is depicted in Fig. 1.4.

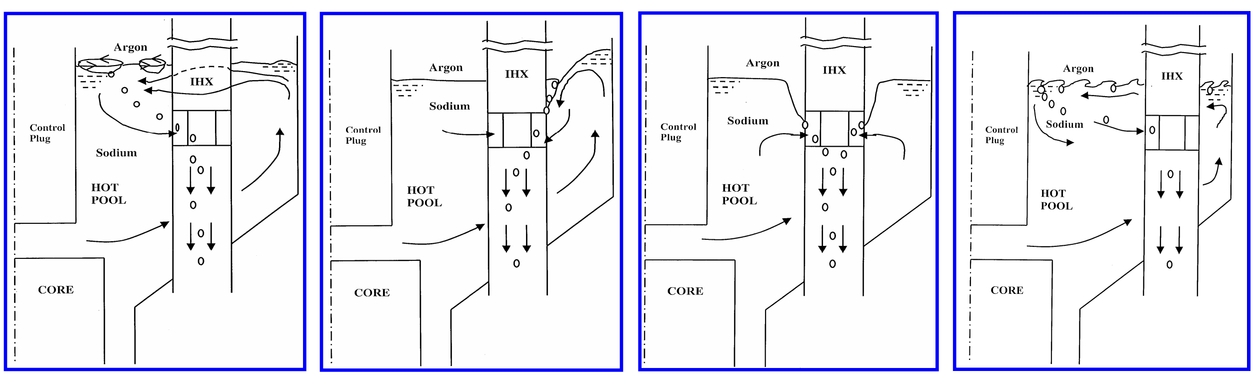

(a) (b) (c) (d)

Fig. 1.4: Schematic of various types of gas entrainment mechanisms that may occur in nuclear reactor: (a) vortex activated gas entrainment, (b) liquid fall induced gas entrainment, (c) drain-type gas entrainment and (d) shear induced gas entrainment.

1.4. MOTIVATION FOR THE PRESENT RESEARCH

1.4.1. Difficulties in Numerical Prediction

The hot pool is ~ 6m in radius and over ~ 5m in height. Typical diameter of spherical gas bubble, when entrainment takes place, is of the order of millimeters. In order to capture these small gas bubbles in a computational mesh, the problem has to be solved in 3-dimensions and the mesh size has to be comparable to the smallest bubble size. This results in a large number of mesh points or control volume cells, which is almost impossible to handle in the present day computers [12]. To compound these difficulties, 3-D numerical solution needs to be obtained in time domain to track the movement and break up of the entrained gas bubbles. To circumvent these difficulties, the experimental approach or combinations of experimental and numerical approaches are being followed to study gas entrainment in sodium systems.

1.4.2. Difficulties in Experimental Simulation

The non-dimensional numbers, which govern the flow distribution in hot pool with undulated free surface, are Froude number (Fr), Reynolds number (Re) and the Weber number (We). The obvious choice for a coolant, which can be used to simulate sodium, is water due to the fact that it is transparent, cheap and easy to handle. The kinematic viscosity of sodium ($3x10^{-7}$ m^2/s) is half that of water at room temperature ($6x10^{-7}$ m^2/s). The surface tension coefficient of sodium (0.16 N/m) is double that of water (0.07 N/m). Due to these reasons, respecting all the three non-dimensional numbers simultaneously is impossible in any scale size of the water model. However, the effect of Reynolds number is secondary, once the flow is well within the turbulent regime and hence mismatch in the Reynolds number can be permitted. Considering this, it can be shown that a scale of 0.59 is necessary to respect the Fr and We numbers exactly. Thus, the scale requirement is very large. Hence, chemicals such as sodium oleate have been proposed in literature which when added to water alter the properties of water. Alternatively, experiments can be carried out on a few number of small scale models and the results can be extrapolated for the full scale condition, based on the scale effect brought out by the study. But there are certain limitations on experiments carried out on scaled models. In scaled down models respecting Froude number, the velocity is always less than the prototypic value. Hence, it is essential to make sure that no entrainment takes place in the small-scale model even if the velocity is increased to the value in prototype. Based on such considerations, Eguchi et al., [13] propose equal velocity similitude (between the model and the prototype) for a conservative simulation of gas entrainment. On similar lines, Smith [14] argues that the downward velocity level in the model should be more than the terminal velocity, if the prototypic downward velocity is more than the terminal velocity. Violation of this criterion is expected to distort the distribution of entrained bubble size. Gas entrainment phenomenon is highly geometry dependent. Hence, experiments need to be carried out in models having exact geometric similarity with the prototype.

1.5. OBJECTIVES AND SCOPE OF THE PRESENT WORK

The present study is focused towards developing a computational model for prediction of conditions for onset of gas entrainment in liquid pools. It is directed towards understanding gas entrainment induced by liquid fall and vortex activated mechanisms. The scope of the research is basically computational. Nevertheless, these computational models are validated by appropriate experimental/numerical results published in open literature. The objectives of the study are:

(i) Investigate multiphase flow distributions in idealized models of hot pool employing free surface tracking models, viz., volume of fluids (VOF) [15] method and establish a free surface velocity criterion for the onset of gas entrainment.

(ii) Investigate flow distribution in the hot pool of a medium sized FBR and identify a passive anti-gas entrainment device.

(iii) Investigate laminar and turbulent 3-D vortex shedding phenomena behind cylindrical components, which play a critical role in vortex activated gas entrainment.

(iv) Develop understanding of free surface profile/velocity characteristics by 3-D multiphase simulations and assess the risk of gas entrainment around partially submerged cylindrical components.

1.6. ORGANIZATION OF THE THESIS

The thesis is divided into three major parts. The first part consists of three chapters with the introduction of the problem in Chapter 1, detailed survey of relevant literature in Chapter 2 and mathematical formulation and solution procedure in Chapter 3. The second part consists of five chapters (Chapters 4 to 8). Chapter 4 deals with basic studies on liquid fall induced gas entrainment. Chapter 5 deals with application oriented studies related to identification of a passive device for reactor hot pool of a 500 MW pool type LMFBR. Chapter 6 brings out the investigation of laminar vortex shedding past a finite circular cylinder mounted on a flat plate in order to study the vortex activated entrainment. Chapter 7 deals with investigation of turbulent vortex shedding past a finite circular cylinder mounted on a flat plate. Chapter 8 deals with investigation of free surface characteristics during turbulent flow past a circular cylinder. Finally, the major conclusions derived from these studies are summarized in Chapter 9.

CHAPTER 2

LITERATURE REVIEW

2.0. FOREWORD

Gas entrainment phenomenon can cause unfavorable operational problems in the reactor which are listed below:

(i) A large variation of argon gas content in the core possibly causes a reactivity fluctuation.

(ii) Argon bubbles are nucleation sites for boiling or cavitation.

(iii) If large argon bubbles can get trapped in a subassembly, burn out of fuel pins may occur.

Hence, it is important to mitigate the gas entrainment at the free surface of the hot pool. Considering the significance of the gas entrainment, many fundamental experiments as well as numerical studies on reactor geometry models have been carried out by various researchers. Important among them are reviewed here.

2.1. FUNDAMENTAL EXPERIMENTS

2.1.1. Liquid-Fall Induced Entrainment

Laithwaite and Taylor [16] conducted water experiments on different scale models of Prototype Fast Reactor (PFR) to study gas entrainment due to liquid fall and vortex formation mechanisms. They observed that surface tension is not an important parameter in large-scale models. No serious wave formation (shearing of gas-liquid interface) was seen on the free surface of the model. Madarame and Chiba [6] performed experiments on slab models to identify conditions leading to gas entrainment. The geometry considered by them was an idealized upper plenum of IHX in Demonstration Fast Breeder Reactor (DFBR), where the primary sodium flows on the tube side. Based on the submergence of the inlet nozzle and the width of the plenum, they identified that waterfall induced entrainment occurred when the re-submerging velocity is high.

Their results indicated that when the re-submerging velocity is such that the 4^{th} root of the product (Fr.We) < 2, no entrainment was found to take place irrespective of any submergence depth.

Following Madarame's experiment, Hagiwara et al., [17] performed similar tests and concluded that the liquid fall induced entrainment is governed not only by re-submerging velocity but also by re-submerging angle. They found that, for re-submerging velocity < 0.8 m/s, the critical re-submerging angle is 12^o. If the angle exceeds 12^o, entrainment takes place. Eguchi et al., [18] performed fundamental experiments in different slab models to study gas entrainment at free surface of water. They concluded that the critical Froude number, above which gas entrainment appears, is a strong function of the model scale and it decreases as model size increases. Kimura et al., [19] studied gas entrainment phenomenon experimentally using dipped plate just below the free surface of liquid to keep free surface calm thereby avoiding liquid fall and shearing type entrainments. The vortex type of entrainment was still dominant in the region of gaps between dipped plate and reactor internals. They have concluded that vortex type entrainment results into highest quantity of gas entrapment.

2.1.2. Formation of Drain-Type Vortices

Baum [20] experimentally analyzed the phenomenon of air entrainment induced by drain-type vortex. He observed that for H/D > 1.5 (submergence depth/drain-hole diameter), the Weber number does not influence vortex formation and for H/D < 1.5, its effect cannot be neglected. He also proposed a correlation to estimate the submergence height to avoid inception of air entrainment. Unfortunately, the range of Fr considered by him was very narrow. Baum and Cook [8] performed experiments using sodium, water, white sprit and Freon 113 in a simple small-scale model of cylindrical tank with tangential inlet and bottom outlet. Their experimental results indicated that, for drain-type vortices, water experiments are conservative. Takahashi et al., [9] experimentally analyzed the occurrence of drain-type vortices for the suction flow into a vertical pipe in a cylindrical vessel. From visual observation and theoretical consideration, it was found that the onset conditions for drain type entrainment are dominated by the following two criteria: (i) whether the air core formed by vortex reaches the pipe and (ii) whether the water flow in the suction pipe is fast enough for the flow to draw bubbles downward. Sakai et al., [21] performed experiments on drain-type vortex with a tangential entry at the top and an outlet at the bottom. They measured velocity distribution around the gas core and proposed a correlation with the depth of the vortex.

Ardron and Bryce [22] carried out experiments in horizontal pipes, partially filled with water and having a drain hole at the bottom. The submergence height (H) required to avoid gas entrainment due to drain-type vortex was found to obey the criterion,

$$H = \frac{K W_c^{0.4}}{\left(g \rho_{sod} \Delta \rho\right)^{0.2}} \tag{2.1}$$

where the value of K (proportional constant) is 1.5, W_c is the mass flow rate of the liquid, g is acceleration due to gravity, ρ_{sod} is liquid density and $\Delta\rho$ is the density difference between the liquid and the gas. Shiraishi et al., [23] analyzed the formation of drain-type vortex induced by a rotating cylinder. They presented a criterion that for $W_o^2/gH < 0.25$, (where W_o is the downward velocity at the vortex core, H is the submergence height), gas entrainment may not occur easily. They also pointed out that the diameter of the vortex dimple (generated due to vortex shedding behind IHX) increases and its height decreases with increase in velocity which leads to entrainment. Monji et al., [24] observed through experiment that a long gas core tends to be broken randomly by flow fluctuations. However continuous gas bubble detachments from the tip of the gas core were observed as a definite phenomenon. Transient behavior of gas entrainment caused by surface vortex was studied by Ezure et al., [25] through visualization techniques. It was found that the gas core length extends with time delay to the increase of circulation around the vortex.

2.1.3. Vortex Activated Entrainment

Greaves and Kobbaccy [4] observed that small vortices are formed due to the turbulence generated at the interface while investigating the mechanism of surface aeration. They correlated the entrainment with the impeller type, location, size and speed of the impeller and geometry of the tank. Sverak and Hruby [5] investigated the mechanism of surface aeration by vortex formation and observed that, the process of vortex formation can be characterized by two non-dimensional numbers, viz., Froude Number and Strouhal Number. Air entrainment in open channel studied by Ervine and Falvey [11] indicated that entrainment occurs when the turbulence level is large enough to overcome both surface tension and gravity. They found that, air gets entrapped when turbulent velocities normal to the free surface became greater than 0.1 - 0.3 m/s.

Smith [14] conducted experiments on different water scaled models of Commercial Demonstration Fast Reactor (CDFR) hot plenum with special attention to vortices shed downstream of IHX, pump stand pipe etc. and measured the frequency of vortex formation and depth of vortex. Their study indicated that the maximum depth of vortex increases with increase in size of the model indicating its dependence on scale size. Guidez and Cognet [26] discuss the possibility of vortex induced entrainment by simulating water-air combination at reduced scale models. They pointed out that small-scale models are not conservative but necessary for parametric studies. Funada et al., [27] mentioned the possibility of gas entrainment in IHX vessel of DFBR, when the free surface velocity is 0.9 m/s. They along with Miura et al., [28] performed experiments in geometrically similar IHX vessel and observed that the critical Froude number for gas entrainment was a function of scale size which indirectly indicated that a similitude criterion suitable for onset of entrainment is equal velocity condition between the model and the prototype. Astegiano et al., [29] presented a series of experimental and numerical studies carried out on the water tests and pointed out that small scale models lead to optimistic results with respect to gas entrainment behavior in the prototype.

Fundamental water experiments on slab models carried out by Gowda and Prasad, [30] indicated that, for $V/(Dg)^{1/2} > 3$ (where V is the water velocity entering the plenum below the control plug and D is the diameter of IHX), the free surface flow pattern was waterfall dominant with risk of gas entrainment. Free surface flow pattern becomes vortex dominant for $2 \leq V/(Dg)^{1/2} \leq 3$, while for $V/(Dg)^{1/2} \leq 2$, the free surface was either quiet or wavy, but without any risk of gas entrainment.

2.1.4. Shearing of Free Surface

Clark and Vermeulen [10] investigated conditions of surface aeration in stirred tank through visual observation on the liquid surface and found that a region of high shear exists on the liquid surface, which occurs due to a combination of flows in the opposing directions (first the impeller discharge flow and second the flow that is rebounded off). The oscillatory surface formed a small wave that entraps gas which eventually gets carried out into the liquid. Volkart [31] studied the shear type entrainment in smooth channels and spillways through surface visualization using a stroboscope. It was observed that the entrainment of air in liquid resulted due to falling water droplets that were ejected from the liquid surface due to high levels of turbulence. The author also observed that the diameters of the bubbles formed were larger than the diameter of the falling liquid droplets. However, the proposed mechanism does not serve to explain entrainment in all types of systems as the surface velocities required for above mentioned phenomenon to occur are much higher (~ 5 m/s) as compared to the surface velocities reported (0.25 – 0.34 m/s) by other investigators [32, 33, 34]. Yahalom and Bennett [35] experimentally studied gas entrainment in a 1:14.4 scale model of 1000 MWe loop type FBR hot pool respecting Froude Number similarity. The objectives of the study were (i) sweeping (shearing) induced gas entrainment, generated when sodium discharges from the control plug shell at high velocities close to the free surface and (ii) gas entrainment due to vortex shedding from objects in the pool such as DHX. It was observed that when velocity was 0.78 m/s, no sweeping induced entrainment was found but occasional vortex induced entrainment was observed near the DHX. However, when the discharge velocity was very high (~ 2.5 m/s), the surface was very rough with large quantities of sweeping induced entrainment. They proposed a thumb rule of keeping $V^2/gH < 0.1$ (where, V is the discharge velocity at CP exit and H is the discharge submergence of CP hole) to avoid gas entrainment. Chanson [36] reviewed the characteristics of self-aerated flows (flows with high surface aeration) in chute sand spillways. He concluded that the gas entrainment in liquid occurs when the turbulent velocity normal to the liquid surface is large enough to overcome the surface tension and the bubble rise velocity. The author also proposed the following conditions for the onset of gas entrainment to occur.

$$v' = (8\sigma/(\rho w d_b))^{1/2} \tag{2.2}$$

and

$$v' > u_r \cos\alpha \tag{2.3}$$

where v' is RMS of lateral component of fluctuating velocity, σ and ρ are the surface tension and density of the liquid, d_b is the bubble diameter, w is the width of the tank, u_r is bubble rise velocity and $\cos\alpha$ represents angle of bubble inception. The issue of entrainment of argon cover gas in LMFBRs was addressed by Govindaraj et al., [37]. They performed experiments in cylindrical tank and proposed a correlation for onset of entrainment. Masuzaki et al., [38] carried out experiments for prevention of gas entrainment on 1/10 scale water model of DFBR upper plenum and IHX plenum. For the upper plenum, they studied two different devices: (i) providing a ring plate around the IHX-primary suction and (ii) making the control plug as porous. They found that both these modifications are able to prevent gas entrainment. Similarly, for the IHX plenum lowering the primary inlet pipe and providing baffles around the IHX were found to prevent gas entrainment.

Sun et al., [39] carried out experimental and numerical investigations of gas hold up distribution in surface aerated stirred tanks. Experimentally, the gas holdup was measured using conductance probe. The numerical simulations were carried out using two fluid models with standard k-ε turbulence model. They proposed a fundamental equation for prediction of local rate of surface aeration at which gas got entrained in the liquid as;

$$R_g = B\left(\nu\varepsilon\right)^{1/4} \tag{2.4}$$

where, R_g is rate at which gas is entrained through the liquid surface, ν is kinematic viscosity, ε represents rate of dissipation of turbulent kinetic energy and B is proportionality constant. Although the above equation could not accurately predict the gas hold up distribution, it did bring considerable improvements in aeration rate particularly at a high agitation speed. Bhattacharya et al., [32] studied air entrainment in baffled stirred tanks to determine the effect of impeller submergence, impeller diameter and physical properties of fluid on the onset of gas entrainment. It is observed that, the r.m.s. and the mean velocity need to be in certain proportion for onset of gas entrainment. Mali and Patwardhan [33] investigated characterization of shear and liquid fall type entrainment in stirred tank with various impeller geometries with air–water and xylene–water systems. It was observed that the onset of entrainment can be characterized by the mean velocity and turbulent kinetic energy near the free surface. Durve and Patwardhan [34] studied the shear type entrainment using experimental techniques such as Ultrasonic Velocity Profiler (UVP), Particle Image Velocimetry (PIV) and High Speed Photography (HSP) in conjunction with Large Eddy Simulations (LES). The effect of surface tension and viscosity of liquid on entrainment was studied by changing the respective values in the simulation. Onset of entrainment was found to be more sensitive to changes in viscosity of the continuous phase as compared to surface tension of gas–liquid system.

2.2. NUMERICAL STUDIES

For the prediction of 3-D flows with deforming gas-liquid interface, numerical methods such as Height Function Method and Volume of Fluids (VOF) method [15] have been developed and incorporated in commercial CFD computer codes such as STAR-CD [40]. The effect of gas entrainment on thermal hydraulic performance of sodium cooled reactor core is reported in detail by Hori and Friedland [41]. Ueda et al., [42] studied numerical simulations of free surface activity by VOF method and reported that VOF method is capable of estimating large-scale wave motions and drain-type vortices. However, they felt that finer grid size and large computational effort are needed to get accurate solutions. Menant et al., [43] reported experimental results of OREILLETTE mockup of SPX2 and the utility of the CFD code "TRIO-VF" in assessing gas entrainment. They found out that the free surface flow was dominated by two opposing recirculations in the wake of pump stand pipe and IHX, which induce strong downward velocity and consequent gas entrainment. The maximum value of free surface velocity in between IHX and pump stand pipe is 0.6 m/s (numerical) and 0.55 m/s (experimental). Free surface was seen to become calm by the introduction of vertical stiffener plates between the components and the upper shell of inner vessel. They also reported that, though TRIO code has the potential to predict the general flow patterns in the pool but has little significance in predicting the vortices due to their small-scale nature.

Qing [44] explained the formulation of the "AQUA-VOF" code, which is capable of analyzing deforming free surfaces. Using this code, he predicted the flow distribution and shape of free surface in an idealized model of Demonstrative Fast Breeder Reactor (DFBR) hot pool, having IHX-suction pipe immersed in the pool. He found that there is a large free surface undulation in the reference geometry of hot pool and made the free surface calm by introducing two horizontal baffles (one attached to control plug and the other attached to upper shell of inner vessel) at a certain depth from the mean free level. Okamoto and Madarame [45] investigated the characteristics of self-induced oscillations of liquid surfaces caused by vertical submerged water jets, such as Jet-Flutter, Sloshing etc. Later, Iida [46] developed a 3-D FEM computer code named "SPLASH-ALE", to capture the free surface movements. The code was found to predict the frequency and amplitude of the jet flutter accurately. CFD studies carried out by Sakai et al., [47] proposed two types of design criteria on gas entrainment for bathtub/drain type vortex. The first is a gas core extension directly to the outlet piping level, which induces a large amount of gas entrainment to the flow system. The second involves continuous bubble detachments from the tip of the vortex dimple. It was found that the non-dimensional numbers are useful for the design parameters of gas entrainment criteria. A gas entrainment prediction method has been developed by Ito et al., [48] to establish design criteria for the large scale sodium-cooled fast reactor systems by introducing the surface tension effects into the prototype gas entrainment prediction method. Results showed that the analytical gas core lengths calculated by the improved gas entrainment prediction method became shorter in comparison to the prototype gas entrainment prediction method, and are in good agreement with the experimental data [49]. Tenchine [50] highlights the various sources of gas entrainment in the primary sodium pool of FBR and the challenges in their computational prediction. Detailed 3-D thermal hydraulic studies have been carried out by Velusamy et al., [3] using CFD code PHOENICS [51] to see the efficacy of using baffle plates in reducing free level velocity.

2.3. CLOSURE

From the above literature survey, it is clear that the numerical studies on various types of gas entrainment mechanisms and their mitigation strategy are very limited. Therefore, careful studies on various types of gas entrainments are needed. The present work attempts to address the onset of gas entrainment caused by liquid fall and vortex activation mechanisms through the study of 2-D and 3-D computational models and validate them against experimental and numerical results reported in open literature.

CHAPTER 3

MATHEMATICAL FORMULATION

3.0. FOREWORD

As the present work concerns with numerical investigations of gas entrainment phenomenon in an LMFBR, the conservation equations that govern the fluid flow with free surface are presented in this chapter. This chapter consists of two main sections; the first section introduces the background theories of CFD and the techniques for solving fluid flow problems while the second part deals with the various turbulence models with different interface capturing methods that are employed for investigation of gas entrainment in reactor hot pool.

3.1. OVERVIEW OF COMPUTATIONAL FLUID DYNAMICS (CFD)

Fluid dynamics is the science of fluid motion. The study of fluid flow is possible by three different routes, viz., (i) Experimental, (ii) Theoretical and (iii) Numerical. The numerical route is known as Computational Fluid Dynamics (CFD). The CFD route consists of three elements known as (i) *pre-processor*, (ii) *solver* and (iii) *post-processor* [52]. Pre-processor consists of inputs of the flow problem to a CFD program by means of an operator friendly interface and the subsequent transformation of this input into a form suitable for use by the solver. The region of the fluid to be analyzed is called the computational domain and it is made up of a number of discrete volumes called the mesh or grids. After mesh generation, the properties of fluid and appropriate boundary conditions are specified. The solver completes the solution of the CFD problem by solving the governing equations. The governing equations are in the form of Partial Differential Equations (PDE) made up of combinations of flow variables and its derivatives. The solver converts the PDEs into a system of algebraic equations employing the finite difference (or) finite volume (or) finite element method. This process is known as numerical discritisation.

The different methods of discretisations are described in the flow chart given below (see Fig. 3.1). The present thesis work is based on the finite volume method using the commercial CFD software package FLUENT 6.3 [53]. Post-processor is used to visualize and process the results from the solver part quantitatively.

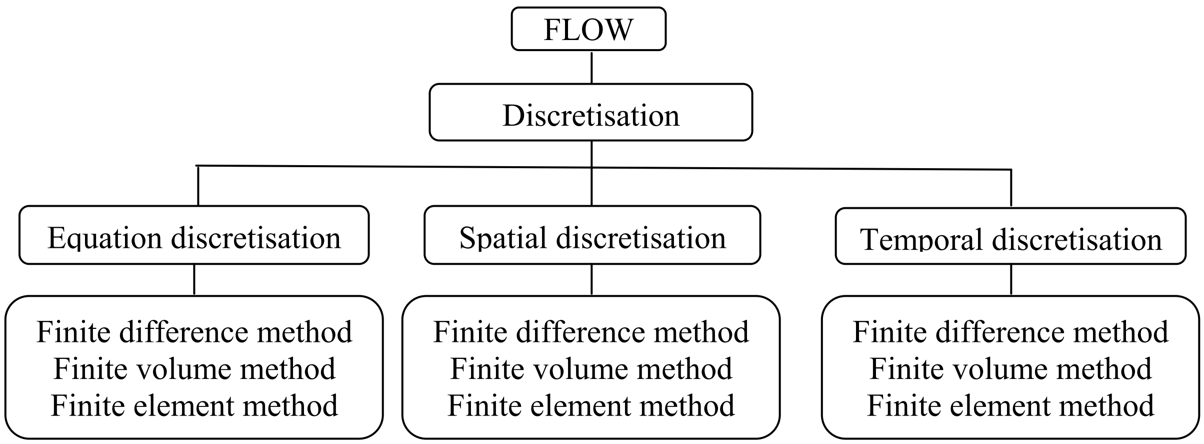

Fig. 3.1: Various discretisation methods.

3.2. GOVERNING EQUATIONS

Combining the fundamental principles, the physics of fluid flow is expressed in terms of a set of partial differential equations known as Navier-Stokes equations given by famous French engineer Claude-Louis Navier and the Irish mathematician George Stokes. These equations are derived from fundamental governing equations for fluid dynamics known as the continuity, the momentum and the energy equations which represent the conservation laws of physics. For incompressible flow, the following equations describe the fluid flow [54],

- Navier-Stokes equations: (conservation of momentum)

$$\frac{\partial u_i}{\partial t}+u_j\frac{\partial u_i}{\partial x_j}=-\frac{1}{\rho}\frac{\partial p}{\partial x_i}+\frac{\partial}{\partial x_j}\left(\nu\frac{\partial u_i}{\partial x_j}\right) \tag{3.1}$$

- The continuity equation: (conservation of mass)

$$\frac{\partial u_i}{\partial x_i}=0 \tag{3.2}$$

3.3. AN OVERVIEW OF TURBULENCE MODELS

Flow can be laminar or turbulent depending on the fluid flow conditions reflected through Reynolds number. For engineering applications, most flows are turbulent in nature. Turbulence is chaotic in nature exhibiting random variation in space and time and is characterized by its irregularity, three-dimensionality and dissipative nature. Flow in turbulent regime contains eddies with different sizes which are always rotational in motion and are responsible for carrying of energy and momentum in the flow. The smallest scale eddies, where dissipation of energy occurs are known as the *Kolmogorov* scale eddies. The time and length scales of these eddies are smaller than the time periods or lengths of engineering interest. In spite of their tiny sizes, the eddy Reynolds number of turbulent motion is of the order of unity, suggesting that even the smallest eddy obeys the continuum hypothesis [55]. Larger eddies extract energy from the mean flow and transfer it to the smaller eddies where energy is taken out through viscosity which is known as the *Richardson's cascade*. Currently available computer power is not yet sufficient to resolve the smaller eddies. So turbulence models are generally based on some simplified assumptions. An overview of turbulence models commonly adopted in CFD simulations is shown in Fig. 3.2. Generally, turbulent simulations can be done by *filtering* or *averaging* the Navier-stokes equations.

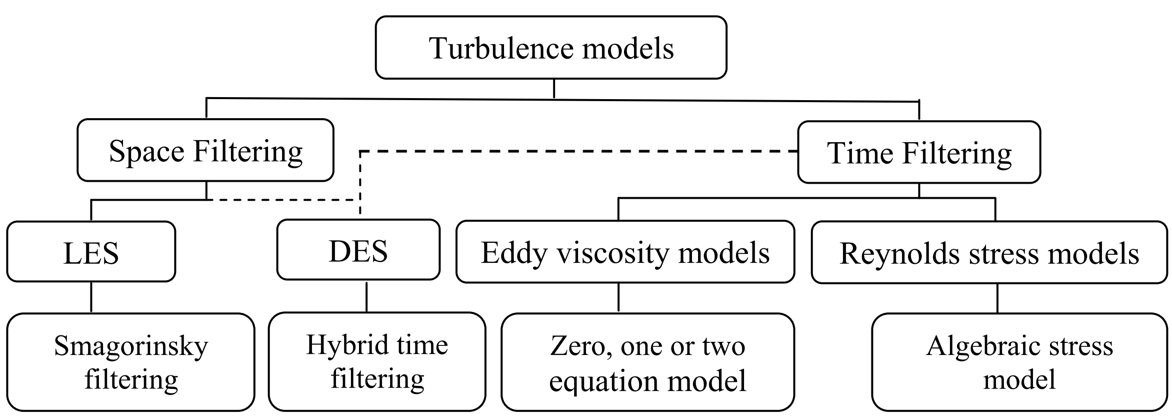

Fig. 3.2: An overview of various turbulence models.

3.3.1. Filtering

The main idea behind this approach is to filter the time dependent Navier Stokes equations in either Fourier space or configuration space. A simulation using this approach is known as *Large Eddy Simulation* (LES) [56]. The filtering process creates additional unknown terms known as *Sub-Grid Scale Stresses* (SGS) which must be modeled in order to provide closure to the set of equations [57]. In the simplest model originally proposed by Smagorinsky, the SGS are computed using an isotropic eddy viscosity approach. The eddy viscosity is then calculated from an algebraic expression involving the product of a model constant (C_S). But the problem with this approach is that, there is no single value of the constant which is universally applicable to a wide range of flows. To overcome this, *Dynamic Smagorinsky Model* (DSM) was proposed [58]. In this case, the constant 'C_s' is dynamically computed during the simulation using information provided by the smaller scales of the resolved fields. In this way Smagorinsky model is able to simulate the transitional flow.

3.3.2. Reynolds Averaging

In the *Reynolds averaging* approach, all flow variables are divided into a mean and a rapidly fluctuating component and then all equations are time averaged to remove the rapidly fluctuating components. In Navier Stokes equations, the time averaging introduces new terms which involve mean value of products of rapidly varying quantities known as *Reynolds Stresses* [59]. There are two sub categories for time averaging approach: (i) *Eddy-viscosity* model and (ii) *Reynolds stress* model.

3.3.2.1. Eddy-Viscosity Model

This model is based on the assumption that turbulent stress is proportional to the mean rate of strain and eddy viscosity is derived from turbulent transport equations.

- *Zero equation models*: It is one of the oldest turbulence models in which turbulent kinematic viscosity (ν_t) is expressed as a product of turbulent velocity (θ) and length scale (ℓ) as [60];

$$\nu_t = C\theta\ell \tag{3.3}$$

where C is constant of proportionality. The dynamic turbulent viscosity is written as;

$$\mu_t = C\rho\theta\ell \tag{3.4}$$

The kinetic energy of the turbulence is contained in the largest eddies. For such flows the turbulent velocity scale is described by

$$\theta = c\ell\left|\frac{\partial U}{\partial y}\right| \tag{3.5}$$

where c is a dimensionless constant and $\left|\frac{\partial U}{\partial y}\right|$ is the mean velocity gradient. Combining eqs. (3.3) and (3.5) and absorbing the two constants (C, c) into a new length scale ℓ_m, we obtain

$$\nu_t = \ell_m^2\left|\frac{\partial U}{\partial y}\right| \tag{3.6}$$

This is known as *Prandtl's mixing length model*. This model is easy to implement, cost effective in terms of computing resources and good enough to predict thin shear layers like jets, mixing layers, wakes and boundary layers. However, the mixing length model is incapable of describing the flows with separation and recirculation.

- *One equation models*: In this category of models, the velocity scale is obtained by the solution of a simple PDE. The *Spalart-Allmaras model* is a one equation model that models production, transport, diffusion and destruction of the turbulent viscosity [61]. This model is suitable for external flows encountered in aerospace applications but it fails to predict internal flows.

- *Two equation models*: These are the most common type of turbulence models used for most types of industrial problems. This model includes two extra transport equations to represent the turbulent properties of the flow. One of the transport variables is the turbulent kinetic energy (k) and the other is the turbulent dissipation (ε), or the specific dissipation (ω). Details of two equation models are given in the subsequent sections.

3.3.2.2. Reynolds Stress Models

It is the most elaborate type of turbulence model which closes the Reynolds-averaged Navier-Stokes equations (RANS) by solving transport equations for the Reynolds stress, together with an equation for dissipation rate. In this case additional transport equations are required (4 in 2-D flows and 7 in 3-D flows) for getting the solution. It is claimed that, the Reynolds stress model has greater potential to achieve accurate prediction in complex flows [62].

3.3.2.3. Detached Eddy Simulation (DES)

This was first proposed by Spalarat [63] in an attempt to combine the most favorable aspect of RANS and Large Eddy Simulation (LES). DES reduces to RANS calculation near solid boundaries and to LES calculation away from the wall. Both LES and DES models are highly computationally intensive and hence are not adopted in the present studies.

3.3.2.4. Reynolds Averaged Equations for Turbulent Flow

The basic tool required for the derivation of Reylonds Averaged Navier-Stokes equations from the instantaneous Navier-Stokes equations is the *Reynolds decomposition* which refers to separation of the flow variables into the mean and fluctuating components [60] as follows;

$$u = \overline{u} + u' \tag{3.7}$$

where $\overline{u}$ and u' represent the mean and fluctuating parts of the turbulent velocity. From an engineering point view, only mean effects of the turbulent quantities are important. Hence, a more practical approach is necessary to model the averaged turbulent quantities. In order to model a turbulent flow, the turbulent fluctuations in the governing equations are averaged over time through the process known as *Reynolds averaging*. The time averaging of velocity component is defined as,

$$\overline{u} = \frac{1}{T}\int_{0}^{T} u(t)\, dt \tag{3.8}$$

where T represents the time period, usually chosen to be large compared to the typical timescale of turbulent fluctuation. Substituting Eq. (3.7) into eq. (3.1), one obtains the time averaged Navier-Stokes equations as follows:

$$\frac{\partial \overline{u}_i}{\partial t} + \overline{u}_j \frac{\partial \overline{u}_i}{\partial x_j} = \frac{1}{\rho}\frac{\partial \overline{p}}{\partial x_i} + \frac{\partial}{\partial x_j}\left(\nu \frac{\partial \overline{u}_i}{\partial x_j} - \overline{u_i^{'} u_j^{'}} \right) \tag{3.9}$$

where ρ, p and ν represent the density, pressure and kinematic viscosity respectively. The statistical averaging of the Navier-Stokes equations gives rises to the unknown terms $\overline{u_i^{'} u_j^{'}}$ known as the *Reynolds stress* [64] that relates the fluctuating velocity components to the mean quantities. The existence of the Reynolds Stress means there is no longer a closed set of equations and turbulence model assumptions are needed to estimate the unknowns to solve this closure problem.

3.3.2.4.1. The standard k-ε model

The k-ε turbulence model solves the flow based on the assumption that the rate of production and dissipation of turbulent flows are in near balance in energy transfer. The dissipation rate (ε) of the energy is written as [60],

$$\varepsilon = \frac{k^{3/2}}{L} \tag{3.10}$$

where 'k' is the turbulent kinetic energy and L is length scale. The turbulent viscosity μ_t is related to k and ε by,

$$\mu_t = \rho C_\mu \frac{k^2}{\varepsilon} \tag{3.11}$$

where *'C_μ'* is an empirical constant. The transport equation for the turbulent kinetic energy in the *k-ε* model is,

$$\frac{\partial(\rho k)}{\partial t} + \bar{u}_i \frac{\partial(\rho \bar{u}_j k)}{\partial x_j} = \frac{\partial}{\partial x_j}\left(\frac{\mu_t}{\sigma_k}\frac{\partial k}{\partial x_j}\right) + \mu_t \frac{\partial \bar{u}_i}{\partial x_j}\left(\frac{\partial \bar{u}_i}{\partial x_j} + \frac{\partial \bar{u}_j}{\partial x_i}\right)\frac{\partial \bar{u}_i}{\partial x_j} - \rho\varepsilon \tag{3.12}$$

The equation for *ε* is,

$$\frac{\partial(\rho \varepsilon)}{\partial t} + \bar{u}_i \frac{\partial(\rho \bar{u}_j \varepsilon)}{\partial x_j} = \frac{\partial}{\partial x_j}\left(\frac{\mu_t}{\sigma_\varepsilon}\frac{\partial \varepsilon}{\partial x_j}\right) + C_{\varepsilon 1}\frac{\varepsilon}{k}\mu_t \frac{\partial \bar{u}_i}{\partial x_j}\left(\frac{\partial \bar{u}_i}{\partial x_j} + \frac{\partial \bar{u}_j}{\partial x_i}\right) - \rho C_{\varepsilon 2}\frac{\varepsilon^2}{k} \tag{3.13}$$

Physically, the rate of change of kinetic energy is related to the convection and diffusion of average/mean motion of the flow. The diffusion term is assumed to be proportional to mean gradient of velocity. The production term, which is responsible for the transfer of energy from the mean flow to the turbulence, is counterbalanced by the interaction of the Reynolds stresses and mean velocity gradient. The destruction term deals with the dissipation of energy into heat due to viscous nature of the flow. Based on extensive examination of a wide range of turbulent flows, the constant parameters used in the equations take the following values [65];

$C_\mu = 0.09$, $C_{\varepsilon 1} = 1.44$, $C_{\varepsilon 2} = 1.92$, $\sigma_k = 1.0$, and $\sigma_\varepsilon = 1.3$

The *k-ε* model has gained popularity among RANS models due to

- robust formulation
- widely documented and reliable
- lower computational overhead

However, the model encounters some difficulties in:

- over prediction of turbulence near stagnation point
- length scale is too large in adverse pressure gradient flows
- fails to resolve flows with large strains (swirling and curved boundary layers flow).

3.3.2.4.2. RNG k-ε model

The frame work in this model is based on the principles of *Renormalization Group (RNG)* theory due to Yakhot and Orszag [66]. In the RNG *k-ε* model, apart from the standard equations given by eq. (3.12) and (3.13), the rate of dissipation of turbulent kinetic energy equation is augmented on the right-hand side by an extra strain-rate term '*R*' given by:

$$R = -\frac{c_{\mu}\eta^{3}(1-\eta/\eta_{0})\varepsilon^{2}}{(1+\beta_{0}\eta^{3})k} \tag{3.14}$$

where the quantity η is given as

$$\eta = \frac{k}{\varepsilon}\left[\left(\frac{\partial \overline{u}_i}{\partial x_j} + \frac{\partial \overline{u}_j}{\partial x_j}\right)\frac{\partial \overline{u}_i}{\partial x_j}\right]^{1/2} \tag{3.15}$$

For RNG *k-ε* model, the turbulent eddy viscosity expression is

$$\nu_t = \nu\left[1+\left(\frac{c_{\mu}}{\nu}\right)^{1/2}\frac{\kappa}{\varepsilon^{1/2}}\right]^{2} \tag{3.16}$$

The values of the RNG *k-ε* model constants are:

$C_{\mu} = 0.0845$, $C_{\varepsilon 1} = 1.42$, $C_{\varepsilon 2} = 1.68$, $\sigma_k = 0.7179$, $\sigma_{\varepsilon} = 0.7179$, $\beta_0 = 0.012$ and $\eta_0 = 4.38$.

3.3.2.4.3. k-ω turbulence model

Wilcox [59] developed the *k-ω* model as an alternative to cope up with the deficiencies of *k-ε* model at the walls. The *k-ω* model is very similar in structure to *k-ε* model but the variable '*ε' is* replaced by the dissipation rate per unit kinetic energy '*ω'*. The advantage of *k-ω* model is that the '*ω'* equation is more robust and easier to integrate compared to the '*ε'* equation without the need of additional damping function. The *k*-equation in the *k-ω* model is written as,

$$\frac{\partial(\rho k)}{\partial t} + \overline{u}_i\frac{\partial(\rho \overline{u}_j k)}{\partial x_j} = \frac{\partial}{\partial x_j}\left(\frac{\mu_t}{\sigma_k}\frac{\partial k}{\partial x_j}\right) + \mu_t\frac{\partial \overline{u}_i}{\partial x_j}\left(\frac{\partial \overline{u}_i}{\partial x_j} + \frac{\partial \overline{u}_j}{\partial x_i}\right)\frac{\partial \overline{u}_i}{\partial x_j} - \rho k\omega \tag{3.17}$$

and the ω-equation is,

$$\frac{\partial(\rho\omega)}{\partial t}+\bar{u}_i\frac{\partial(\rho\bar{u}_i\omega)}{\partial x_j}=\frac{\partial}{\partial x_j}\left(\frac{\mu_t}{\sigma_\varepsilon}\frac{\partial\omega}{\partial x_j}\right)+\alpha\frac{\omega}{k}\mu_t\frac{\partial\bar{u}_i}{\partial x_j}\left(\frac{\partial\bar{u}_i}{\partial x_j}+\frac{\partial\bar{u}_j}{\partial x_i}\right)-\beta\rho\omega^2 \tag{3.18}$$

The replacement with the variable 'ω' allows better treatment in resolving the flow near the walls. Near the wall, the boundary layer is affected by viscous nature of the flow, so a very fine mesh is necessary to resolve the flow. However, the *k-ω* model will over predict the spreading rates around the free shear layer due to inaccurate prediction of eddy viscosity value. A comparison between *k-ω* and *k-ε* turbulence model is shown in Table-3.1. It is observed that *k-ε* model performed well in the shear layer flow while the *k-ω* model is excellent near the wall. This led to the development of the Shear Stress Transport (SST) model which aims to combine the advantages of these two models.

Table-3.1: Comparison between the *k-ω* and *k-ε* models.

	***k-ω* model**	***k-ε* model**
Sub layer	Robust Accurate Simple	Stiff Less accurate Complex
Log layer	Accurate	Length scale too large
Free stream	Inaccurate in free stream layer	Well defined

3.3.2.4.4. Shear stress transport (SST) k-ω model

In order to overcome the problem of free stream dependency of *k-ω* model and to prevent the over prediction of length scale near the wall by *k-ε* model, Mentor [67] introduced the SST *k-ω* model, which combines the positive features of both models. The idea is to employ the *k-ω* model near the wall whereas *k-ε* model near the boundary layer edge. To achieve this, *k-ω* model is multiplied by a blending function 'F_1' and the *k-ε* model is multiplied by '$(1-F_1)$', such that F_1

has a value of ‘*one*’ near wall region and switches to ‘*zero*’ at the boundary layer where k-ε model is recovered.

In the present thesis, the standard high Reynolds number k-ε model, RNG k-ε model and SST k-ω models have been used. The standard logarithmic wall function has been used near the walls to avoid fine grids. The value of y^+ near the walls is respected to be 30 – 100. The models adopted for specific simulations are given in the respective chapters. The turbulence intensity at the inlet is taken as 5% in all the simulations.

3.4. FREE SURFACE MODELLING

An interface between a gas and liquid is often referred to as a free surface. The reason for the "free" designation arises due to large difference in densities of gas and the liquid (ρ_w/ρ_a = 1000). Lower gas density means its inertia can generally be ignored compared to that of liquid. In this sense the liquid moves independently, or freely, with respect to gas. The only influence of gas is the pressure it exerts on the liquid surface. In other words, the gas-liquid surface is not constrained, but free. “Free surface flows” can be broadly classified into three groups based on the interfacial structures and topological distributions of the phases viz., *segregated flows*, *transitional* or *mixed flows* and *dispersed flows* [68]. The above flows can be explained by considering a closed container partially filled with a liquid and the other part occupied by a gas. The first class of flows occurs when the container is oscillating very gently with low amplitude and frequency and the two phases remain separated with a single well defined interface. *Mixed* or *transitional flows* occur when the frequency and amplitude are increased to the extent that the waves become unstable and break up with small bubbles that are trapped in the liquid. *Dispersed flows* occur when the container is shaken violently and the gas is suspended as small bubbles within the liquid. The study of *gas entrainment* in a fast reactor falls in the category of *mixed or* *transitional flows*. In the following discussion, we briefly review the different types of numerical approaches that have been used to model free surface flows.

3.4.1. Methods for Solving Free Surface Phenomena

All numerical simulations of flows require a discretisation or rationalization to allow numerical treatment of free surface flow on computers. There are two fundamental approaches as follows:

- *Eulerian Method*: uses a frame of reference fixed in space, and matter (fluids) moving through this frame of reference
- *Langrangian Method*: instead of using frame of reference uses marker particles, grid or mesh moving with the matter.

The Langrangian methods are less useful if strong distortions of the flow occur, or if the topology changes, for example, as moving boundaries merge or break up. Then, the frame of reference has to be reinitialized (remeshing or reordering of points), which may be very cumbersome. Eulerian methods, on the other hand, tend to be less accurate due to numerical diffusion. In the present application where strong distortion of free surface with gas entrainment is expected, an *Eulerian Method* is adopted.

3.4.1.1. Surface Height Method

Hirt and Nichols [15] extend the idea of interface marker particles by relating the reference points on the interface to points on a certain reference plane. The interface location is then defined by its height (*H*) or distance from the reference plane. Time evolution of the height is governed by,

$$\frac{\partial H}{\partial t} + u\frac{\partial H}{\partial x} + v\frac{\partial H}{\partial y} = w \tag{3.21}$$

where (*u, v, w*) are fluid velocities in the x, y, and z directions. This equation represents that the surface moves with the fluid. Finite-difference approximations to this equation are easy to implement. Furthermore, only the height values at a set of horizontal locations must be recorded so the memory requirements for a 3-D numerical solution are extremely small.

A major limitation of this method is that every reference coordinate can represent only one interface value. Therefore, it is not possible to predict situations where the reference coordinates can be multi valued (droplet break-up, breaking of waves etc.).

3.4.1.2. Marker and Cell (MAC) Method

The earliest numerical method devised for time-dependent free-surface flow problems was the Marker-and-Cell (MAC) method [12]. This scheme is based on a fixed Eulerian grid of control volumes. The location of fluid within the grid is determined by a set of marker particles (have no volume, mass) that move with the fluid as depicted in Fig. 3.3.

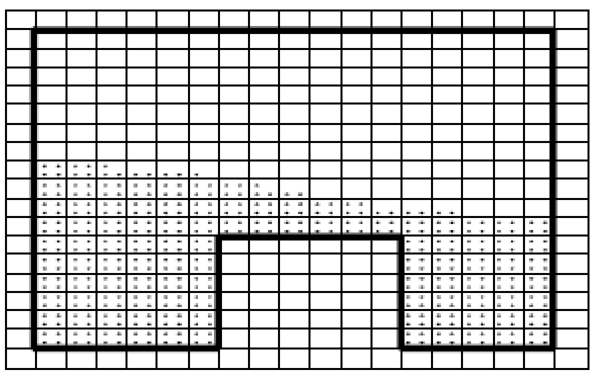

Fig. 3.3: Schematic representation of marker and cell (MAC) mesh layout [12].

Grid cells containing markers are considered occupied by fluid, while those without markers are empty (or void). A free surface is defined to exist in any grid cell that contains particles and that also has at least one neighboring grid cell that is void. Evolution of surfaces is computed by moving the markers with locally interpolated fluid velocities. Some special treatments were required to define the fluid properties in newly filled grid cells and to cancel values in cells that are emptied. The boundary conditions consist of assigning the gas pressure to all surface cells.

Velocity components are assigned to all locations on or immediately outside the surface in such a way as to approximate conditions of incompressibility and zero surface shear stress.

The success of MAC method in solving a wide range of complicated free surface flow problems are well documented in numerous publications [69]. One reason for this success is that the markers do not track surfaces directly, but instead track fluid volumes. Surfaces are simply the boundaries of the volumes, and in this sense surfaces may appear, merge or disappear as volumes break apart or coalesce. MAC [70] method is generally limited to 2-D simulations as it requires considerable memory and CPU time to accommodate the necessary number of marker particles and it fails in the regions involving converging/diverging flows.

3.4.1.3. Level Set Method

A continuous function, known as level set function was introduced by Osher and Sethian [71] over the whole computational domain. Level set method employs the idea of one fluid simulation. The implicit material boundary / interface is given by the zero set of the scalar field (ϕ) such that Γ: $\{(x,y,z) \mid \phi(x,y,z) = 0\}$ and

$$\phi(x,t) = \begin{cases} > 0 & \text{In fluid 1} \\ < 0 & \text{In fluid 2} \\ = 0 & \text{At boundary } \Gamma \end{cases} \tag{3.22}$$

Here ϕ is similar to a marker. The only difference is that $\phi = 0$ is exactly where the interface lies. The level set function is a scalar property associated with the fluids and is propagated with the fluids by solving a scalar transport equation given by

$$\frac{\partial \phi}{\partial t} + \overline{u}_j \frac{\partial \phi}{\partial x_j} = 0 \tag{3.23}$$

Moreover, normal and curvature of the level set is given by:

$$\hat{n} = \frac{\nabla \phi}{|\nabla \phi|} \qquad\qquad k = \nabla \cdot \frac{\nabla \phi}{|\nabla \phi|} \tag{3.24}$$

A general concern for curvature is the minimization of surface energy, which is related to surface tension. The calculation of surface tension force is solved by using continuum surface force (CSF) model of Brackbill et al., [72]. Level set method is easy to adopt but has the draw back that volume is not always conserved while advecting the interface. Such disadvantages can be corrected by applying a volume correction after each numerical advection.

3.4.1.4. Front Tracking Method

In a front-tracking method [72a], the fluid interface is evolved in time by updating an explicit representation of the interface in the form of elements or markers. It thus applies to problems which contain important singularities or jump discontinuities. The locations of the discontinuity surfaces are referred to as fronts. Front tracking employs two grid systems: (i) the grid located in the regions between the fronts, and (ii) a lower-dimensional grid defines the location of the jump in the solution variables. The dynamics of the front comes from the mathematical theory of Riemann solutions, which is an idealized solution of a single jump discontinuity for a conservation law. Nonlocal corrections to Riemann solutions provide the coupling between the solution values on these two grid systems.

Despite significant advances, front tracking method has shortcomings when it comes to dealing with topological singularities, e.g. break-up, merging etc.

3.4.1.5. Volume-Of-Fluids (VOF) Method

This method is based on the concept of fluid volume fraction. Within each grid cell (control volume), it is customary to retain only one value for each flow quantity, e.g., pressure, velocity, temperature, etc. Following this, the use of a single quantity (the fluid volume fraction 'α') in each grid cell, determines the interface position. The basic kinematic equation for fluid fraction is as follows;

$$\alpha(x,t) = \begin{cases} 1\, or\ 0 & \text{for a grid point in the liquid or gas} \\ 0 < \alpha < 1 & \text{for the interface} \end{cases} \tag{3.25}$$

Particular values of α are associated with each fluid and are evolved with its corresponding phase as shown in Fig. 3.4.

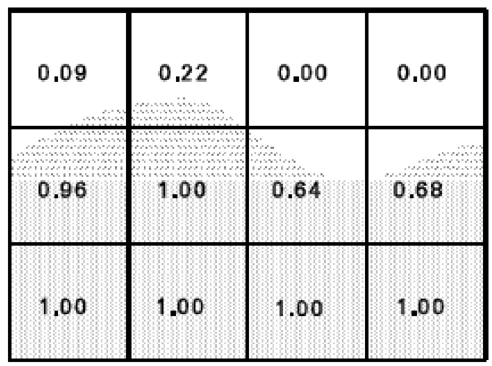

Fig. 3.4: Volume fraction on a discrete mesh [15].

Knowing this, the volume fractions in neighboring cells can be used to locate the position of fluid as well as its slope and curvature, within a particular cell. The transport equation for the liquid volume fraction α satisfies the transport equation as given by Eq. (3.23). From phase fraction information, geometric reconstruction of the interface shape is obtained.

Pioneering work on VOF methods goes back to Noh and Woodward [73], Ramshaw and Trapp [74], Hirt and Nichols [15] and their “SOLA-VOF” code, which has been widely used. There is a vast amount of literatures available that demonstrate the validity of VOF method. Situations such as rising bubbles [69], jet and droplet break-up [75], droplet impact [76] and dam break problems [77] etc. are simulated with various VOF methods. Several commercial CFD codes incorporate VOF method. This method is adopted in the present studies.

3.4.1.6. Line Interface Technique

The volume fraction "*α*" is the only phase information stored in VOF methods. Approximate locations are found from interface reconstruction. This is needed for advecting volume fraction for determining the local properties (density, viscosity etc.) and for better graphical representation. In earlier versions, known as SLIC (Simple Line Interface Construction) method [73], interfaces are approximated with either a horizontal or vertical line in each cell as depicted in Fig. 3.5.

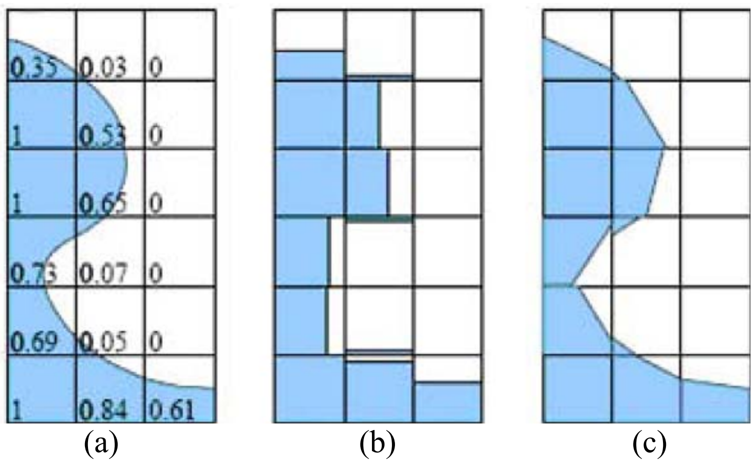

Fig. 3.5: Various line interface techniques, (a) a true interface, (b) SLIC and (c) PLIC [78].

More accurate reconstructions are possible with PLIC (Piecewise Line Interface Construction) methods, pioneered by Youngs [78]. Here, the interface is approximated by a straight line of arbitrary orientation (found from the fluid distribution in the neighboring cells) in each cell.

3.5. BOUNDARY CONDITIONS

The governing equations of free surface flows are elliptic in space coordinates and hence the boundary conditions for velocity components, k and ε/ω are needed to be specified on all the boundaries. For an unsteady laminar incompressible viscous flow, solution variables (φ) are to be specified as an initial condition. The velocity components are zero on solid walls (no-slip condition) and φ are to be mentioned at inflow boundary. At outlet, specified pressure or outflow boundary condition $\left(\frac{\partial u_i}{\partial n}=0\right)$ is to be specified. Furthermore, symmetric boundary condition $\left(\frac{\partial \varphi}{\partial n}=0\right)$ is supplied to take advantage of special geometrical features of the solution region.

For turbulent flow simulations, the standard practice is to use wall functions [59] close to the wall, where the variables change very sharply. This is required to avoid excessive grid refinement and associated high computational effort [55]. The details of boundary conditions for each specific problem are discussed in the corresponding chapters.

3.6. GRID INDEPENDENCE TEST AND CONVERGENCE

In all CFD simulations, a mesh independence test is important in order to achieve a statistically accurate and converged solution which means change of mesh will not affect the numerical solutions significantly. A mesh independence test is usually done by refining mesh resolution of the simulations gradually to achieve a constant solution. Another aspect in the CFD study is the residual of the solutions. The equations describing fluid flow are solved iteratively and hence residuals appear. A residual is usually targeted between four to six orders of magnitude of the original value to achieve convergence [79] of the solution to an acceptable level.

3.7. CLOSURE

The governing equations for fluid flow along with various mechanisms for capturing interface have been presented. Detailed flow boundary conditions, grid independent test and the solution procedure used for the simulations are presented in the respective chapters.

CHAPTER 4

NUMERICAL STUDIES ON LIQUID FALL INDUCED GAS ENTRAINMENT

4.0. FOREWORD

In a number of chemical engineering applications, a cover gas is maintained above a liquid pool. Also a large number of components remain partially submerged in the liquid pool with liquid flowing past these components. In a fast breeder reactor, argon gas is maintained above all the sodium pools and there is likelihood of argon entraining into sodium by a variety of mechanisms, which can cause unfavorable operational problems as listed below:

- A large number of gas bubbles which accumulate near the core possibly cause a reactivity fluctuation.
- Bubbles are nucleation sites for boiling or cavitation.
- If large bubbles can get trapped in a subassembly, burn out of fuel pins may occur.

Hence, it is important to mitigate the gas entrainment at the free surface of the hot pool. An extensive literature survey showed that scale down model experiments with water as simulant are a possible option to predict the gas entrainment behavior in prototype. The present study numerically explores the parameters responsible for the onset of liquid fall induced gas entrainment and its mitigation strategy. Various mechanisms responsible for gas entrainment and the pertinent literature have already been discussed in Chapter 2.

Investigation of the inception of gas entrainment in sodium pools can be performed in conjunction with interface tracking, using volume of fluids (VOF). However, the entrained gas bubbles are copious, but millimeter or so in size. It should be noticed that, compared to the size of reactor pool (~ 12 m in diameter), entrained gas bubbles are 3 to 4 orders lower in size.

Maintaining the grid resolutions dictated by the entrained gas bubbles would be computationally very intensive. Therefore, it would be necessary to develop lower order CFD models to identify conditions conducive to gas entrainment and judiciously couple them with global CFD tools. Furthermore a design solution to mitigate gas entrainment would necessitate a large number of parameters to be investigated to optimize the solution strategy. To this end, gas entrainment studies on Indian Prototype Fast Breeder Reactor (PFBR) which is in an advanced stage of construction, were carried out in two steps. In the first step, detailed investigations are carried out on a 2-D slab model employing the VOF method. It is found that free surface velocity is the main parameter which governs the process of entrainment, in addition to liquid properties. To confirm this, results obtained from 2-D transient VOF studies are verified through 2-D steady fixed grid simulation. Further, in order to confirm the conclusions derived from 2-D transient VOF and 2-D steady fixed grid simulations, 3-D transient VOF simulations were also carried out. Furthermore, a design solution to mitigate gas entrainment is proposed. In the second stage, a 3-D CFD model of PFBR hot pool is developed using fixed grid simulations. Following this, a circumferential baffle as a means for the mitigation of gas entrainment is proposed. The design optimization for the baffle position and size are systematically performed which will be discussed in detail in the next chapter.

4.1. SOLUTION METHODOLOGY

4.1.1. Governing Equations

The velocity and pressure fields are determined by solving the transient incompressible form of Navier-Stokes equations and continuity equation along with standard *k-ε* turbulence model. As the problem is associated with free surface, VOF method is used to track the interface between the liquid and gas phases, with a jump discontinuity between them. The detailed mathematical description of the two-fluid system is available in Hirt and Nichols [15] and its implementation through the general purpose CFD tool, FLUENT 6.3 [53] has already been discussed in chapter 3.4. In order to account the surface tension effect, the well known Continuum Surface Force (CSF) model, proposed by Brackbill et al., [72] has been adopted. This approach provides a robust formalism and accuracy in terms of curvature estimation. With this model, the inclusion of surface tension to the VOF calculation results in an additional source term in the momentum equation. The pressure jump across the liquid-gas interface can be written as;

$$p_1 - p_2 = \sigma\left(\frac{1}{R_1} + \frac{1}{R_2}\right) \tag{4.1}$$

where p_1 and p_2 are the pressures in the two fluids on either side of the interface and σ is surface tension coefficient with R_1 and R_2 as the radii of curvatures in two orthogonal directions. The surface curvature is computed from local gradients in the surface normal to the interface. If 'n' be the surface normal, defined as the gradient of α_l then we have $n = \nabla\alpha_l$. The curvature k_l, is defined in terms of the divergence of the unit normal, $\hat{n}$ as $k_l = \nabla \bullet \hat{n}$, where $\hat{n} = n/|n|$. Finally, the volumetric force (F_{vol}) in the momentum equation is

$$F_{vol} = \sigma \frac{\rho k_l \nabla\alpha_l}{0.5(\rho_l + \rho_g)} \tag{4.2}$$

where ρ_l, ρ_g and ρ are respectively liquid, gas and volume-averaged density values.

In order to validate the CSF model, movement of a gas bubble in a stagnant liquid is simulated. The properties of liquid are: density = 1000 kg/m^3, viscosity = 0.1 kg/m-s and surface tension coefficient = 0.09 N/m. The properties of gas are: density = 10 kg/m^3 and viscosity = 10^{-3} kg/m-s. The width, depth and height of the tank are 0.012m, 0.012m and 0.03m respectively (Fig. 4.1). The fluid properties and the tank size are as described in Annaland et al., [80]. The computed pressure distribution along a vertical line passing through the rising gas bubble is depicted in Fig. 4.2.

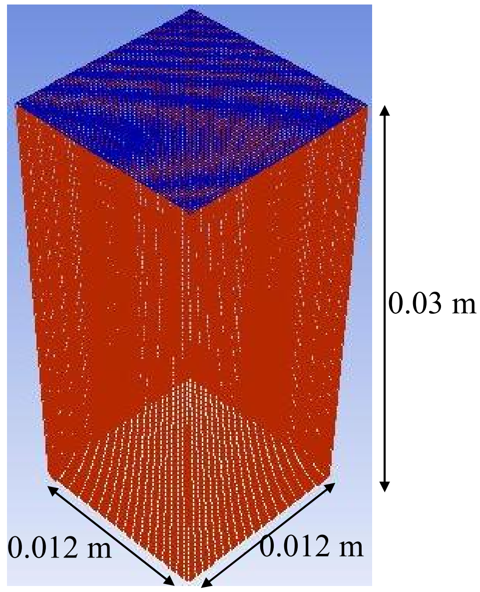

Fig. 4.1: Computational domain.

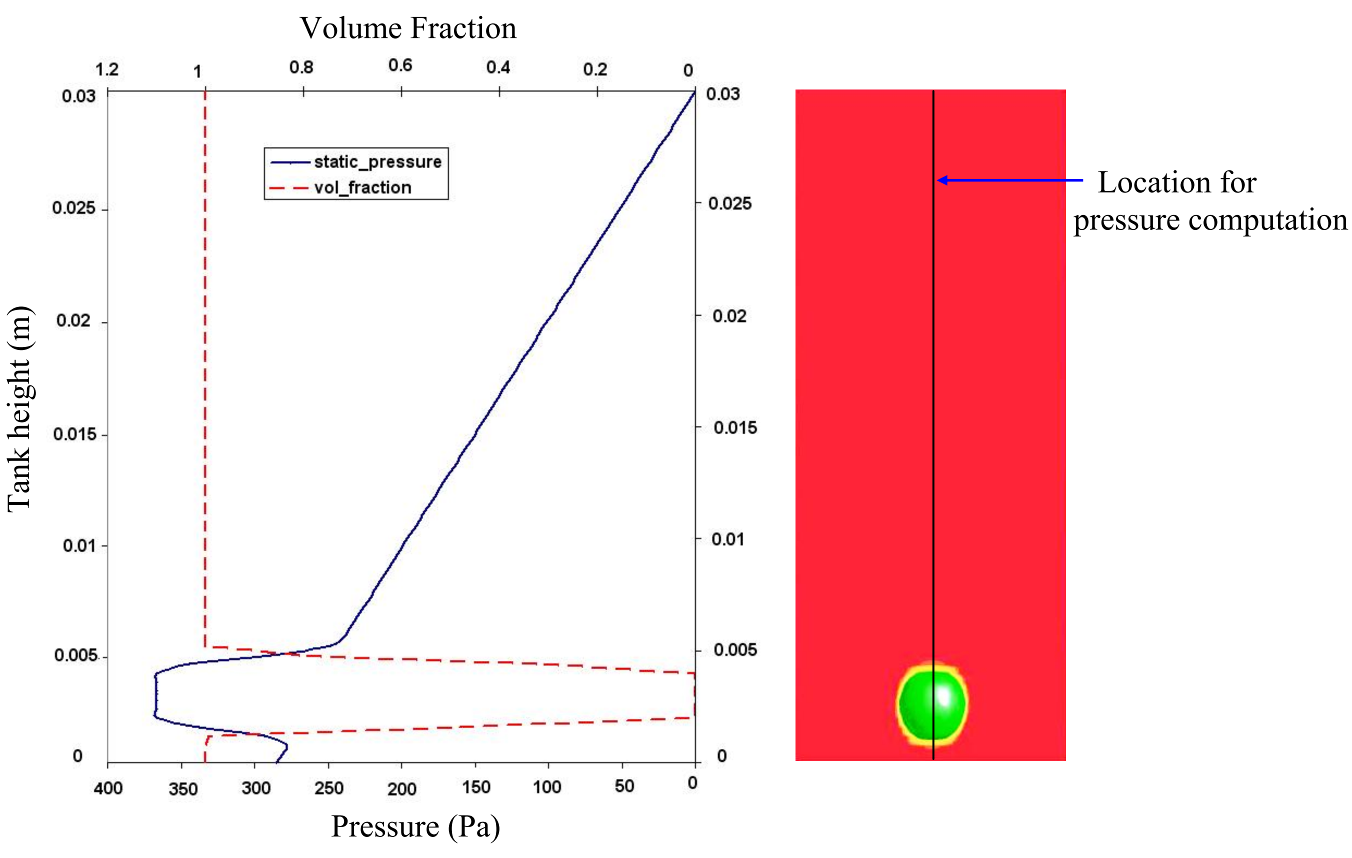

Fig. 4.2: Computed pressure jump.

It can be seen that the CSF model which is adopted in the present investigations, clearly predicts the pressure jump at the interface between the gas bubble and the surrounding liquid. The pressure jump computed by the code at the interface is ~ 127 Pa and this value compares very well with the value of ∇p computed from Eqn. (4.1), viz., 120 Pa, validating the proper implementation of the interface boundary condition.

Pressure-velocity coupling between the incompressible Navier-Stokes and continuity equations is resolved using the Pressure Implicit with Splitting of Operators (PISO) algorithm [52]. This pressure-based algorithm solves the momentum equations and pressure correction equation through a segregated solver. The convective and diffusive fluxes are combined using the first order upwind scheme. The temporal part has been solved by an implicit time marching technique with time step (Δt) determined by the CFL condition [81]. From phase fraction information, geometric reconstruction of the interface shape is achieved. To declare convergence at any time level, the absolute error in the discretized momentum and continuity equations is set to a value below 10^{-4}.

4.1.2. Validation for the Interface Dynamics

A benchmark problem widely studied by experimental and computational researchers associated with free surface flow is the "Dam Break Problem" [77]. An elaborate description of the experimental setup related to the same is available in Koshizuka and Oka [82]. The setup consists of a slab model of an open tank of width 4 m and height 3 m. Inside the tank, a water column of width 1 m and height 2 m is maintained by a thin wall. The rest of the volume is occupied by air. Top face of the tank is open to atmosphere. During the start of the transient, the wall collapses allowing the water column to deform, slosh and finally settle to a new equilibrium level. A schematic of the broken dam problem is depicted in Fig. 4.3. Predicted results of interface movement between water and air are depicted in Fig. 4.4 along with the numerical results reported by Violeau and Issa [83]. It is clear that the interface is well predicted in the present simulation.

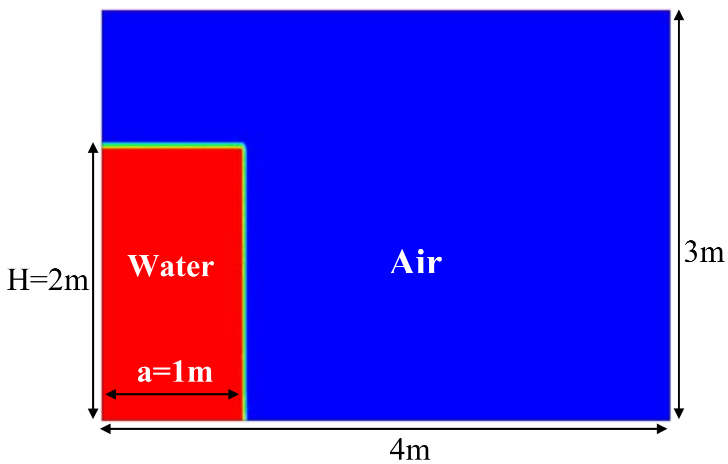

Fig. 4.3: Schematic of the broken dam problem.

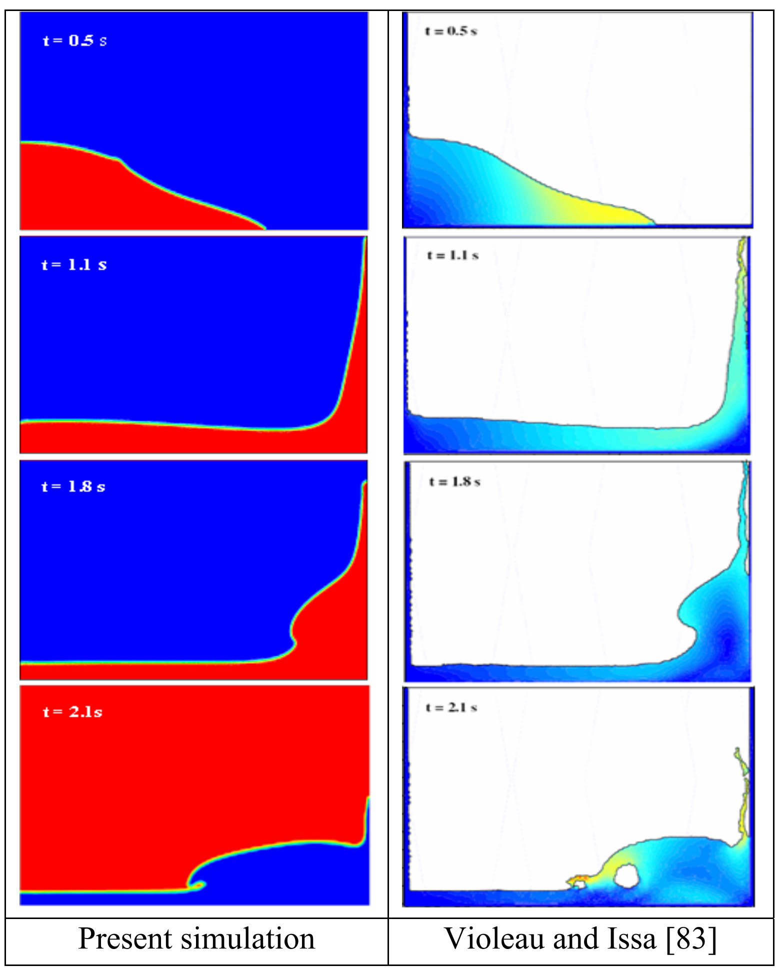

Fig. 4.4: Water-air interface at various time steps.

Figure 4.5 depicts reduction of water level on the left boundary as a function of time, along with the reported experimental results of Koshizuka and Oka [82] and numerical results of Violeau and Issa [83]. The level decreases as water flows towards the right wall. The instantaneous location of interface front at the bottom wall is depicted in Fig. 4.6 along with the experimental [82] and the numerical data [83]. It is clear that the present results agree very well with the published data demonstrating the validity of the VOF method employed.

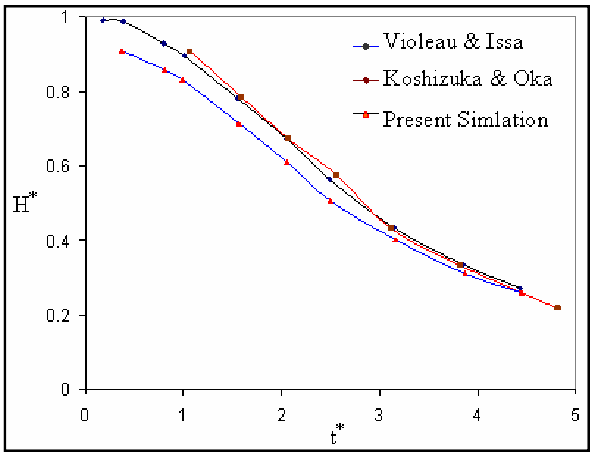

Fig. 4.5: Reduction of water level on the left boundary as a function of time

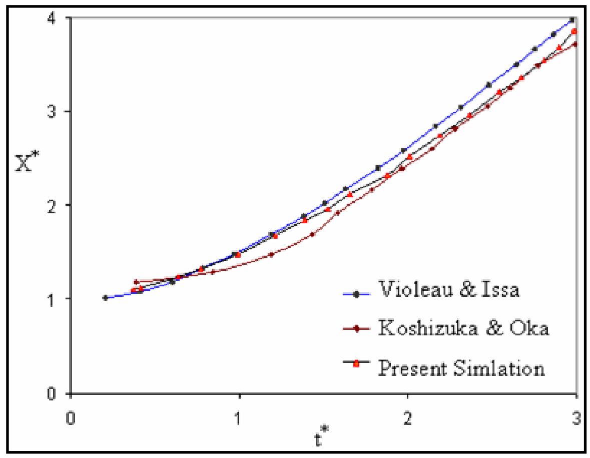

Fig. 4.6: Distance traveled by the interface front

X^* = X/a (X = distance traveled by the collapsing water column, a = width of water column); t^* = t/sqrt(a/2g) where t = time; H^* = H/2a, H = height of the water column

4.2. ESTABLISHMENT OF FREE SURFACE VELOCITY LIMIT

4.2.1. A 2-D Model Problem

After satisfactory validation of the method, numerical simulations are carried out to establish maximum permissible free surface velocity to avoid gas entrainment effects for a 2-D model flow. VOF based CFD simulations were performed on idealized 2-D and 3-D slab models of FBR hot pool. While detailed parametric studies have been carried out in two-dimensions, limited confirmatory studies have been carried out in 3-D model, owing to limitations in both the computational resources and number of parameters involved. The computational domain considered in the 2-D studies is shown in Fig. 4.7.

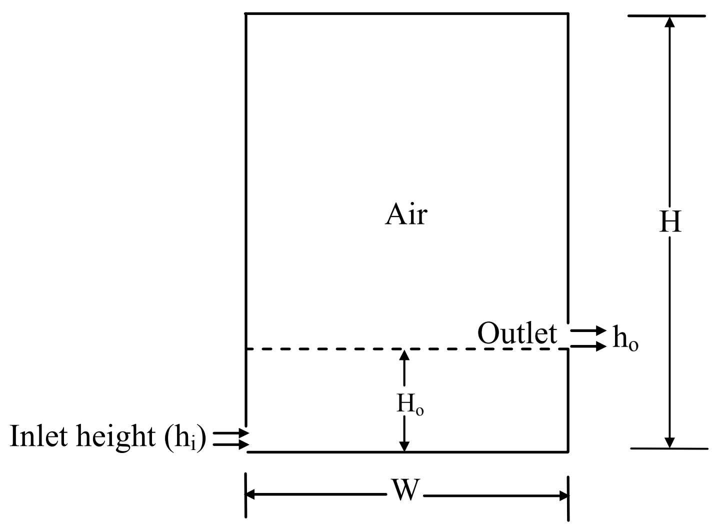

Fig. 4.7: Idealized flow domain of interest with geometric details for 2-D studies.

The flow domain consists of an inlet attached at the bottom of the left wall, and an outlet on the right wall at a height of H_o from the bottom. The inlet models the flow entering hot pool through axial gap between core and control plug while the outlet models flow leaving the hot pool into an Intermediate Heat Exchanger (IHX) (Fig. 1.4b). Features of the idealized model geometry, viz., horizontal width of tank, height of the inlet and inflow velocity have been systematically varied. The fluids considered for simulations are air (lighter fluid) and water (heavier fluid). The surface tension coefficient (σ) at the interface between the fluids is taken as 0.07 N/m. The Reynolds number of the flow is varied in the range of 5×10^4 to 3×10^5, inline with the practical range of values. The spatial mesh resolution is varied from 2 mm to 0.5 mm. Hence, the present model is restricted to predict bubbles of sizes of the order of mm only. Further, the focus of the study is only to predict conditions for onset of gas entrainment and not quantification of entrainment rate or distribution bubbles inside the liquid pool. Hence, the present mesh resolution may be considered to be acceptable for the present purpose. Close to the no-slip walls, the mesh resolution is such that the y^+ value varies from 20 to 30. Total number of mesh points used in the numerical simulation is varied from 7.5×10^3 to 4.5×10^4. Inlet is imposed with a constant velocity boundary condition, while a constant pressure condition is imposed at both the outlet boundary and at the top of the tank. No-slip boundary condition is applied on the side and bottom walls of the container. Liquid, which is heavier than air, is initially filled upto the outlet window. Inlet velocity is varied from 0.5 to 1 m/s and the inlet height is varied from 0.01 to 0.02 m. The width and elevation of the outlet window are fixed throughout the simulation. The tank height is varied to ensure that there is no overflow. Detailed case studies that were conducted are presented in Table-4.1.

Table – 4.1: Parametric studies considered for the 2-D VOF simulations.

Case No:	h_{in} (m)	h_o (m)	W (m)	H (m)	V_{in} (m/s)	$Re \times 10^5$
A	0.01	0.01	0.1	0.3	0.50	0.50
					0.75	0.75
					1.00	1.00
B			0.2		0.50	1.00
					0.75	1.50
					1.00	2.00
C			0.3		0.50	1.50
					0.75	2.25
					1.00	3.00
D	0.02		0.1	0.6	0.50	0.50
					0.75	0.75
					1.00	1.00
E			0.2		0.50	1.00
					0.75	1.50
					1.00	2.00
F			0.3		0.50	1.50
					0.75	2.25
					1.00	3.00

4.2.2. Dynamic Evolution of Gas Entrainment

Different phases of gas entrainment process are captured in the 2-D numerical simulations. Unsteady fluid flow simulations are carried out in the tank with initial water level upto the bottom of the outlet window (Fig. 4.8a). Due to the imbalance between the rates of inflow and outflow, the water level rises. Such a rise is large at the beginning of the transient when the window submergence is low and hence the outflow is small. This results in fast swelling of liquid adjacent to the right wall topping over to form liquid fall induced gas entrainment. Gas entrainment essentially refers to the formation of at least one gas bubble surrounded by liquid on all sides. In Fig. 4.8(b) such an entrapment of gas bubble, which is about to form has been termed as ‘inception of entrainment’. As the water level rises further, both the free surface velocity and the free surface gradient decrease. For some specific conditions, further gas entrainment ceases (Fig. 4.8c), which is referred as ‘end of entrainment’. Note in particular, presence of gas bubbles which are dragged downwards (see Fig. 4.8c). During the temporal evolution, a dynamic equilibrium between the outflow and inflow is reached. In some cases, especially with low inlet velocities, no entrainment is found to happen as seen in Fig. 4.8(d).

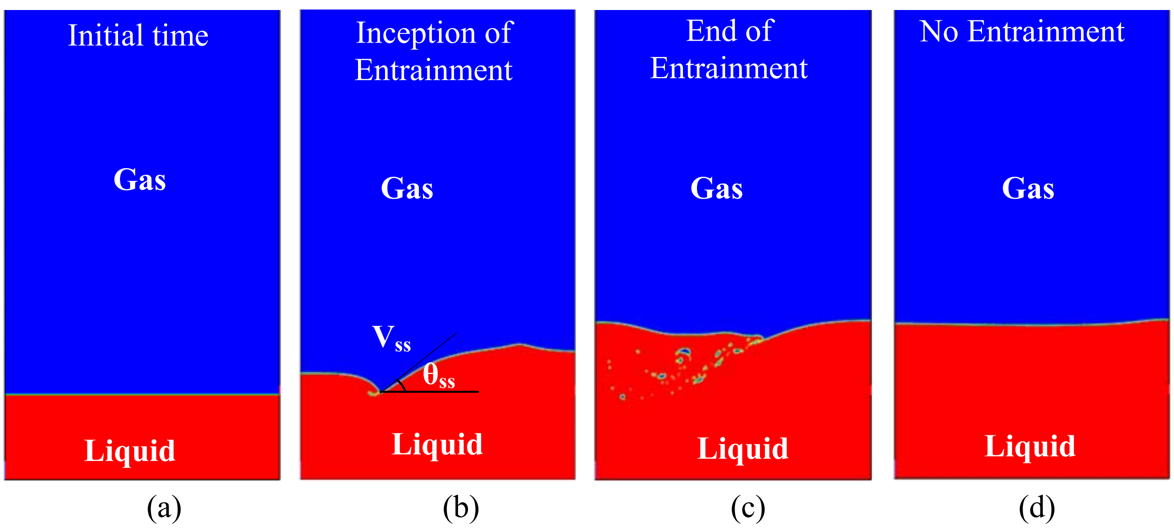

Fig. 4.8: Different phases of gas entrainment. Air-water interface is captured using VOF technique: (a) Initial time, (b-c) gas entrainment and (d) no entrainment case.

4.2.3. Inception of Entrainment

Critical examination of transient free surface characteristics indicate that two local parameters, viz., (i) the re-submergence angle (θ_{ss}) and (ii) the maximum free surface velocity (V_{ss}) affect gas entrainment. The re-submergence angle refers to the maximum gradient formed on the swollen surface as shown in Fig. 4.8(b). The influence of inlet liquid velocity on θ_{ss} and V_{ss} are obtained, at the beginning of gas entrainment (see Table-4.2).

Table-4.2: Determination of the inception of gas entrainment through parametric studies.

h_{in} (m)	W (m)	V_{in} (m)	Fr*	θ_{ss} (degree)	V_{ss} at start (m/s)	Occurrence of Entrainment
0.01	0.1	0.50	1.36	10.4	0.220	no
		0.75	3.73	27.9	0.604	yes
		1.00	4.00	48.7	0.648	yes
	0.2	0.50	1.42	7.10	0.229	no
		0.75	2.73	17.2	0.443	yes
		1.00	2.89	29.9	0.467	yes
	0.3	0.50	1.03	3.70	0.166	no
		0.75	1.95	8.60	0.315	no
		1.00	2.89	19.1	0.468	yes
0.02	0.1	0.50	1.23	6.60	0.207	no
		0.75	3.13	28.2	0.506	yes
		1.00	3.66	41.4	0.592	yes
	0.2	0.50	1.82	7.10	0.293	no
		0.75	3.91	24.7	0.632	yes
		1.00	3.30	20.8	0.534	yes
	0.3	0.50	1.02	5.80	0.172	no
		0.75	2.69	18.4	0.435	yes
		1.00	3.87	25.4	0.626	yes

From table 4.2, it can be observed that, there is no gas entrainment if the magnitude of free surface velocity is less than 0.315 m/s. However, gas entrainment is imminent for $V_{ss} > 0.435$ m/s. Furthermore, it is observed, that at the free surface the magnitude of horizontal velocity component is much higher than that of the vertical component. Also, gas entrainment occurs when the re-submergence angle is greater than 17°, and no entrainment is noticed for θ_{ss} below 10°. Furthermore, there appears to be a strong correlation between re-submergence angle and the magnitude of free surface velocity. To explore the dependency between θ_{ss} and V_{ss}, a plot between the two is presented in Fig. 4.9. Here, a linear relation between V_{ss} and θ_{ss} can be noticed with a distinct demarcation between entrainment and no entrainment cases. Since the latter depends on the former, it is surmised that the value of free surface velocity alone is adequate to infer gas entrainment in open liquid pools.

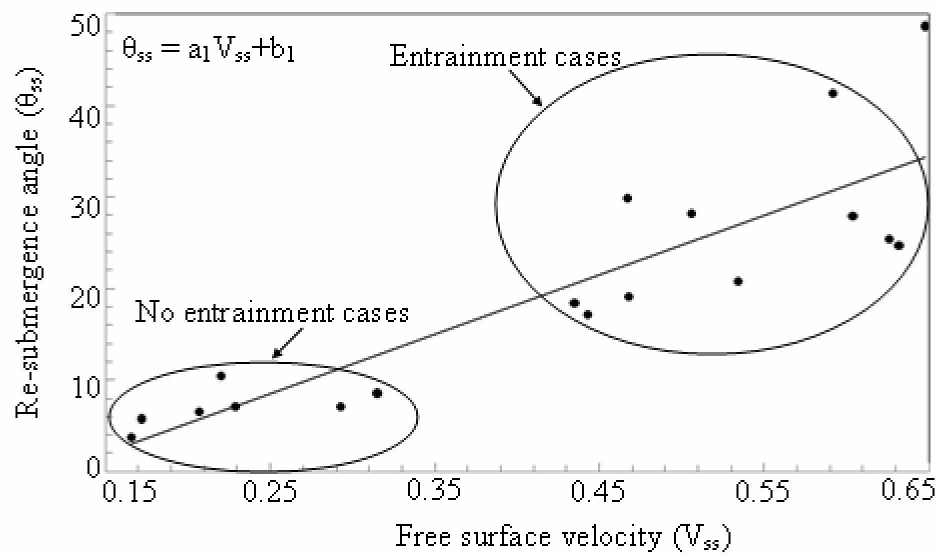

Fig. 4.9: Dependence of re-submergence angle on the free surface velocity

4.2.4. End of Entrainment

During the temporal evolution, free surface swells and the liquid level in the tank fluctuates, while the free surface velocity and re-submergence angle change with time. Long after the inception, further gas entrainment ceases to exist in most of the cases when the free surface conditions are no longer conducive. The free surface characteristics at this instant are presented in Table-4.3.

Table-4.3: Parameters at the end of gas entrainment. The values of θ_{ss} and V_{ss} below refer to re-submergence angle and free surface velocity at the end of entrainment.

h_{in} (m)	W (m)	V_{in} (m/s)	Fr*	θ_{ss} (degree)	V_{ss} at end (m/s)
0.01	0.1	0.75	2.50	22.2	0.403
		1.00	2.20	15.9	0.356
	0.2	0.75	2.69	16.7	0.436
		1.00	3.10	17.4	0.424
	0.3	1.00	2.63	14.9	0.425
0.02	0.1	0.75	2.33	18.2	0.377
		1.00	2.40	19.9	0.388
	0.2	0.75	2.74	12.0	0.443
		1.00	2.68	12.7	0.433
	0.3	0.75	2.87	14.9	0.384
		1.00	3.55	14.6	0.475

Within the range of validity of the present investigation, it is seen that when entrainment ceases, the free surface velocity is less than 0.5 m/s in all the cases, with corresponding re-submergence angle between 12° to 22°. Thus it can be concluded that, for the present tank geometry, when the free surface velocity is less than 0.4 m/s, gas entrainment is less likely in the liquid pools.

4.2.5. Parameters Influencing Gas Entrainment

In order to establish the relationship between θ_{ss} and V_{ss}, simple dimensional arguments may be employed with the aid of Buckingham's π-theorem [84]. Assuming θ_{ss} is a function of V_{ss}, liquid density, surface tension and gravity (g), it can be shown that,

$$\theta_{ss} = f\left(\frac{\rho V_{ss}^{4}}{\sigma g}\right) \tag{4.3}$$

The term on RHS of Eq (4.3) may be interpreted as the product of Weber number ($\rho V^2 h/\sigma$) and Froude number (V^2/gh). Fourth root of this product can be defined as a modified Froude number (Fr^*). A linear fit between Fr^* and θ_{ss} ensues as depicted in Fig. 4.10. The critical value of Fr^* for the onset of gas entrainment can be noticed to be above 2.0.

$$Fr^{*} = V_{ss}\left(\frac{\rho}{\sigma g}\right)^{1/4} \tag{4.4}$$

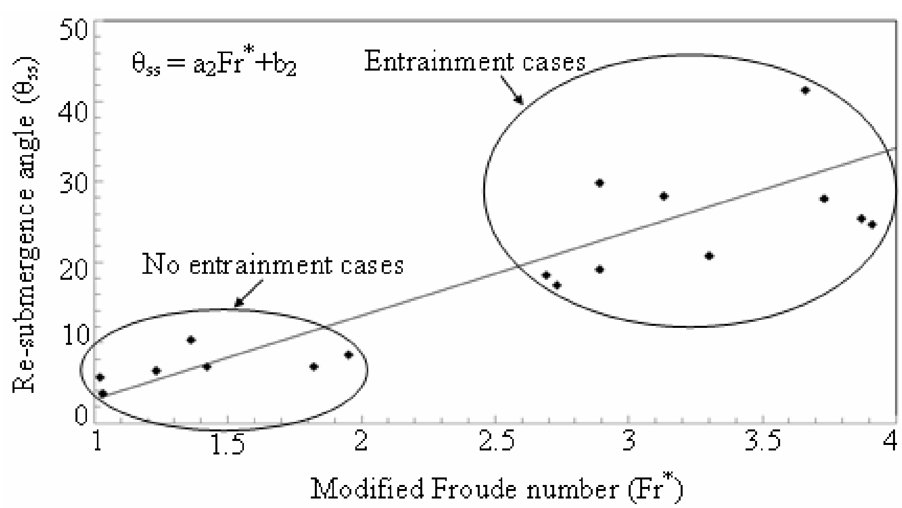

Fig. 4.10: Variation of re-submergence angle as a function of Fr^*.

4.3. SENSITIVITY ANALYSIS

Detailed sensitivity analysis has been carried out to understand the influence of various parameters involved in gas entrainment, viz., density, surface tension, acceleration due to gravity and viscosity. Decrease in liquid density or increase in surface tension was observed to mitigate gas entrainment for identical velocity and geometrical conditions. This is because any change in these parameters leads to reduction in Fr^* value which is clearly observed from the Fig. 4.11. However, change in viscosity is found not to affect entrainment characteristics.

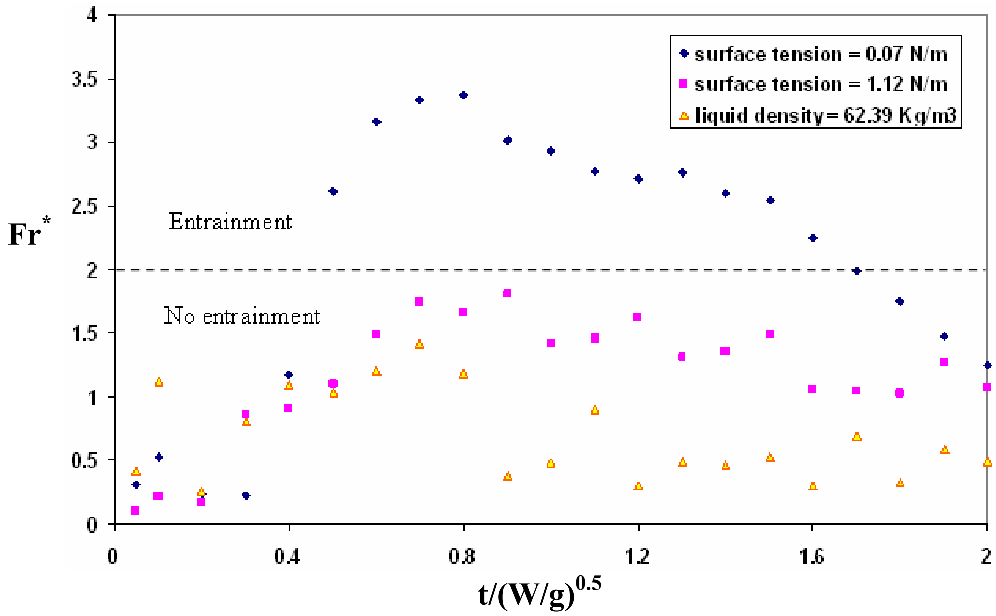

Fig. 4.11: Sensitivity analysis for liquid properties.

4.4. VERIFICATION OF THE CRITERION IN FIXED GRID SIMULATION

The 2-D VOF results obtained in transient simulations are verified in the process of 2-D steady fixed grid simulation. In the 2-D VOF simulations, we have measured the free level height at two positions, viz., (i) where the inception of gas entrainment starts and (ii) when gas entrainment stops in one of the 2-D results. These levels were considered for steady state fixed grid simulations. The boundary conditions are maintained to be same as that of 2-D VOF case except that the top wall is maintained as free slip wall. The measured horizontal velocities for both the cases, i.e., start and end of entrainment in fixed grid simulations are compared with the corresponding 2-D VOF results. This comparison is depicted in Figs. 4.12 and 4.13 respectively. The magnitudes of free surface velocity in both the cases are somewhat comparable. The pattern of recirculation regions are well captured in both the simulations which are evident from the figures. These comparisons are satisfactory.

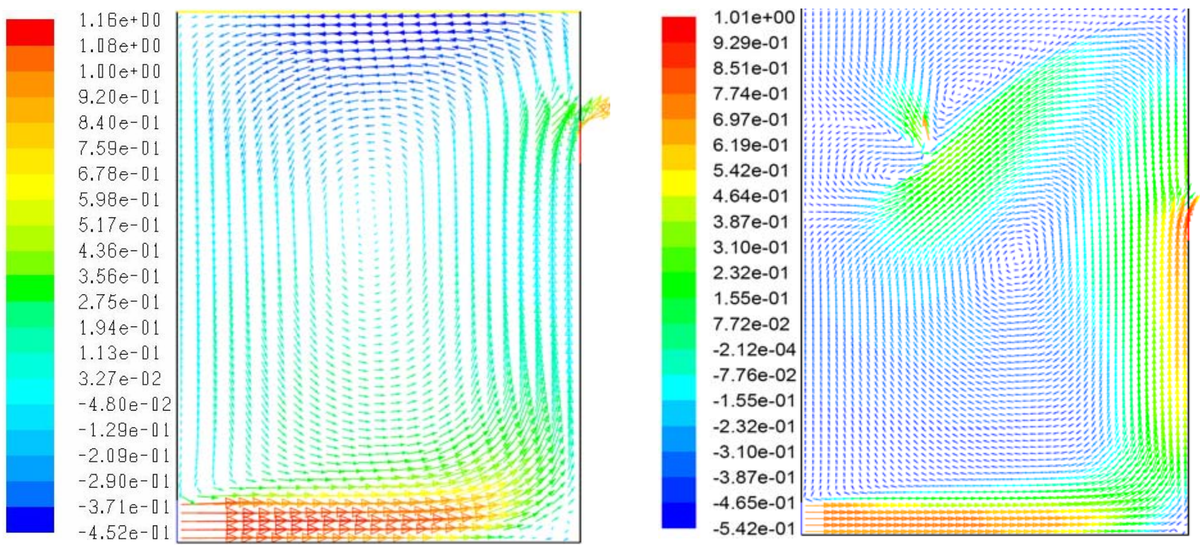

(a) (b)

Fig. 4.12: Velocity vectors at the inception of entrainment (a) fixed grid simulation and (b) 2-D VOF simulation.

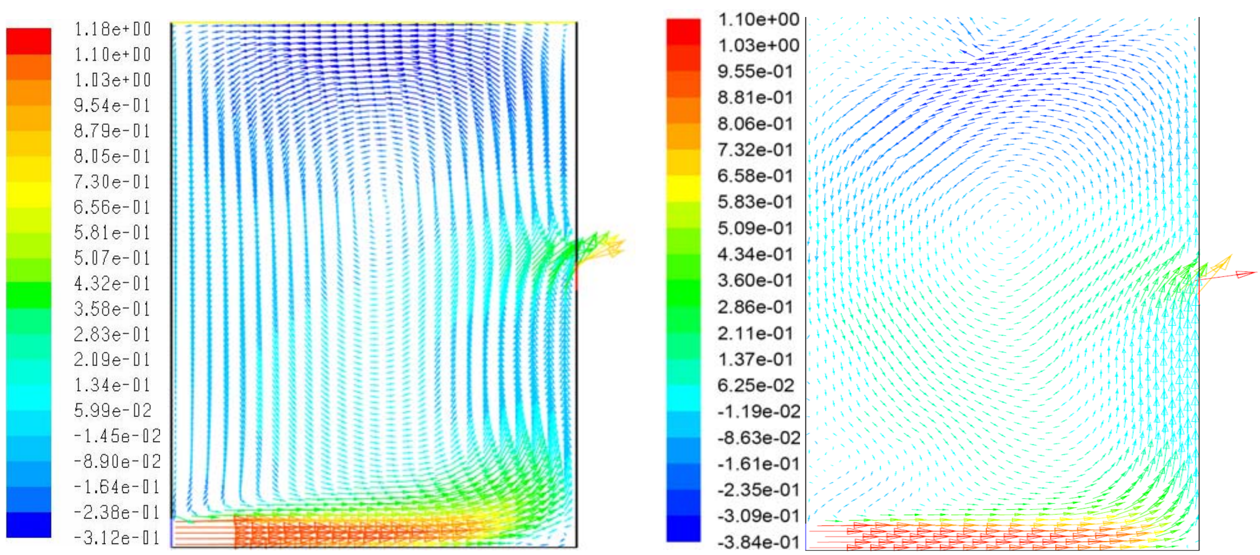

(a) (b)

Fig. 4.13: Velocity vectors at the end of entrainment (a) fixed grid simulation and (b) 2-D VOF simulation.

4.5. SIMULATIONS ON 3-D MODELS

The 2-D tank simulations have been extended to 3-D rectangular tanks for two cases. The computational domain for 3-D investigation consists of a rectangular tank of 0.1 m width and 0.3 m in height. Total number of grid points used for the simulations is about 3×10^5 with a mesh size of 0.5 mm. To minimize the computational expenditure, only two cases with different velocities, viz., 0.5 m/s and 1 m/s have been considered. For an inlet velocity of 0.5 m/s, no entrainment was observed, which closely resembles the corresponding 2-D results. But inception of gas entrainment starts for an inlet velocity of 1 m/s resulting in a free surface velocity of 0.67 m/s at the inception of entrainment, which ceases at a later time when this value reduces. This trend is in good agreement with the 2-D simulations. The predicted distribution by VOF at three different vertical planes is shown in Fig. 4.14, when the inlet velocity is 1 m/s. Further, it can be noticed that the entrained gas bubbles break up into smaller bubbles and move towards the free surface. However, the motion of these bubbles is governed by the local force balance at different spatio-temporal positions.

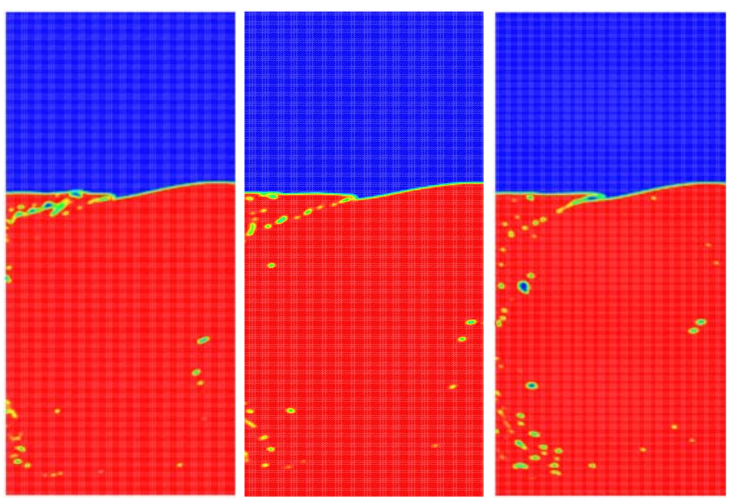
(a) (b) (c)

Fig. 4.14: 3-D numerical simulations using VOF method (a) front face, (b) middle face and (c) rear face of the rectangular tank indicating gas entrainment into the liquid.

4.6. CLOSURE

Gas entrainment in pools by liquid fall induced gas entrainment mechanism has been investigated by 2-D simulations performed on slab models. The free surface deformation has been captured by VOF method. Validity of the 2-D simulation has been established against 3-D VOF simulation. Parametric studies on ideal hot pool model of fast breeder reactor indicate that liquid fall induced gas entrainment primarily depends on free surface velocity, re-submergence angle and a modified Froude number (Fr^*). Gas entrainment into the liquid pool is found to take place, if the value of Fr^* exceeds 2.0. By a fixed grid 3-D simulation of the reactor hot pool, the velocity distribution at the free surface could be determined. Using the sodium properties, viz., density and surface tension coefficient at appropriate temperatures, the distribution of Fr^* at the free surface could be determined to assess the risk of gas entrainment.

CHAPTER 5

IDENTIFICATION OF A PASSIVE DEVICE FOR REACTOR HOT POOL

5.0. FOREWORD

In the previous chapter, investigations on 2-D and 3-D model flow problems have been carried out. From these simulations, it was demonstrated that, re-submergence angle, free surface velocity and the Froude number (Fr^*) essentially characterize the onset of liquid fall induced gas entrainment in the hot pool of an FBR. The criterion established in the previous chapter is used to understand gas entrainment risk in the hot pool of Indian prototype FBR (PFBR). Towards this, 3-D flow distribution in the hot pool of PFBR is determined by a fixed grid numerical simulation. From the predicted free surface velocity, the risk of gas entrainment is assessed. It shall be highlighted that only steady state simulations need to be carried out as the requirement is only to predict time-averaged free surface velocity distribution. This distribution is used to compute the maximum value of Fr* at the free surface, which is an indicator of risk of gas entrainment. The CFD model adopted for this purpose is validated against available 1/4th water scale model of PFBR. Simulation of pool hydraulics in PFBR is attempted after gaining adequate understanding of parameters that influence gas entrainment. In the case of hot pool, buoyancy force is also expected to play a role. However, due to inertial dominance, mixed convection parameter, Richardson number (Ri) (ratio of buoyancy force to inertia force) is observed to be very small (Ri << 1) [85]. Hence, the flow is in the forced convection regime under full power condition, when gas entrainment is of major concern. However, either under low power operation or shut down phase, the buoyancy will have some influence on the dynamics of the fluid flow. Gas entrainment is not of much concern under low power condition. Hence, in the present study only hydrodynamic aspects of PFBR hot pool have been investigated. Towards this, a quadrant of the hot pool is modeled along with internal submerged components such as IHX, Decay Heat Exchanger (DHX), Primary Sodium Pump (PSP) etc as close to reality as possible. In particular, attention is focused on the parameters that influence gas entrainment.

5.1. COMPUTATIONAL MODEL FOR PFBR HOT POOL

The primary liquid sodium (1.15×10^7 kg) contained inside the main vessel of PFBR can be approximately bifurcated by a thin structure known as inner vessel, into hot pool (~ 547°C) and cold pool (~ 397°C). Primary sodium flows from hot pool to cold pool on the shell side of IHX. The primary sodium inlet window of IHX is submerged at a depth of 1.4 m below the hot pool. Four decay heat exchangers are also submerged in the hot pool, apart from two primary sodium pumps located in the cold pool. Control plug located above the core subassembly (SA) diverts the axial hot sodium from the subassembly into a radial stream. A horizontal lattice plate (with 60% porosity) located at 0.475 m above the subassembly top provides support for core monitoring of thermocouples. To exploit symmetry and to reduce too many detailed calculations, simulations are performed on a quadrant of the hot pool domain.

Three dimensional computational domain considered in the present study comprises of sodium in inner vessel and hot pool components, viz., IHX, DHX, standpipe of primary sodium pump, control plug, lattice plate, anti stratification porous skirt, upper stay plate, lower stay plate etc. (see, Fig. 5.1(a)). The flow entering the control plug is 15 % of the total core flow. All the subassemblies including fuel, blanket, reflector, storage and shielding subassemblies etc. have been modeled and sodium flow velocity has been specified at the top of subassemblies (SA). The flow is isothermal at 547°C. The flow enters hot pool through the axial gap between core and control plug and leaves the hot pool through the IHX. The Reynolds number based on IHX diameter as the charactestics length scale, is of the order of 10^6. The flow domain of interest and corresponding volume discretization are shown in Fig. 5.1 with isometric and sectional views. The location of the circumferential baffle plate on which optimization studies are performed is also indicated.

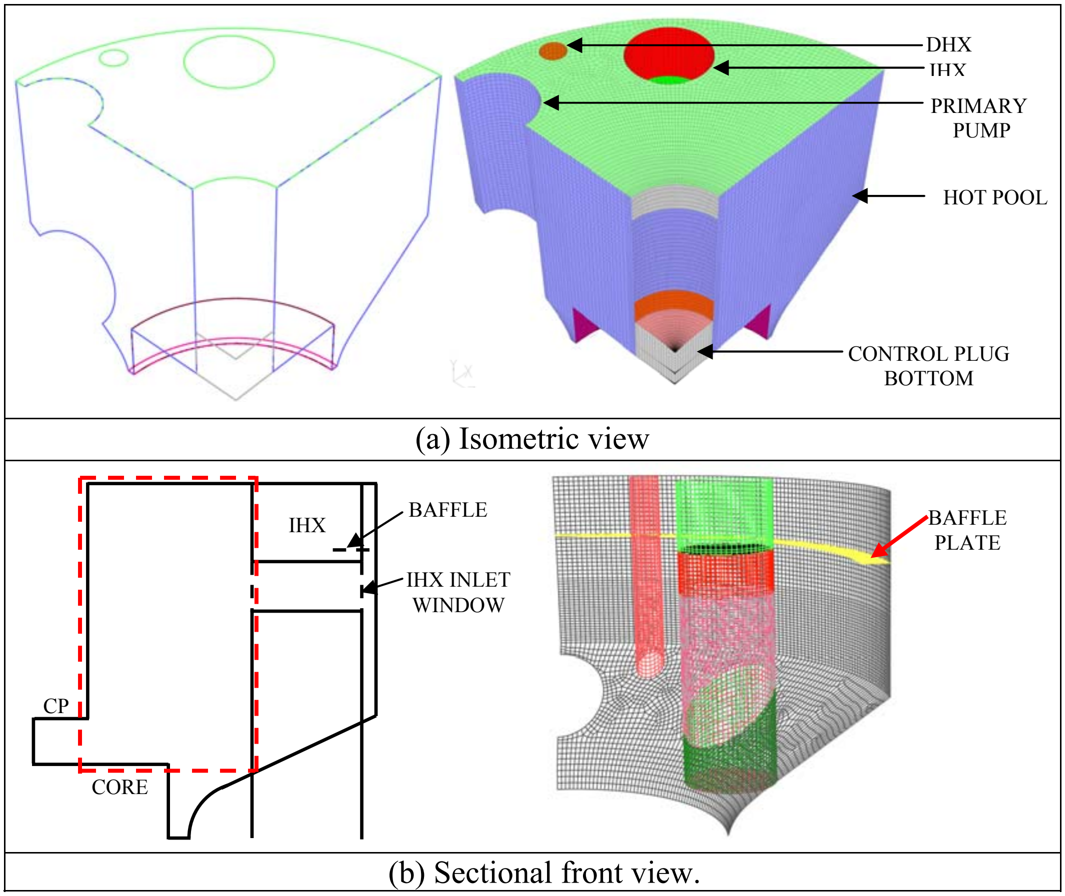

(a) Isometric view

(b) Sectional front view.

Fig. 5.1: 3-D computational domain and global grid pattern of 90° sector model of PFBR hot pool: (a) isometric view and (b) sectional front view (red dotted line shows the ideal slab model considered for 2-D simulation). Note in particular, the location of a circumferential baffle.

5.2. COMPUTATIONAL DETAILS

As already explained, Reynolds averaged Navier-Stokes equations require modeling of Reynolds stresses. A variety of two equation closure models, such as *k-ε, k-ω,* RNG *k-ε* models are available in the literature [59-60, 66]. The evaluation of these models is carried out through extensive testing and numerical experimentation. Based on the performance of these models, RNG k-ε model was chosen for further investigation. Mass flow rate at the inlet is specified as the boundary condition and imposed at core subassemblies as well as, at control plug shell. A constant pressure condition is imposed at the outlet boundary. No-slip boundary condition is applied on all the solid walls. Specific porosity and resistance coefficients are enforced on the anti stratification porous skirt (radial porosity of 10 % with a pressure loss coefficient of 250) and lattice plate (axial porosity of 60 % with pressure loss coefficient of 1.5). IHX tube bundle is modeled as a porous body with anisotropic porosity and flow resistance values, estimated from Zukauskas correlation [86].

5.3. GRID INDEPENDENCE STUDY

In order to choose the right finite volume grid to be adopted for the prediction of 3D velocity distribution in PFBR hot pool, three different mesh sizes have been adopted in the IHX window and free surface regions which are of interest in the present simulation. The mesh size varies from 10 mm to 100 mm respectively. Close to the walls, the mesh size is controlled by monitoring the y^+ value to be in the range of 20 ~ 30. The number of control volume cells employed for three different grid sizes are, 103322, 198036 and 355540. The maximum free surface velocity predicted for the three mesh sizes specified above are, 1.18, 1.15 and 1.14 m/s. It can be noticed that, the deviation between the last two free surface velocities is less than 1 %. Hence, all the computations reported in this study have been carried out using the intermediate a mesh size of 198036 grid points.

5.4. VALIDATION AGAINST EXPERIMENTS

The present investigation benefits from the detailed hydraulic experiments on a 1/4th scale model of PFBR hot pool conducted by Banerjee et al., [87]. Towards validating the hot pool CFD model, the 1/4th scale experimental set-up is numerically simulated by scaling by a factor of 4.

The inlet velocity magnitudes have been reduced by half to enforce Froude number similarity. The velocity distribution at the free surface predicted by the 3D CFD model as against measured experimental values at 23 points, is depicted in Fig. 5.2. It is noticed that the flow at the free surface is predominantly radial from inner vessel towards control plug with a maximum velocity of ~ 0.6 m/s. The maximum free surface velocity measured is ~ 0.58 m/s, while the corresponding value from numerics is ~ 0.5 m/s. The maximum deviation between the computational and experimental data is about 17 %. In a holistic sense, the predicted flow distribution is found to compare well with the measured experimental data.

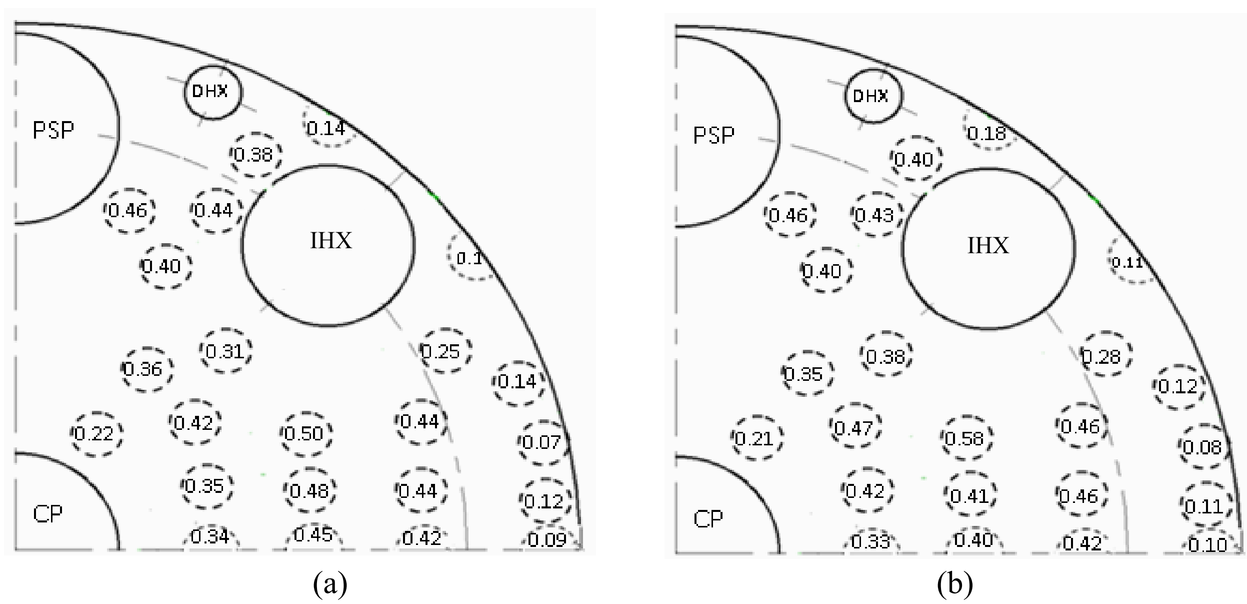

Fig. 5.2: Velocity (m/s) distribution at the free surface for 1/4th scale model (a) present numerical simulation and (b) experimental measurements of Banerjee et al., [87].

Detailed velocity distribution at the entry to IHX at different angles is presented in Fig. 5.3. The experimental measurements of Banerjee et al., [87] are superimposed against the present computational result. In order to find velocity distribution around IHX inlet window, measurements were performed by Banerjee et al., [87]. To bring clarity to the comparison exercise, the location around the periphery and its corresponding elevations of IHX are shown in Fig. 5.4.

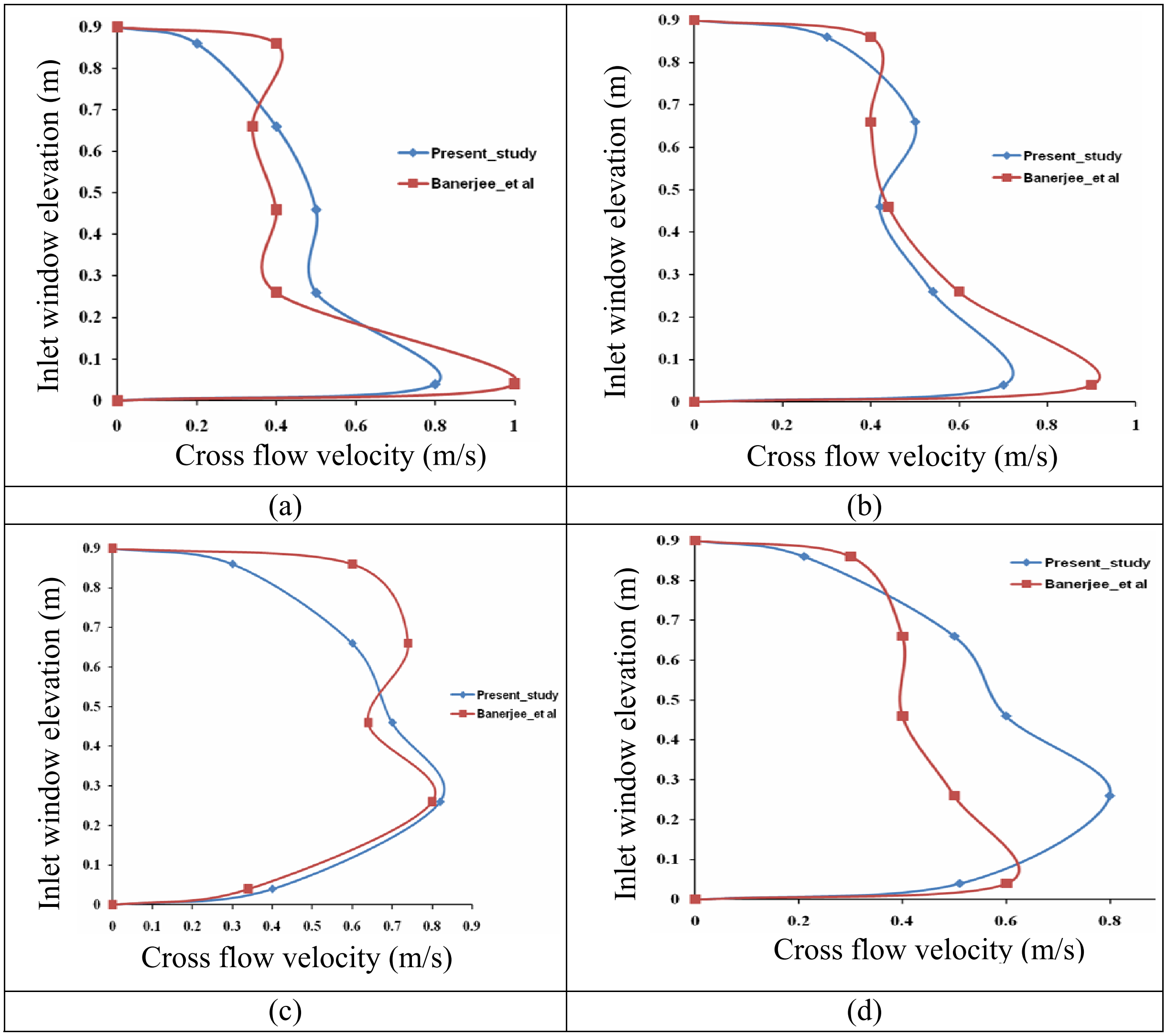

Fig. 5.3: Cross flow velocity distribution along IHX inlet window at various reference locations: (a) 0°, (b) 90°, (c) 180° and (d) 270°.

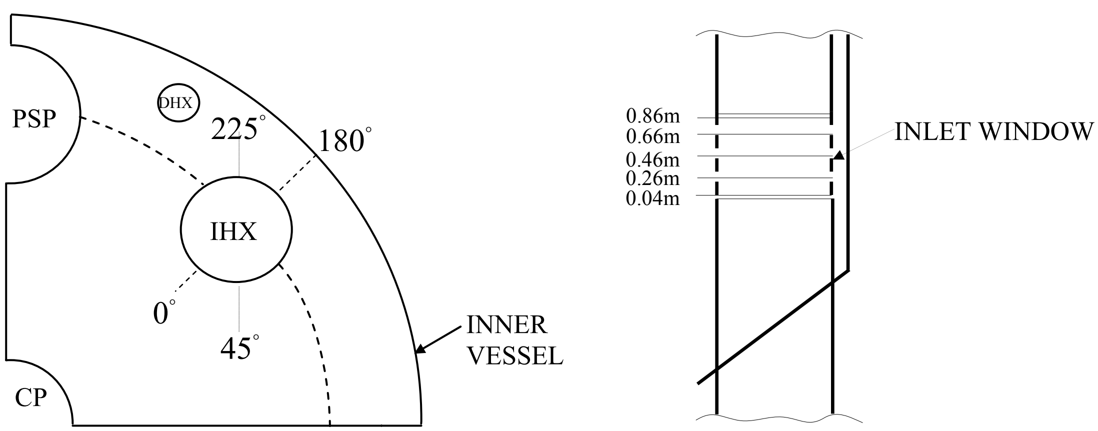

Fig. 5.4: Measurement locations around IHX inlet window and side view indicate the height along IHX inlet window.

5.5. SODIUM FLOW DISTRIBUTION IN PFBR HOT POOL

Following the validation studies, further CFD simulations on the sodium pool have been performed. The predicted velocity distribution in a vertical section passing through the IHX and the free surface velocity distribution are depicted in Fig. 5.5.

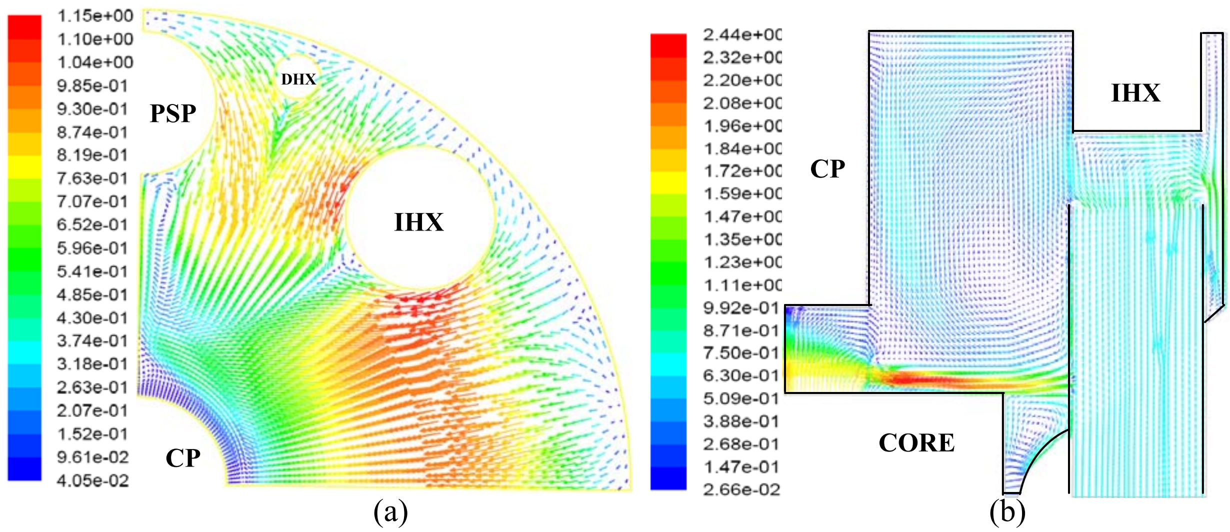

Fig. 5.5: Sodium velocity in PFBR hot pool (m/s): (a) at the free surface and (b) at a section through IHX.

In the original hot pool, fluid emanating from the core, encounters a high resistance porous skirt which in turn enables radial movement of the fluid. Such a design has the advantage of avoiding thermal stratification in the lower part of hot pool. The maximum velocity of liquid sodium entering the hot pool is about 2.4 m/s and it is seen that, the circumferential variation in this component of velocity is negligible. When this radial jet reaches close to the upper portion of the inner vessel, it turns upwards and accelerates. Upon reaching the free surface, the flow turns radially inwards towards the control plug. Since it meets the flow radially coming out from the control plug, the two opposing streams form a recirculation zone around the primary sodium pump. The fluid eventually leaves the hot pool with a free surface velocity of 1.15 m/s. The corresponding value of Fr^* is 6.95. This is much higher than the permissible value of Fr^* to avoid gas entrainment, which is determined to be 2.0.

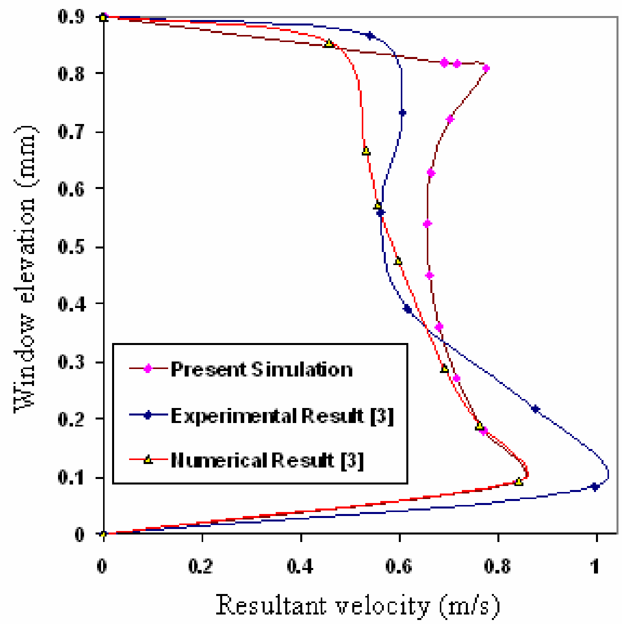

Fig. 5.6: Vertical distribution of resultant velocity along IHX inlet window at an angle of 225°.

The predicted velocity distribution at the entry to IHX, at a particular circumferential location around IHX is presented in Fig. 5.6. It can be noticed that, the comparison is satisfactory. The influence of turbulent fluctuations on the domain is parameterized by investigating the predicted turbulent kinetic energy and the eddy viscosity at the free surface as depicted in Fig. 5.7. Higher levels of turbulent kinetic energy and eddy viscosity are noticed near the pump location which is perhaps a major concern for gas entrainment.

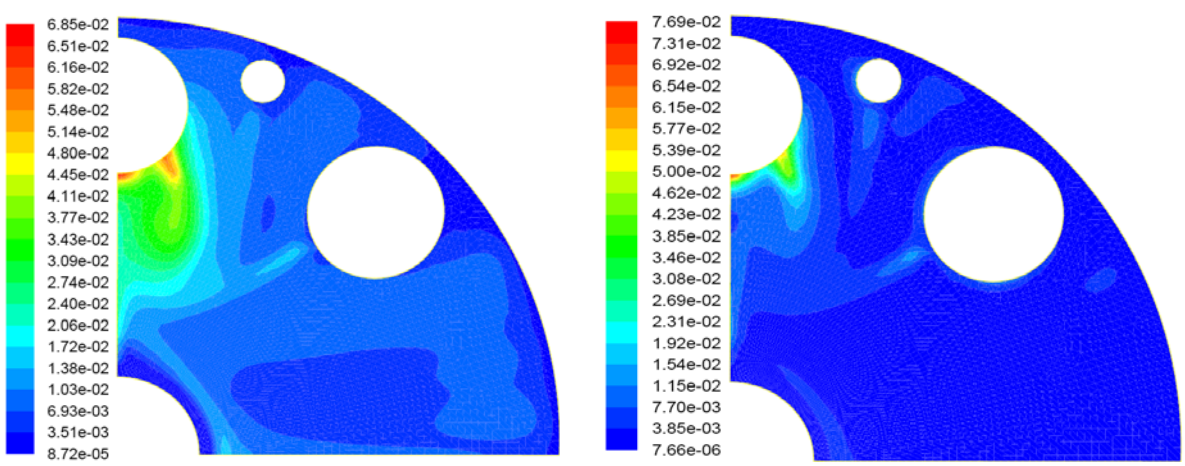

(a) (b)

Fig. 5.7: (a) Turbulence kinetic energy (m^2/s^2) and (b) eddy viscosity ($N\text{-}s/m^2$) at the free surface of PFBR hot pool.

5.6. MITIGATION STRATEGY FOR GAS ENTRAINMENT

In the previous section, it was noticed that, the reference design is prone to risk of gas entrainment. To mitigate this, it is essential that the free surface velocity be reduced, without affecting the compactness of the reactor. One of the simplest measures is to provide a horizontal baffle of appropriate width welded to the upper shell of inner vessel to suppress the vertical jet swelling upwards and close to the wall. From the stability point of view and to minimize plate interference with fuel handling systems, the plate width has to be optimum. Hence, a systematic investigation to obtain the appropriate baffle width and the right depth of submergence from sodium free surface has been carried out. The suitability of locating the baffle plate has been studied for the following cases.

- At the free surface
- 0.5 m below the free surface and
- 1.3 m below the free surface

Further, different baffle widths have been investigated. Effect of placing the baffle at 3 different depths is shown in Fig. 5.8. The velocity distribution at the free surface and at a vertical plane through IHX is shown in Fig. 5.8(a-c). These plots indicate that the baffle diverts the upward axial flow towards the centre of the hot pool with a longer resistance path and thus reduces the magnitude of free surface velocity. However, among the three elevations, the plate located at a depth of 1.3 m below sodium surface resulted in a minimum free surface velocity of 0.622 m/s. The corresponding Fr^* value is 3.84. However, this value is higher than the design limit of $Fr^* = 2$, that was suggested in Section 4.2. It is also seen that the horizontal baffle does not significantly influence the flow distribution in the pool below the baffle plate elevation. Hence, the possibility of increasing the width of the plate is explored. To this end, eight different baffle widths have been systematically studied at a depth of 1.3 m below the free surface.

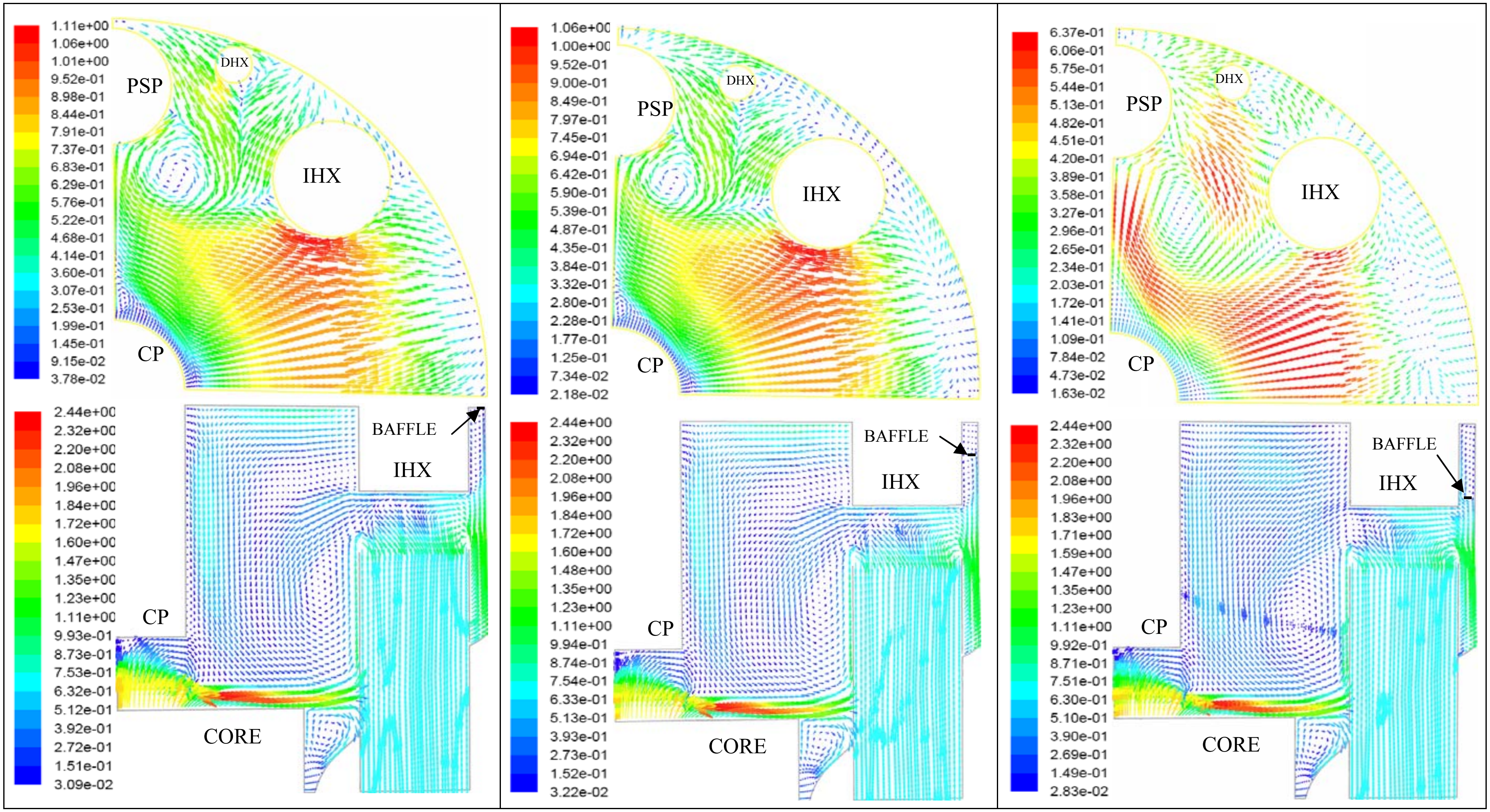

(a) (b) (c)

Fig. 5.8: Hot pool velocity field with 125 mm baffle positioned at different depths from the free surface: (a) at free surface (b) at a depth of 0.5 m from free surface and (c) at 1.3 m depth from the free surface.

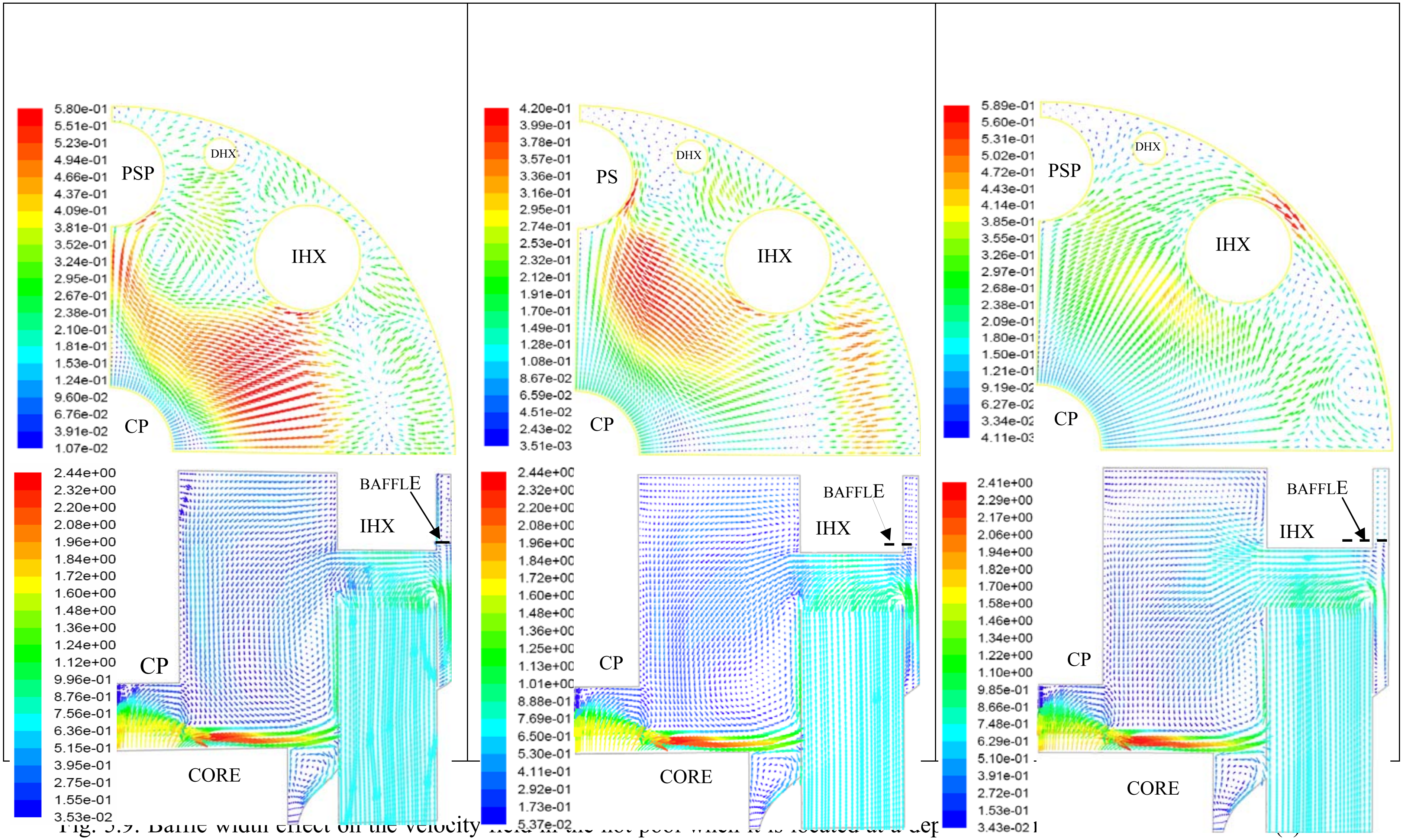

Fig. 5.9: Baffle width effect on the velocity ... ep
mm baffle (b) 500 mm and (c) 750 mm baffle.

The free surface velocity field for three different baffle widths is depicted in Fig. 5.9. The free surface velocity in these three cases is less than that observed in the reference design (without any baffle, Fig. 5.5) thus demonstrating the usefulness of the baffle. The peak value of free surface velocity as a function of baffle width that was located at 1.3 m below the free surface is depicted in Fig. 5.10. The presence of a minimum can be noticed from Fig. 5.10.

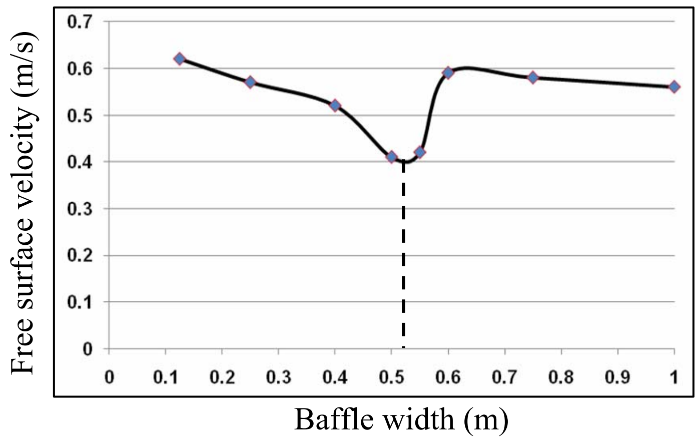

Fig. 5.10: Effect of free surface velocity against baffle width depicts possible optimal (as shown dotted lines) width for the configuration under investigation.

It is found that the magnitude of free surface velocity gradually decreases and attains an optimum value of 0.41 m/s for a baffle width of 0.5 m. The values of turbulent kinetic energy and eddy viscosity for 0.5 m baffle width located at a depth 1.3 m from the free surface are shown in Fig. 5.11.

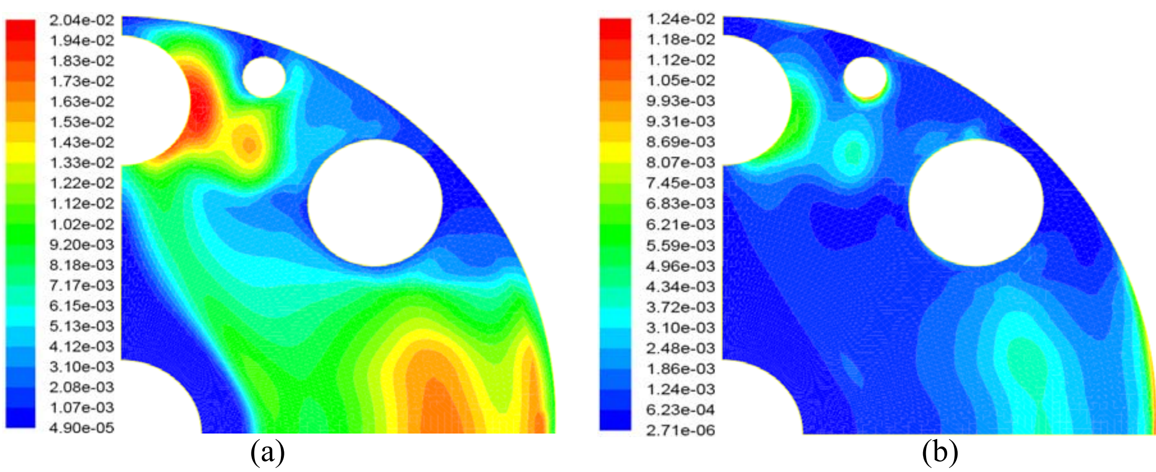

Fig.5.11: (a) Turbulence kinetic energy (m^2/s^2) and (b) eddy viscosity ($N\text{-}s/m^2$) for 0.5 m baffle width located at a depth 1.3 m from the free surface.

The peak values of turbulent kinetic energy and eddy viscosity are seen to be reduced by a factor of over 4 as compared to the value in the absence of baffle. Such a decrement reflects a lower level of activity from the fluctuating components. This agrees well with the reported results of Patwardhan et al. [88]. Any further increase in baffle width, is only counterproductive to the goal of surface velocity minimization. The value of Fr^* corresponding to a baffle width of 0.5 m is about 2.03. This is perhaps acceptable to avoid gas entrainment, as it is closer to the suggested design value of $Fr^* = 2.0$. Detailed parametric studies on baffle width carried out for 3-D CFD model of hot pool are listed in Table-5.1.

Table–5.1: Effect of baffle width on free surface velocity at different depths.

Sl. no	**Baffle width (m)**	**depth of location for the baffle from free surface (m)**	**Free surface velocity (m/s)**
1	0.125	0.0	1.08
		0.5	1.03
		1.3	0.62
2	0.25	0.0	0.97
		0.5	0.94
		1.3	0.57
3	0.4	0.0	0.92
		0.5	0.81
		1.3	0.52
4	0.5	0.0	1.07
		0.5	0.78
		1.3	0.41
5	0.55	0.0	1.07
		0.5	0.72
		1.3	0.42
6	0.6	0.0	1.04
		0.5	0.69
		1.3	0.59
7	0.75	0.0	1.12
		0.5	0.6
		1.3	0.58
8	1.0	0.0	1.15
		0.5	0.66
		1.3	0.56

It is observed that, out of three possible baffle locations, velocity magnitude has a lower value for baffle located at a depth of 1.3 m from the free surface in all cases. Also out of several possible reference design of baffle width, 0.5 m baffle width located at a depth of 1.3 m from the free surface is the best option to mitigate gas entrainment in the hot pool of PFBR.

5.7. CLOSURE

CFD studies have been carried out on PFBR hot pool and the highest free surface velocity has been estimated to be about 1.15 m/s which is conducive to argon gas entrainment into sodium pool. Mitigation of gas entrainment necessitates reduction in this free surface velocity. Towards achieving this value, a horizontal baffle plate has been proposed as a passive solution. A systematic study of baffle depth and width was conducted and an optimal configuration was reached. A baffle of 0.5 m width at a depth of 1.3 m from the free surface was found to be optimal to mitigate gas entrainment effects in the liquid pool. For this configuration, free surface velocity was found to be 0.41 m/s and its corresponding Fr^* as 2.03. The CFD results are validated against water model tests.

CHAPTER 6

FLOW PAST A FINITE SIZED CIRCULAR CYLINDER MOUNTED ON A FLAT PLATE

6.0. FOREWORD

Detailed knowledge of flow past circular cylinders is needed to understand the hydrodynamics of pool type fast breeder reactor systems as it consists of many cylindrical components, such as heat exchangers, pumps, core monitoring instruments etc., partially submerged in liquid sodium and partially exposed to argon gas maintained above the sodium pool. Horizontal sodium flow at the free surface past these components leads to the formation of von Kármán vortices [89]. These vortices form dimples of argon cover gas, which is a source of gas entrainment with the associated reactivity perturbations in the core [3]. The components are of different diameters and the depth of sodium in hot pool varies during the reactor operating cycle. Typically, the ratio of pool depth to component diameter (aspect ratio) is in the range of 2 to 10. Detailed knowledge of vortex shedding behavior exhibited by finite depth cylindrical structures is essential for understanding gas entrainment under vortex activation. However, it should be noted that the reactor pool bed is not flat but with an incline. Therefore, it is highly desirable to investigate if an accelerated bottom is strongly responsible for high free surface velocities. The motivation for these studies is to estimate the height above the pool bed wherein the effect of bed friction is important. This knowledge would provide an idea of the optimized liquid depth that has to be modeled in turbulent vortex shedding simulations with free surface effects.

Flow past a circular cylinder has been an important topic in fluid dynamics for a long time because of its wide applications in engineering and its abundant flow physics including separation, reattachment, vortex shedding etc. Flow over a flat plate results in pure boundary layer formation without encountering any flow separation. When the circular cylinder is mounted on a flat plate, wake-boundary layer interaction is imminent. The interaction between the downward flow and the boundary layer close to the surface results in the formation of a vortex system. Downstream of the flow, the two ends of the vortex system wrap around the cylinder in the shape of hairpin and hence popularly known as the horseshoe vortex. This vortex is responsible for the scouring process at the base [90].

The main aim of this chapter is to identify the finite size effect for various liquid depths on the free surface that results in vortex shedding from a circular cylinder mounted on a flat and an accelerated bottom plate in order to understand gas entrainment under vortex activation in a fast breeder reactor. To begin with a basic overview of the flow around a circular cylinder and the flow characteristics such as the Strouhal number, vortex shedding, drag, lift, and pressure coefficients are introduced. Detailed 2-D validation of flow around a circular cylinder at low Reynolds number of the order of 100 – 200, against other available experimental, numerical simulations is presented.

6.1. OVERVIEW OF FLOW AROUND A CIRCULAR CYLINDER

Flow around a circular cylinder tends to follow the shape of the body provided the flow velocity is very small, known as creeping flow. Flow at the inner part of the boundary layers, travels more slowly than the flow near to the free stream. As the speed of the flow increases, separation of flow occurs at some point along the body due to the occurrence of the adverse pressure gradient region (section 6.1.3). Flow separation tends to roll up the flow into swirling eddies, resulting in alternate shedding of vortices in the wake region, known as the von Kármán vortex street.

Flow characteristics around a circular cylinder vary with the Reynolds number. Reynolds number of the flow around a circular cylinder is represented by,

$$\mathrm{Re} = \frac{uD}{v} \tag{6.1}$$

where D is the cylinder diameter, u is the inlet velocity, and v is the kinematic viscosity of the flow. Experimental study of the flow around a circular cylinder has identified regimes where significant changes in flow patterns occur as the Reynolds number changes. Generally, the following regimes have been identified from Roshko's experiment [91]:

Stable range	$40 < \mathrm{Re} < 150$
Transition range	$150 < \mathrm{Re} < 300$
Irregular range	$300 < \mathrm{Re} < 2\times10^5$

Flow becomes very irregular with instabilities beyond Reynolds number of 2×10^5. Another dominant feature of the flow around a circular cylinder is the three-dimensional nature of the flow. Bloor [92] investigated the flow around a circular cylinder between Reynolds number of 200 to 400 when turbulent motion starts to develop in the wake region of the flow. She observed that the flow transition in the wake region is triggered by large-scale three-dimensional structures. Williamson [93] documented the development of three-dimensional flow structures as depicted in Fig. 6.1.

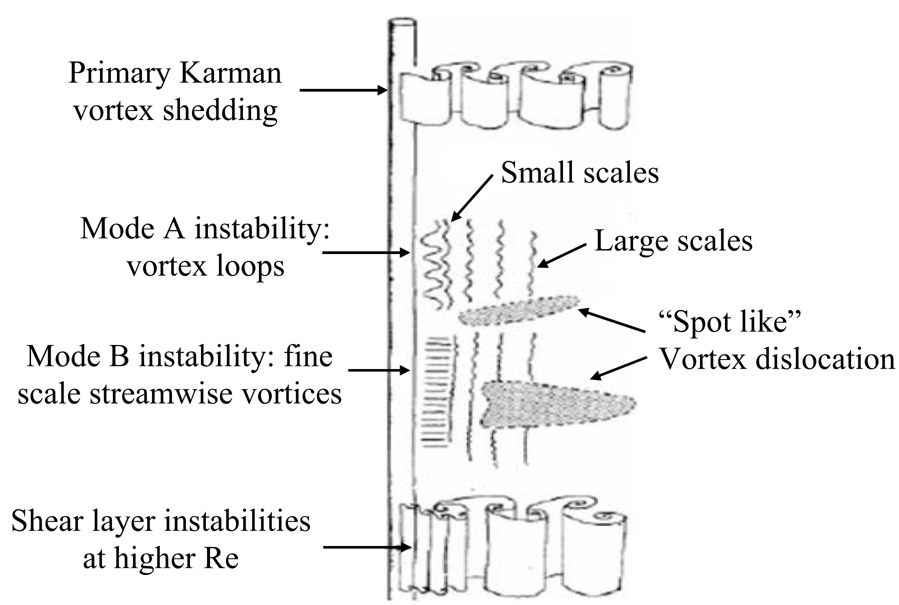

Fig. 6.1: Development of three dimensional flows in the wake region [93].

Primary Kármán vortex is first observed at low Reynolds number (50 < Re < 1200). With increase in Reynolds number, small scale stream wise vortex structures start to form followed by formation of larger 3-D vortices resulting from vortex dislocations. Towards the bottom, shear layer instabilities of the flow is noticed at higher Reynolds number.

6.1.1. Vortex Shedding and Strouhal Number

The separation of flow around a circular cylinder causes pairs of eddies on the top and bottom parts of the cylinder that travel in the wake region resulting in alternate shedding as shown in Fig. 6.2.

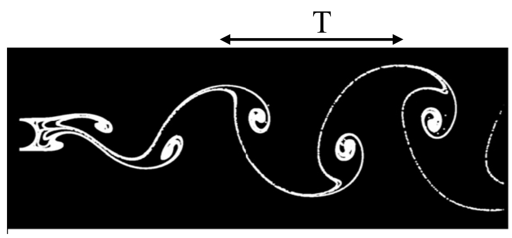

Fig. 6.2: Experimental visual of flow past a circular cylinder [94] at Re = 140, (T = time period).

The frequency of vortex shedding is determined through a non-dimensional parameter known as Strouhal number (St) and is defined by;

$$St = \frac{fD}{u} \tag{6.2}$$

where f is the vortex shedding frequency equal to 1/T (Fig. 6.2)

6.1.2. Drag and Lift Coefficients

Roshko [91] pointed out that the Strouhal number is related to drag coefficient of the flow. In sub-critical Reynolds number region ($100 < Re < 10^4$), increase in the Strouhal number is generally accompanied by a decrease of the drag coefficient which is defined by:

$$C_D = \frac{F}{\frac{1}{2}\rho A u^2} \tag{6.3}$$

where A is the projected area in the flow direction and F is the sum of the pressure and viscous force components on the cylinder surface acting in the flow direction. Lift coefficient is calculated considering the vertical force acting on the cylinder surface (Fig. 6.3).

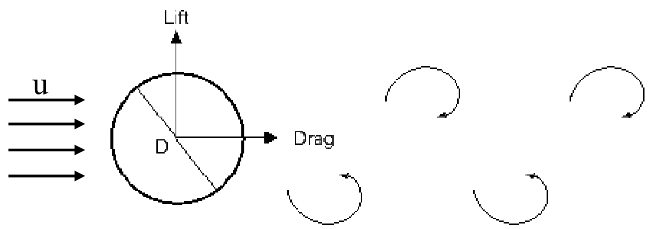

Fig. 6.3: Lift coefficient acting on a cylinder.

The variation of the drag coefficient with Reynolds number around a circular cylinder is depicted in Fig. 6.4.

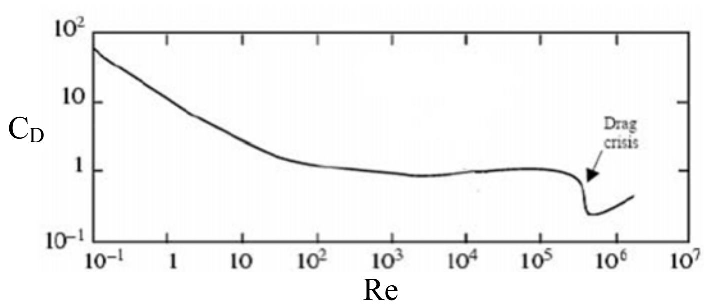

Fig. 6.4: Drag coefficient of the flow around a circular cylinder [95].

At higher Reynolds number of about 2×10^5, the drag decreases dramatically due to transition to turbulence near the cylinder wall. Turbulent nature of the boundary layer involves mixing of flow which results in a higher velocity gradient as compared to laminar flow. Consequently, this delays the separation of flow and pushes the separation point to the rear of the cylinder resulting in a narrower wake, which is accompanied by a drop in the drag coefficient. This is known as the '*drag crises*'. When a vortex is shed from the top of the cylinder, a suction area is created and the cylinder experiences lift. Half a cycle later, an alternate vortex is created at the bottom part of the cylinder. Throughout the process, the lift force changes alternately in a complete cycle of vortex shedding but the cylinder experiences drag constantly changing at twice the frequency of the lift.

6.1.3. Pressure Coefficient

Apart from the drag and lift coefficients, the pressure coefficient distribution around the surface of the cylinder is important. Near the surface of the cylinder, flow momentum is quite low due to viscous effects and thus is sensitive to the changes of pressure gradient. Figure 6.5 shows a typical pressure distribution around a circular cylinder.

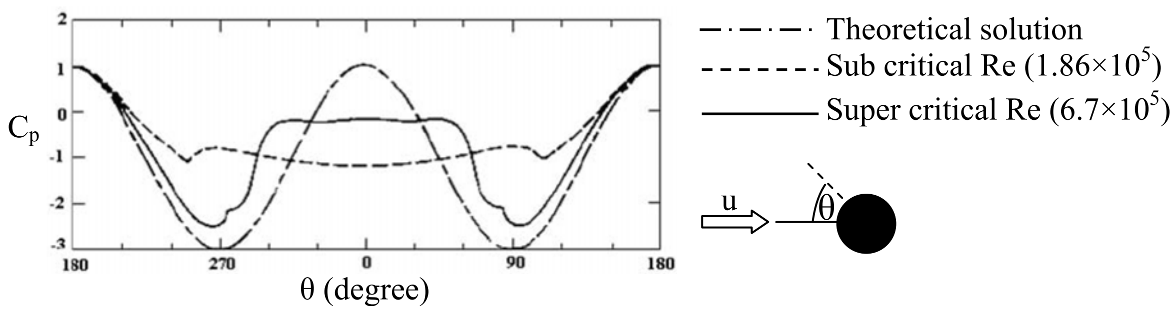

Fig. 6.5: Measured pressure coefficient distribution on the cylinder surface [95].

At $\theta = 0$, velocity becomes stagnant and pressure coefficient is maximum as dynamic head is completely converted to static pressure head (Bernoulli's Theorem). The flow speed then starts to increase accompanied by a negative pressure coefficient. In this case, decrease of pressure in the direction of flow assists the fluid movement and there is no retardation of flow. The speed of flow then starts to reduce near $\theta = 80°$, accompanied by an increase of pressure in the direction of the flow, which results in the adverse pressure gradient situation. The flow now has to move against the pressure force in addition to the viscous force. This leads to a reduced gradient of the velocity profile and the wall shear stress. Separation of flow occurs when the shear stress cannot overcome the adverse pressure gradient (usually happens at $80° < \theta < 120°$ for sub-critical flow). Beyond the point of separation, average pressure remains fairly constant in the wake region.

6.2. SIMULATION OF FLOW PAST A CIRCULAR CYLINDER AT LOW REYNOLDS NUMBER

For a finite circular cylinder (FC), aspect ratio refers to the ratio of its axial height (H) to its diameter (D). Effect of free end on the near wake dynamics in cross flow is of practical interest. This aspect has been experimentally investigated by a number of authors (see, Refs. [96-100]). Park and Lee [96] observed that, vortex shedding frequency decreases for smaller aspect ratios, albeit with an attendant elongation in vortex formation length. This three dimensionality aspect has been attributed to non-uniformities that exist along the body span, in particular, to the imposed end constraints. These investigations were conducted at Re = 2×10^4. Slaouti and Gerrard [97] have investigated the effect of end conditions on the wake structures. Eisenlohr and Eckelmann [98] have achieved parallel shedding mode by modifying the end conditions. Moving end plates have been used by Szepessy and Bearman [99] to investigate the effect of finite aspect ratio. They have measured fluctuating forces, shedding frequency and spanwise correlation by varying end plate separation and Reynolds number. The aspect ratio (H/D = 0.25 - 12) was found to have the most striking effects on the fluctuating lift force. The investigations by Norberg [100] covers the subcritical Reynolds number range of 50 to 4×10^4, for aspect ratios smaller than 7. In the intermediate range of subcritical Reynolds number ($\approx 2\times10^3$), he identified a bi-stable flow switching between *regular vortex shedding* and *irregular flow*. In their influential experiments, Okamoto and Sunabashiri [101] have noticed the process of shedding changes from symmetric to anti-symmetric vortices, with corresponding changes in surface pressure distribution. The turbulent wake characteristics were investigated in the subcritical Reynolds number range of 2.5×10^4 to 4.7×10^5. Fröhlich and Rodi [102] have employed large eddy simulations at Re = 4.3×10^4 and for an aspect ratio of 2.5. They have presented detailed interaction effects between flow separation from side walls and the roof the circular cylinder.

Bed friction plays a critical role in controlling the wake-boundary layer interaction. Balachandar et al. [103] have quantified these effects and observed that, its influence is more pronounced in shallow flows compared to deep flows. The wake region of a bluff body is quite distinct in deep flows with Kármán vortex street formation, while in a corresponding shallow flow, it was found to be stabilized due to frictional influences and the vortex shedding is found to be annihilated. Chu et al. [104] have theoretically studied the stability of shear flows in shallow open channels. They have used order of magnitude arguments and proposed a bed friction parameter as a relative measure to indicate between stabilizing effects of bed friction and destabilizing effect of transverse shear. Particle image velocimetry (PIV) has been employed by Akilli and Rockwell [105] to investigate flow past a vertical cylinder in shallow water in the depth range of 0.5 to 2.0, for $Re \approx 10^4$. Based on their experiments, vorticity and Reynolds stresses above the bed were characterized, with distinct features compared to that of two dimensional wakes behind an infinitely long cylinder.

The formation of unsteady laminar necklace vortex system at the junction between the rectangular bluff body and the flat plate was studied experimentally by Seal et al. [106]. They have found that the vortex system exhibits unsteady behavior which is characterized by periodic formation of necklace vortices upstream of the body that subsequently breaks away and advects in the downstream wake region. The review on junction flows by Simpson [107] covers physical insights of some practical aspects of flows around blunt and streamlined obstacles. For low Reynolds number laminar flows, three primary horseshoe vortices are formed on the upstream of the junction. Baker [108] investigated the horseshoe vortex formation around the base of a cylinder by a separating laminar boundary layer. Pressure distribution underneath the vortex system has been measured and the variation of the horseshoe vortex position on the plane of symmetry upstream of the cylinder has been determined. A general schematic of flow topology of vortex structures past a finite sized circular cylinder is depicted in Fig. 6.6.

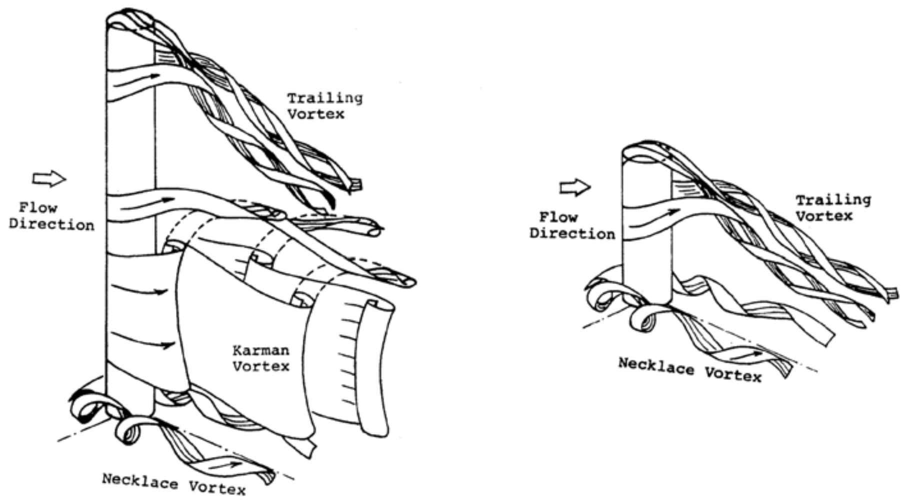

Fig. 6.6: Flow past a pillar, depicting finite size effects (from Kawamura et al. [109]). In the junction between wake and boundary layer, a necklace vortex is formed. This vortex system interacts with the trailing edge vortices for shorter heights.

Here, a horseshoe vortex system is formed at the junction that forms the wake-boundary layer interaction region. The interaction between the trailing edge vortices and necklace vortices is prominently seen for the shorter cylinder. However, in the present study, the cylinder is modeled to be taller than the flow domain of interest and hence, devoid of any trailing edge effects.

6.2.1. Governing Equations

The fluid flow past a circular cylinder in three dimensions is governed by the time-dependent incompressible form of Navier-Stokes and continuity equations. The governing equations have already been discussed in chapter 3.

6.2.2. Initial and Boundary Conditions

The boundary conditions for two-dimensional simulations are:

(a) Inlet located at a distance of 4D on the upstream of the cylinder, is imposed with a uniform velocity U_∞

(b) Outlet located at a distance of 14D downstream of the cylinder with zero traction is specified with a constant pressure

(c) No-slip boundary condition on the cylinder wall, and

(d) No-slip condition on the side confining channel walls located at 4D away from the centre of the cylinder.

The flow domain of interest with boundary conditions is depicted in Fig. 6.7.

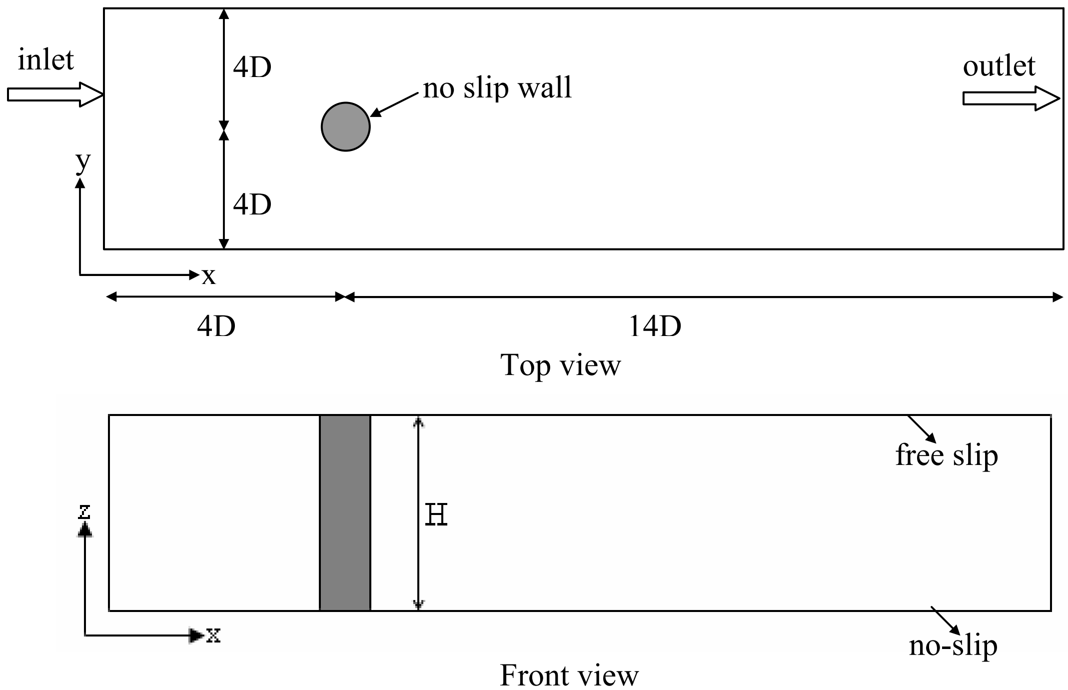

Fig. 6.7: Flow domain of interest with boundary conditions.

Since the side walls are located generally close to the cylinder, there is a concern on the possibility of numerical blockage. This was found to be negligible by systematically varying the sidewall position. However, for the three dimensional simulations, additional boundary conditions are needed for the top and bottom walls. To simulate realistic shallow liquid flows, the bottom wall is imposed with a no-slip boundary, while a free slip condition is enforced on the top surface. To enable comparison with other 2-D simulations and to eliminate undesirable span wise effects into the simulations, free-slip condition on both top and bottom walls is also investigated. Although a free slip bottom wall is unphysical, it helps in understanding unconfined flow past a high aspect ratio circular cylinder. Initial condition for the stream-wise velocity component (u) is assigned with the free stream velocity (U_∞), while other two components are set as 'zero'.

6.2.3. Numerical Approach

The governing equations are solved by a finite volume method using a general purpose CFD tool [53]. Pressure-velocity coupling between the incompressible Navier-Stokes and continuity equations is established using the Pressure Implicit with Splitting of Operators (PISO) algorithm (Versteeg and Malalasekara [52]). The first order semi- implicit scheme is chosen for the time integration. In the PISO solver, the pressure term is treated implicitly at $(n+1)^{th}$ time level, while all other terms are treated explicitly at $(n)^{th}$ time level as follows:

$$u^{n+1} = u^n - \frac{\Delta t}{\rho}\left[\frac{\partial p}{\partial x_i}\right]^{n+1} \tag{6.4}$$

Since it is not possible to compute both velocity and pressure simultaneously at $(n+1)^{th}$ time level, the above equations are split into one that computes an intermediate pressure (p^*), and an intermediate velocity (u_i^*) as follows:

$$u_i^* = u_i^n - \frac{\Delta t}{\rho}\left\{u_j \frac{\partial u_i}{\partial x_j}\right\}^n - \frac{\Delta t}{\rho}\left(\frac{\partial p^*}{\partial x_i}\right) \tag{6.5}$$

However, we need to project these intermediate velocities (which do not satisfy mass conservation) into a divergence free vector space. Subtraction of Eq. (6.5) from Eq. (6.4) provides

$$u_i^{n+1} - u_i^* = -\frac{\Delta t}{\rho}\left\{\frac{\partial^2 p^{n+1}}{\partial x_i \partial x_i} - \frac{\partial p^*}{\partial x_i}\right\} \tag{6.6}$$

Applying divergence on both sides of Eq. (6.6) and enforcing mass conservation $\left(\left(\partial u_i^{n+1}\right)/\partial x_i = 0\right)$ leads to the following Poisson equation

$$\nabla^2 \left(p^{n+1} - p^* \right) = -\frac{\rho}{\Delta t} \frac{\partial u_i^*}{\partial x_i} \tag{6.7}$$

It should be noted that, the intermediate value of pressure (p^*) can be evolved through an initial guess pressure. Further details related to the flow solver and spatial and discretization scheme are available in detail from references [52] and [79]. The discrete temporal step Δt is determined by the CFL (Courant–Friedrichs–Lewy) criterion [81]. An absolute error (ε) in the discretized momentum and continuity equations is set using a tolerance criterion < 10^{-4}.

6.3. RESULTS AND DISCUSSION

6.3.1. Simulation of Flow past a Circular Cylinder

Simulating the fluid flow features past a circular cylinder forms a good test case for the spatio-temporal discretization scheme employed by the Navier-Stokes solver. In an unconfined flow past a circular cylinder, ideally the domain boundary on the upstream and downstream should be located at infinity. However, in a numerical investigation, the computational resources need to be optimized vis-à-vis the resolved scales associated with the simulation. It is also important that the presence of the imposed boundary conditions does not pollute with any undesirable numerical effects. To this end, approximately 4D on the upstream and 14D on the downstream have been chosen for the domain size selection, in accordance with Bosch and Rodi [110].

6.3.2. Grid Sensitivity Check

In a CFD simulation, establishing the independent nature of the solution on the grid size used in the calculations is an essential first step. Towards this goal, an attempt is made to determine optimum mesh for three dimensional simulations. It is observed that the number of radial grid divisions on the periphery of the cylinder is a useful parameter to determine the mesh for an accurate prediction of drag and lift forces. Grid sensitivity tests were carried out first for the case of Re = 200, with four different mesh sizes. Under two dimensional settings, the flow domain of interest is tessellated with a non-homogeneous grid as shown in the Fig. 6.8(a). A close–up view of the mesh, shown in Fig. 6.8(b), reflects fine mesh closer to the no-slip surfaces.

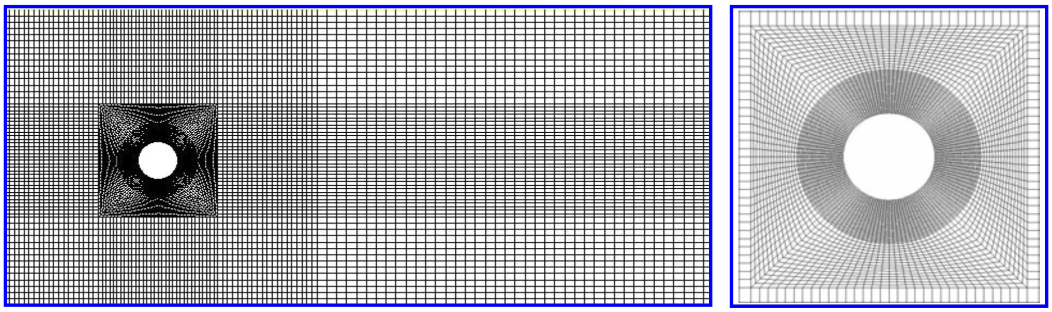

(a) (b)

Fig. 6.8: Typical global grid pattern around the cylinder adopted for numerical simulation: (a) a view of the top surface and (b) close-up view that depicts an O-type grid around the periphery of the cylinder.

Different mesh sizes employed for the grid sensitivity study are shown in Table-6.1. Here, the force coefficients (C_D and C_L), Strouhal number (St) and CPU time requirements associated with grid sizes are presented. It can be noticed that the difference between the results obtained with mesh M3 and M4 is very small, thus justifying the use of the M3 mesh for further investigations.

Table-6.1: Grid sensitivity study for Re=200.

Mesh	**No. of control volumes**	**Min. Radial grid spacing**	C_D	C_L	**St**	**CPU Time per iteration (s)**
M1	7744	0.063D	1.55±0.05	±0.785	0.202	4
M2	9792	0.030D	1.48±0.04	±0.71	0.200	5
M3	11840	0.016D	1.45±0.035	±0.67	0.201	7
M4	13888	0.013D	1.44±0.03	±0.68	0.202	10

Figure 6.9 shows the time histories of the drag force coefficients for all these different mesh sizes. From the figure it can be seen that the mean drag coefficient decreases with increase in the number of elements. The mean drag force values for mesh M3 and M4 are nearly the same, further justifying the M3 mesh size employed in the present study.

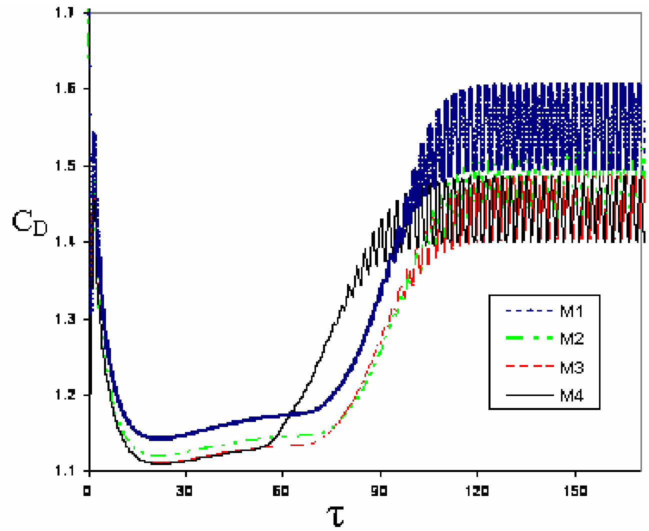

Fig. 6.9: Temporal variation of drag force coefficients to study grid sensitivity.

6.3.3. Validation of Unsteady Wake Characteristics

Spatio-temporal dynamics of the wake behind the circular cylinder is investigated using a mesh of size M3. The temporal evolution of fluid flow features are investigated by capturing its sinuous wake region. Vorticity contours at three different time levels are compared in Fig. 6.10 against the recent numerical calculations of Kalita and Ray [111].

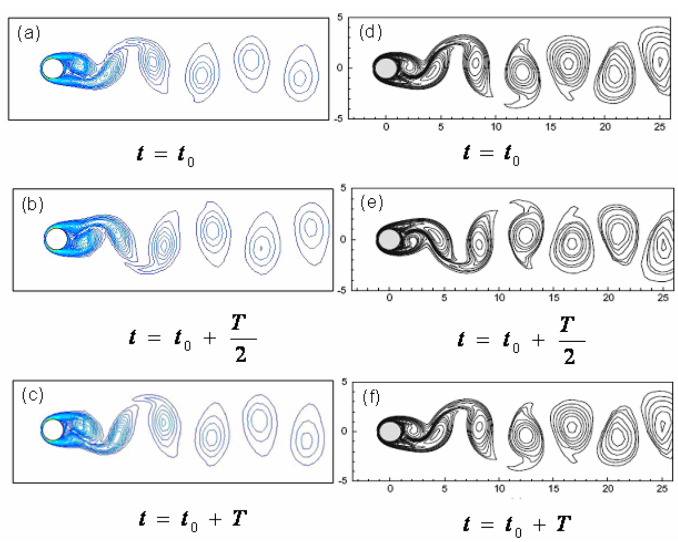

Fig. 6.10: Instantaneous vorticity contours depicting one complete shedding cycle at Re = 200 (a-c) present simulation; (d-f) (Kalita and Ray [111]).

Overall, a good comparison can be seen between these two different simulations. The predicted Strouhal number, mean drag coefficient and its lift coefficient fluctuation are compared with other published experimental and numerical investigations are presented in Table-6.2. The temporal variation of forces acting on the cylinder at Re = 200 is depicted in Fig. 6.11.

Table-6.2: Comparison of Strouhal number, drag coefficient and fluctuating lift coefficient for flow past a circular cylinder at Re = 200.

Reference	St	C_D	C_L
Kalita and Ray [111]	0.210	1.35	± 0.53
Wu and Hu [112]	0.190	1.36	± 0.56
Berthelsen and Faltinsen [113]	0.200	1.37	± 0.70
Farrant et al. [114]	0.196	1.37	± 0.71
Bai et al.[115]	0.195	1.40	± 0.74
Lecointe and Piquet [116]	0.230	1.46	±0.70
Chan and Anastasiou [117]	0.180	1.48	± 0.63
Present study	0.200	1.45	± 0.67

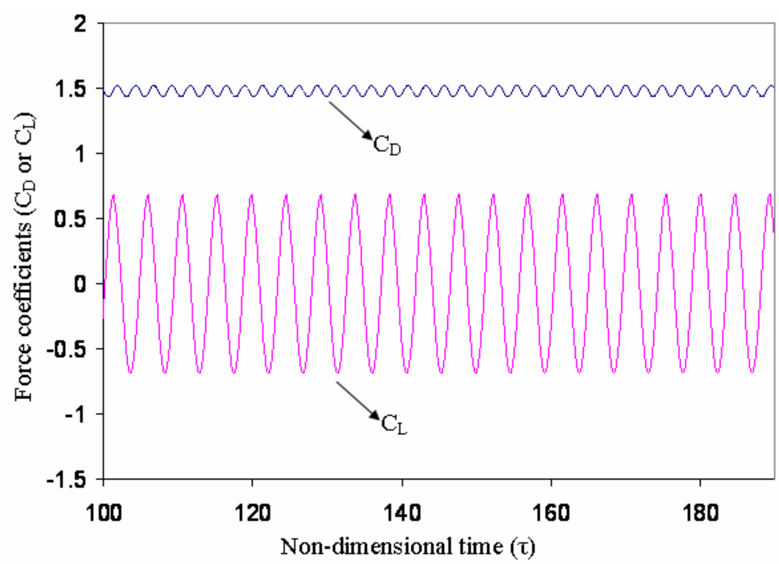

Fig. 6.11: Temporal variation of drag and lift force coefficients after an organized, steady shedding is established. The simulations are performed for Re = 200.

6.4. FINITE ASPECT RATIO EFFECTS OF FLOW PAST A CIRCULAR CYLINDER

When a circular cylinder with finite aspect ratio is mounted on a flat plate, the three-dimensionality effects come into picture. The growth of boundary-layer (δ) on the flat plate influences the vortex shedding past the cylinder leading to wake-boundary-layer interaction. The effect of normalized thickness of the boundary-layer (δ/D) can often be studied as one of the parameters that trigger the three-dimensionality in the system. There is a possibility of strong entrainment of outer irrotational fluid into the wake formation region.

6.4.1. Forces on the Circular Cylinder

To understand the dynamics of flow past a finite circular cylinder, for shallow liquid flows, five different aspect ratios, viz. H/D = 0.5, 1, 2, 5 and 10 are considered. In all the cases, the Reynolds number based on the cylinder diameter is fixed at 200. The three dimensional calculations are initiated by employing free slip walls both on the bottom plate as well as on the top surface. Once the velocity and pressure distributions in the flow domain are obtained from the Navier-Stokes solver, forces and moments on the finite circular cylinder are computed, which are the design parameters of interest. The lift and drag forces are obtained by integrating the normal and tangential stresses which are due to pressure and velocity gradients as given below:

$$C_D\left(t\right)=\int_0^H\int_0^{2\pi} p\cos\theta d\theta\, dz-\frac{2}{\mathrm{Re}}\int_0^H\int_0^{2\pi}\frac{\partial u}{\partial x}\cos\theta d\theta\, dz+\frac{1}{\mathrm{Re}}\int_0^H\int_0^{2\pi}\left(\frac{\partial u}{\partial y}+\frac{\partial v}{\partial x}\right)\sin\theta d\theta\, dz \tag{6.8}$$

$$C_L\left(t\right)=-\int_0^H\int_0^{2\pi} p\sin\theta d\theta\, dz+\frac{2}{\mathrm{Re}}\int_0^H\int_0^{2\pi}\frac{\partial v}{\partial y}\sin\theta d\theta\, dz-\frac{1}{\mathrm{Re}}\int_0^H\int_0^{2\pi}\left(\frac{\partial u}{\partial y}+\frac{\partial v}{\partial x}\right)\cos\theta d\theta\, dz \tag{6.9}$$

Here, angle θ is measured with reference to the upstream vector.

The temporal evolutions of lift forces on the cylinder are presented in Fig. 6.12, for four different values of H/D in the range of 0.5 to 10.0. To start with simulations are performed without taking bed friction into account. Gradually, steady periodic lift force fluctuations about a zero mean value are established due to unsteady wake effects on the cylinder. However, to simulate realistic conditions, bed friction was introduced through a no-slip boundary condition approximately at a non-dimensional time $\tau \approx 100$ and the transient simulations are further continued. It can be noticed that, after a few steady periodic cycles, stabilization is imparted to the wake structures due to bed friction. This result is in accordance with the experimental findings of Balachandar et al. [103] for turbulent flow over a finite cylinder. The complete absence of waviness due to unsteady wake can be particularly noticed for $H/D \leq 1.0$. Nevertheless, persistence of convective instability in the far wake region generates a negligible lift force fluctuation about a zero mean value. However, for $H/D \geq 2.0$, vortex shedding is established with a dominant Strouhal frequency for $2 \leq H/D \leq 5.0$. At $H/D = 10.0$, a beating type pattern can be noticed, indicating that the span wise correlation is dominated by two independently evolving cellular patterns. The evolution of inline drag force over the cylinder for different H/D values, viz., 0.5, 2.0, 5.0, and 10.0 is presented in Fig. 6.13. It can be observed that, small drag coefficient fluctuations exist for free slip bed. The bed friction effects are dominant as seen for $H/D = 0.5$ compared to higher H/D values. As already indicated, after von-Kármán vortex shedding is established, the free-slip boundary condition is changed to accommodate bed friction. As a result, the drag coefficient increases for $H/D = 0.5$. However, mean drag value decreases for $H/D \geq 2.0$. This implies that the aspect ratio of the finite cylinder influences the drag force. At $H/D = 10.0$, the presence of cellular vortices results in beating type of pattern in Fig. 6.13(d). This is corroborated by the presence of two closely spaced frequencies in the fast Fourier transfer (FFT's) analysis, which is presented in section 6.4.4.

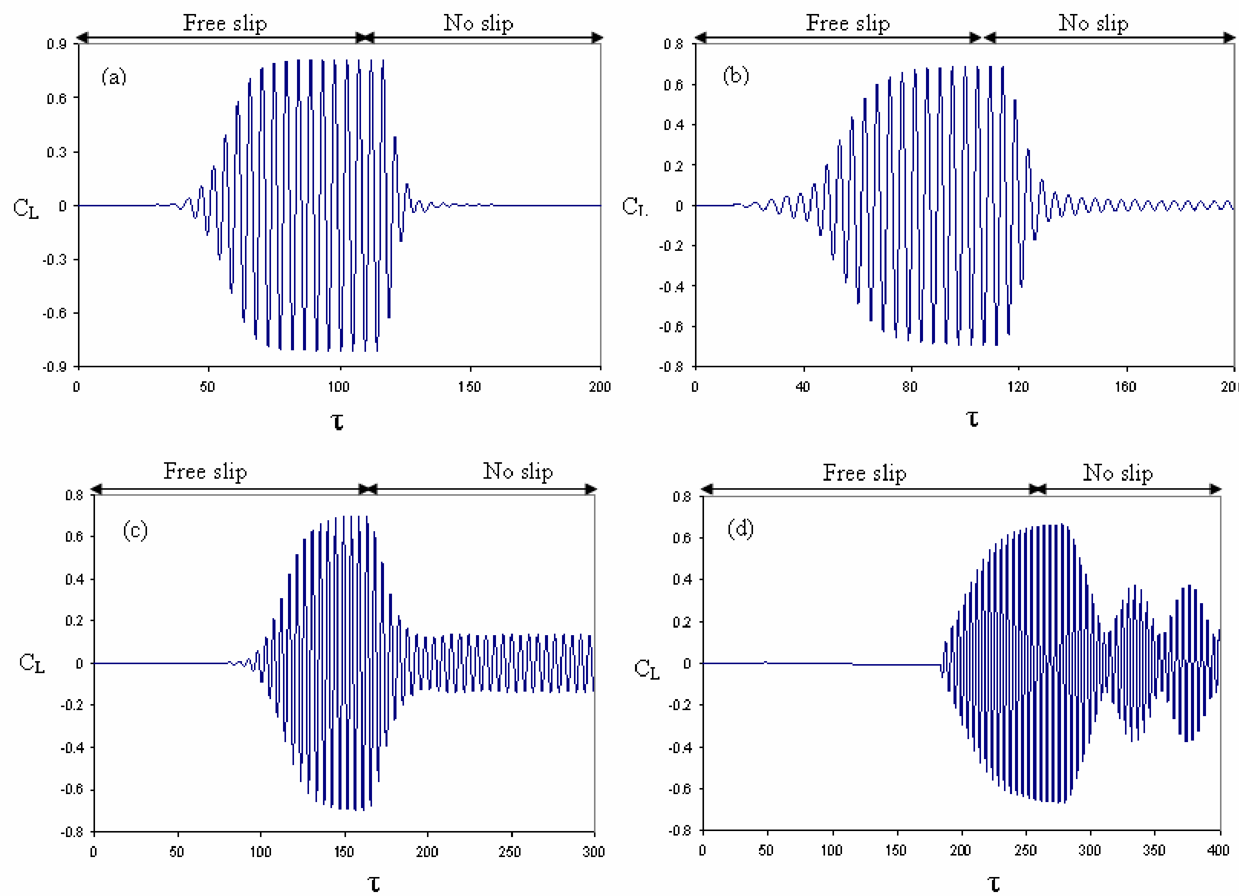

Fig. 6.12: Evolution of lift force coefficients on the cylinder for (a) H/D = 0.5, (b) H/D = 2, (c) H/D = 5 and (d) H/D = 10.

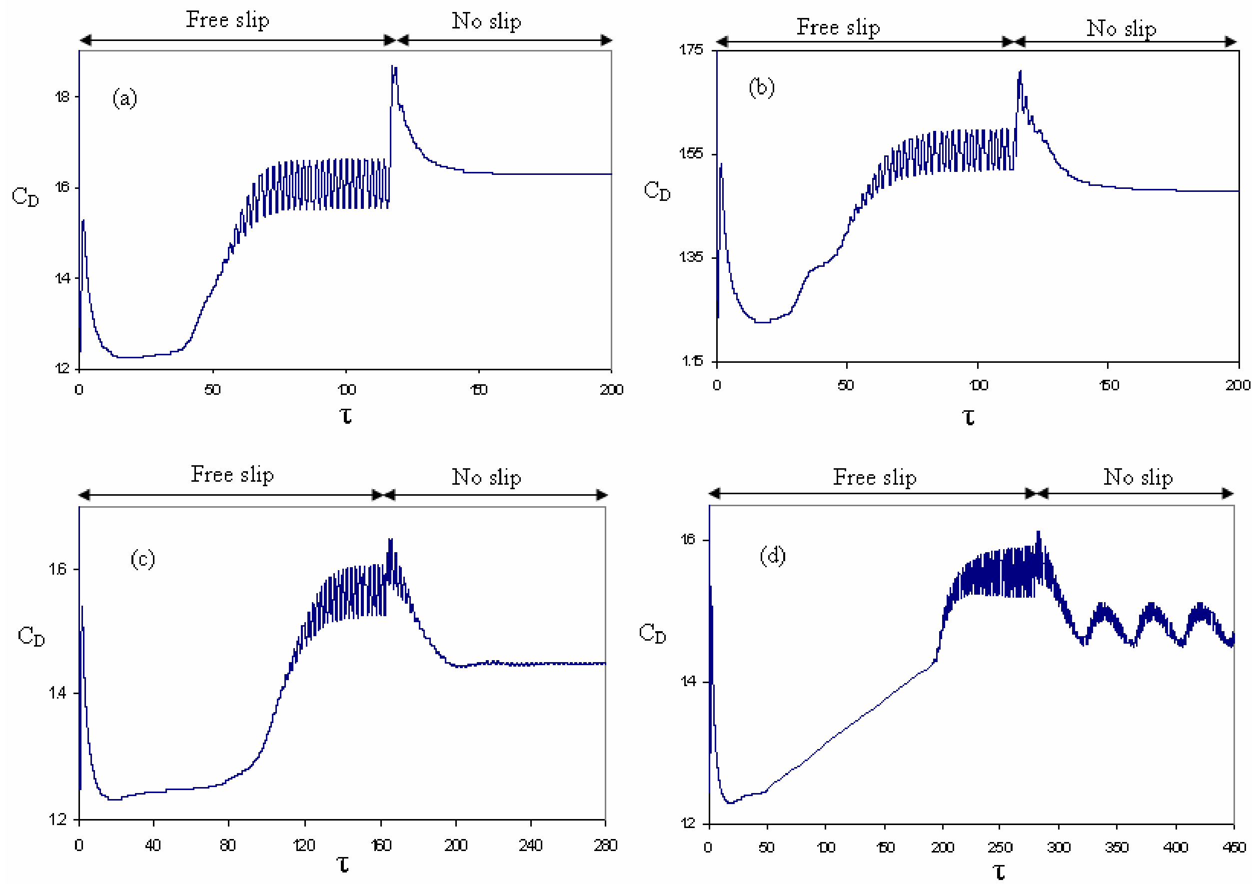

Fig. 6.13: Evolution of drag force coefficients on the cylinder for (a) H/D = 0.5, (b) H/D = 2, (c) H/D = 5 and (d) H/D = 10.

The time averaged mean pressure coefficient is presented in Fig. 6.14 for H/D = 1 and 2 for three different spanwise heights viz., z/D = 0.15, 0.35 and 0.94, where z is vertical coordinate. Closer to the flat plate-cylinder junction, the contribution from the dynamic component of pressure is much lower due to bed friction effects. This leads to fluid flow along the spanwise height of the cylinder to proceed towards the junction.

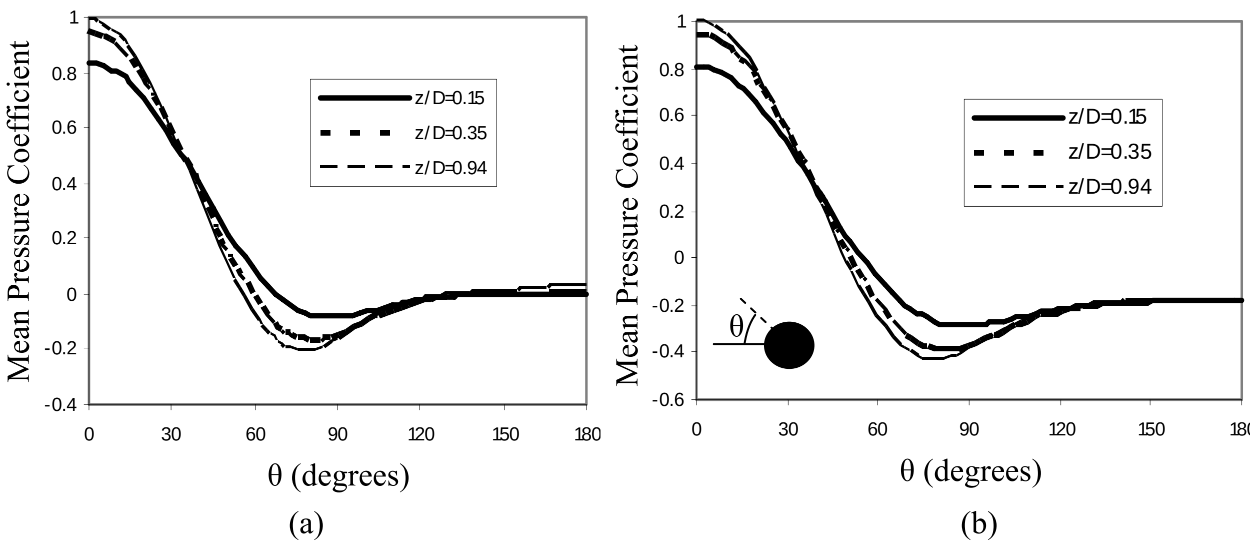

Fig. 6.14: Mean pressure coefficient at three different spanwise heights viz., z/D = 0.15, 0.35 and 0.94 for (a) H/D = 1 and (b) H/D = 2.

6.4.2. Capturing Horseshoe Vortex

Bed friction forms the necessary condition for the generation of horseshoe vortex system, at the junction between upstream of the circular cylinder and the flat plate. However, an adverse pressure gradient is needed for triggering the sufficiency condition for the flow separation to take place, which in turn would generate horse shoe vortex [118]. To be able to visualize the presence of horse shoe vortex, streakline pictures are generated to better reflect the spatio-temporal dynamics of the near wake. These are generated by solving the following evolution equations for the passive tracers, which are assumed to be inertia-less and neutrally buoyant.

$$\frac{dx_i}{dt} = u_i \quad ; \quad \frac{dy_i}{dt} = v_i \quad ; \quad \frac{dz_i}{dt} = w_i \quad ; \quad \forall i : 1, Q \qquad (6.10)$$

Here, Q refers to the total number of particles which are released from distinct sources on the fore of the finite circular cylinder. The above equations are suitably integrated from their initial positions of release on the upstream plane, as the passive scalars move along with the flow field. Note in particular, the spatio-temporal history is better embedded in these streakline visuals with distinct features such as, gradual eddy roll-up at crests and troughs. The formation of horseshoe vortex around the cylindrical structure reflected in the streakline plots is shown in Figs. 6.15 for H/D = 1 and 2 respectively.

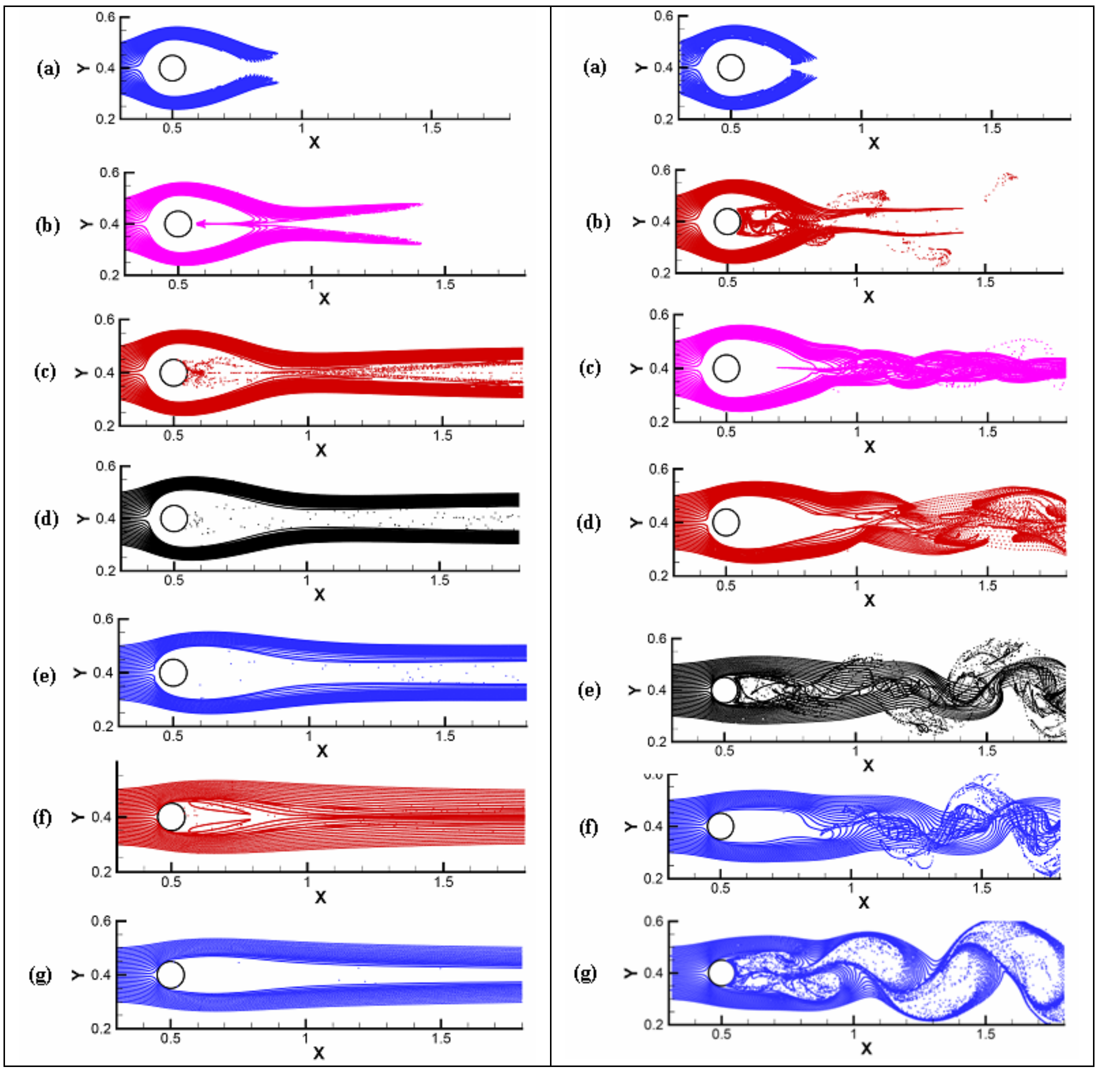

Fig. 6.15: Streaklines at various span wise positions for H/D = 1 (left) and H/D = 2 (right): (a) z/D = 0.02, (b) z/D = 0.05, (c) z/D = 0.1, (d) z/D = 0.2, (e) z/D = 0.5, (f) z/D = 1 and (g) z/D = 1.95.

The necklace vortex, at the junction between the flat plate and the circular cylinder, constrains the released particles on the upstream of the cylinder, to avoid necking around the circular cylinder. Here, at various spanwise heights, numerical tracers are released to mimic the ink shedding process in experiments. The presence of a horse shoe vortex has been clearly captured in the figures for $z/D \leq 0.2$. This is validated with the experimental results of Dargahi [119] in Fig. 6.16.

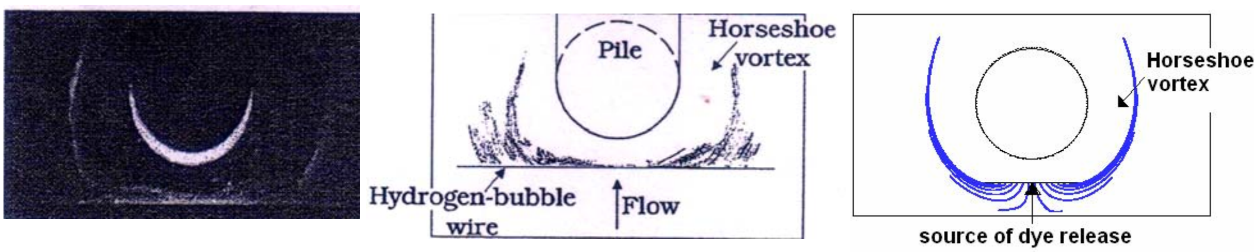

(a) (b) (c)

Fig. 6.16: Horseshoe vortex visualized by hydrogen bubble visualization technique in (a) and (b) (source: Sumer and Fredsøe [120]), show a good comparison with the present numerical simulations in (c).

In the experiments as well as in the present numerical simulations, the existence of horseshoe vortex manifests itself by the absence of bubbles (tracers) in the immediate neighborhood of the cylindrical structure. The problem of scour formation around slender piles on river beds is akin to the present investigations. In this context, Sumer and Fredsøe [120] have identified the occurrence of the following changes in fluid flow features:

(i) Induction of down flow as a consequence of flow deceleration in front of the pillar.

(ii) Generation of horseshoe vortex in front of the pillar.

(iii) Formation of flow pattern in the form of vortex shedding on the leeward side of the pillar.

(iv) Contraction of streamlines at the side edges of the pillar.

In the present investigation, all the above features were noticed for the finite sized cylinder mounted on a flat plate. Velocity vectors in a vertical plane through the cylinder on the upstream side of the cylinder is depicted in Fig. 6.17 for H/D = 10.

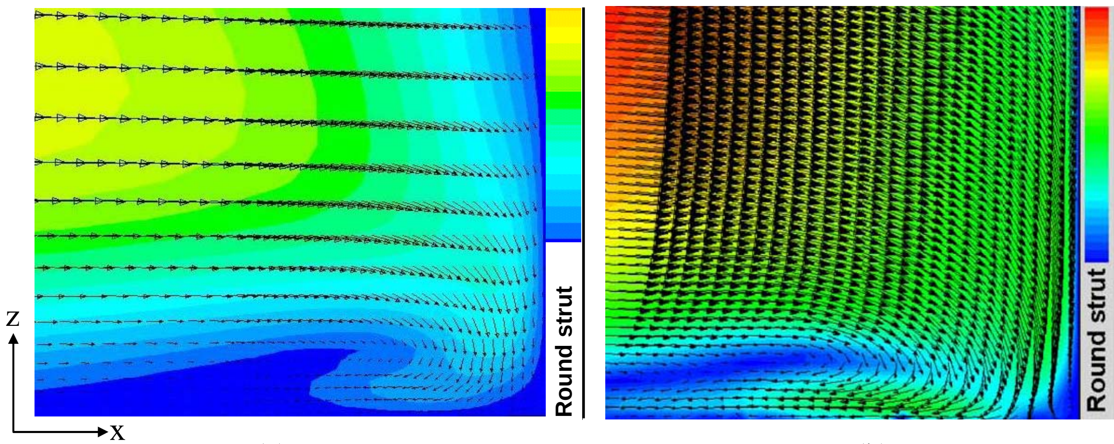

(a) (b)

Fig. 6.17: Time average velocity vectors along the vertical plane (y/D = 0) through the cylinder for H/D = 10, flow from left to right: (a) present simulation Re = 200 and (b) Marakkos and Turner [121] for Re = 5140.

A close up view of the zone closer to the junction between the cylinder and flat plate reflects the existence of reverse flow closer to the flat plate. Due to the presence of shear along the span wise height of the cylinder, velocity increases with distance away from the bottom wall, which creates a static pressure gradient along the vertical direction. Therefore, the incident flow first turns towards the wall junction, and then reverses to move upstream. This indeed explains the origin of the circulation associated with the horseshoe vortex system. By coating Napthalene on the surface of a cylinder, Goldstein and Karni [122] have conducted wind tunnel experiments to study the mass transfer characteristics. In particular, the primary and secondary horseshoe vortex system was found to have a dominant influence.

In order to study the three-dimensional nature of the flow in greater detail, Marakkos and Turner [121] have integrated the continuity equation from the plane velocity data at z/D = 0 to obtain w values at z/D = 0.1. This was achieved by the trapezoidal integration of Eq. (6.11) starting from $w = 0$, at z/D = 0.0.

$$w_{(i,j,k+1)} = w_{(i,j,k)} - \int_{k}^{k+1} \left(\frac{\partial u}{\partial x} + \frac{\partial v}{\partial y} \right)_{(i,j,\hat{k})} dz \tag{6.11}$$

where, i, j, k are the unit vectors along the x, y and z axes, respectively, in a three-dimensional grid and $(\partial u/\partial x + \partial v/\partial y)$ refers to the normal strain. Central differences were used to calculate the in-plane velocity derivatives, $\partial u/\partial x$ and $\partial v/\partial y$. Figure 6.18 shows the patterns of three-dimensional pathlines, obtained from the above procedure.

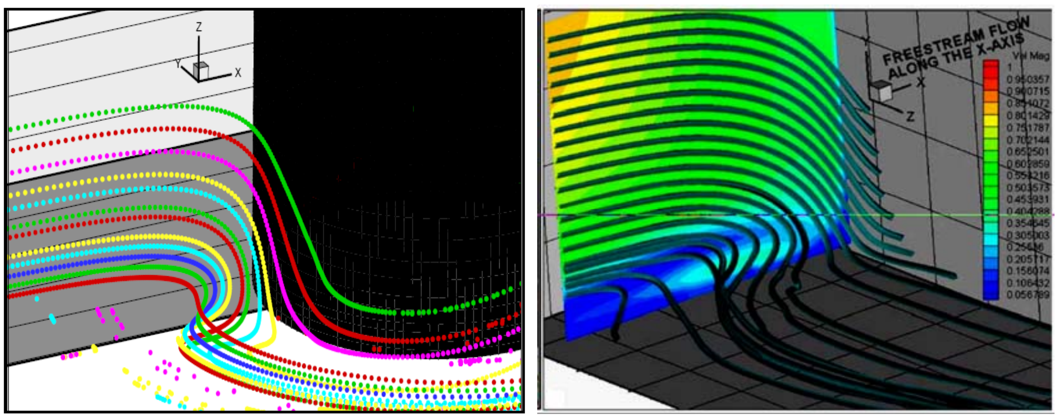

Present simulation Marakkos & Turner [120]

Fig. 6.18: Pathlines in a vertical plane (y/D = 0.01) on the upstream of the cylinder for H/D = 10: left (present simulation) and right (Marakkos & Turner [121] for Re = 5140).

These pathlines illustrate how the free stream and near-wall fluids migrate towards the end wall junction as a result of the relatively low static pressure that exists at the junction. In a similar context, Tiwari et al. [123] have shown particle paths reflecting existence of screwlike helical vortex motion in the region close to the circular tube. They have found significant normal velocity component w, in the wake zone due to pressure gradient in the direction normal to the no slip walls towards the midplane. They have presented time average fluid flow features similar to those shown in Fig. 6.19, which depicts the wake formation region behind the cylinder at various spanwise heights.

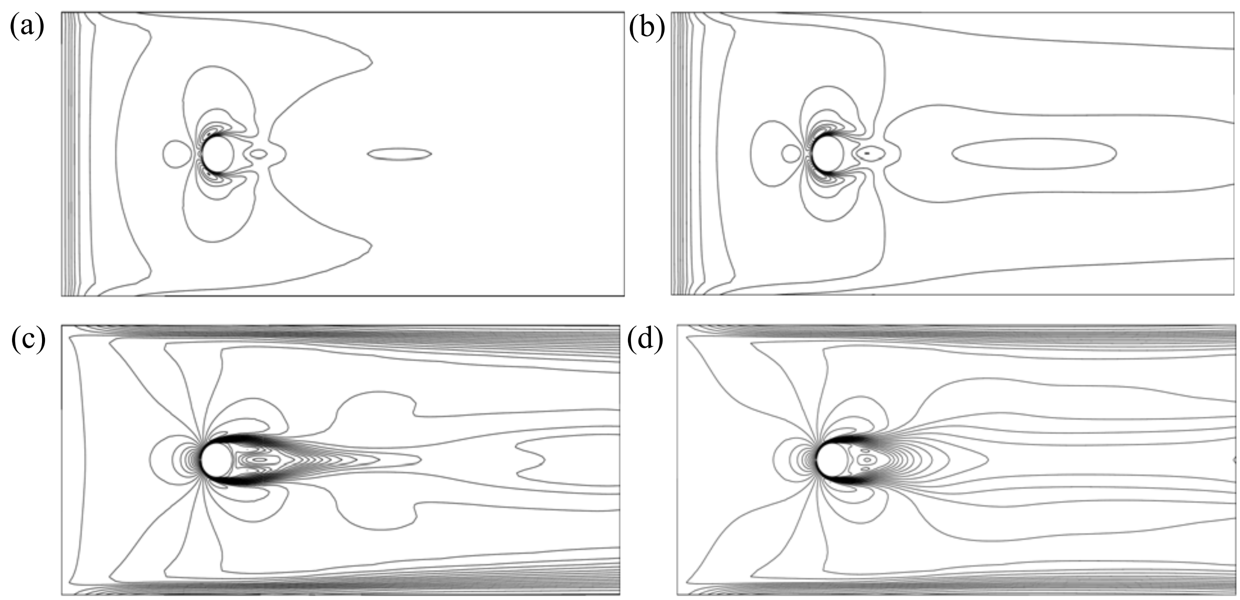

Fig. 6.19: Time averaged velocity distribution at various span wise positions for H/D = 10: (a) z/D = 0.01, (b) z/D = 0.02, (c) z/D = 1 and (d) z/D = 9.

6.4.3. Suppression of vortex shedding

The presence of a horse shoe vortex at the junction has a dominating effect for flow past a low aspect ratio circular cylinder. The interaction between irrotational outer fluid and horseshoe vortex into the wake formation region results in the annihilation of vortex shedding at different spanwise heights. Figures 6.20 and 6.21 depict streak line plots at various span wise heights for both H/D = 1 and 10 plotted at different z/D values.

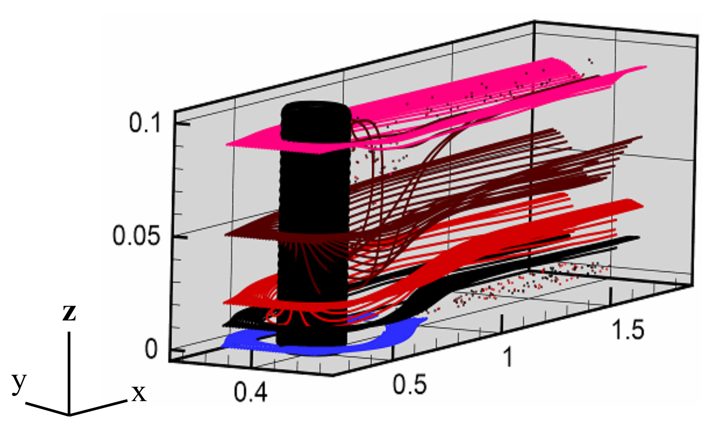

Fig. 6.20: 3-D streaklines along various span wise heights demonstrating vortex shedding suppression at H/D = 1.0.

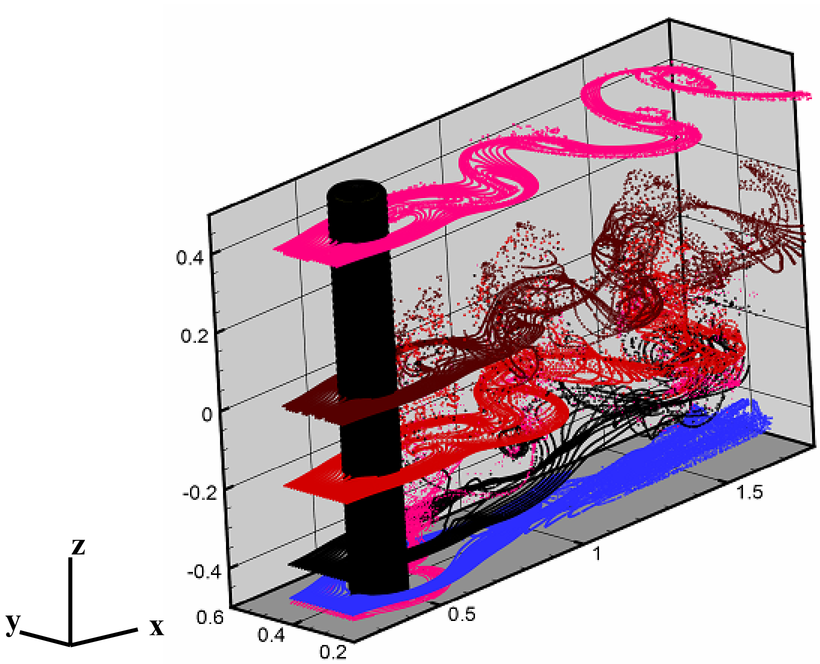

Fig. 6.21: 3-D streaklines along various spanwise heights demonstrating the presence of vortex shedding for H/D = 10.

It can be noticed that, dye released from layers closer to the bottom wall get convected with sinuous features along the span wise direction. For H/D = 1, the unsteady wake features are completely suppressed. This result is further vindicated by FFT analysis presented in Fig. 6.22.

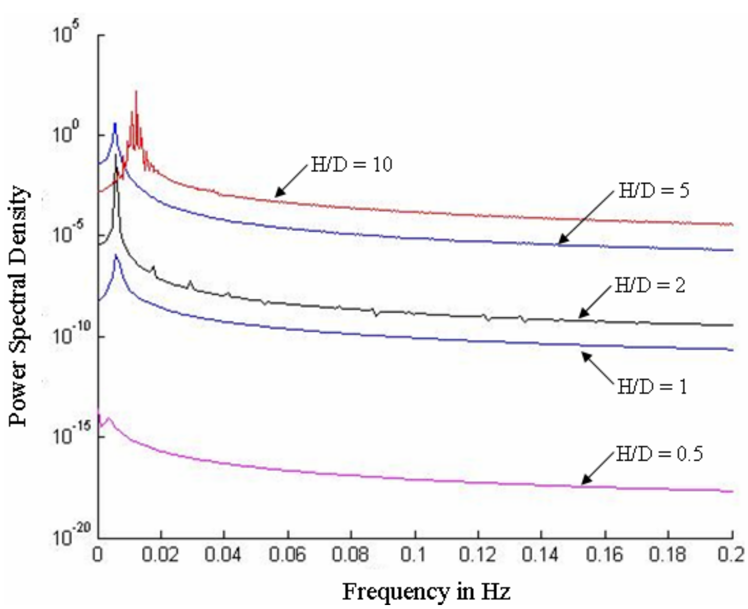

Fig. 6.22: Power Spectral Density from the fluctuating lift coefficient histories for different values of H/D.

The frequency spectrum in the lift coefficient history plot is determined through FFT analysis and plotted against power spectral density. For H/D = 2 and 5 a single dominant peak can be noticed, while such a peak is only notional for H/D = 0.5 and 1.0. However, for H/D = 10, there are two peaks closer to each other indicating vortex shedding influenced by bed friction and lack of it. The instantaneous pressure contours are depicted in Fig. 6.23 for different H/D values of 1, 2, 5 and 10 for the same z/D value of 0.25. For H/D = 1.0, complete vortex shedding suppression can be noticed. However, at the same elevation, vortex street prevails for H/D ≥ 2.0. This result amply demonstrates the influence of finite aspect ratio effects on a circular cylinder mounted on a flat plate.

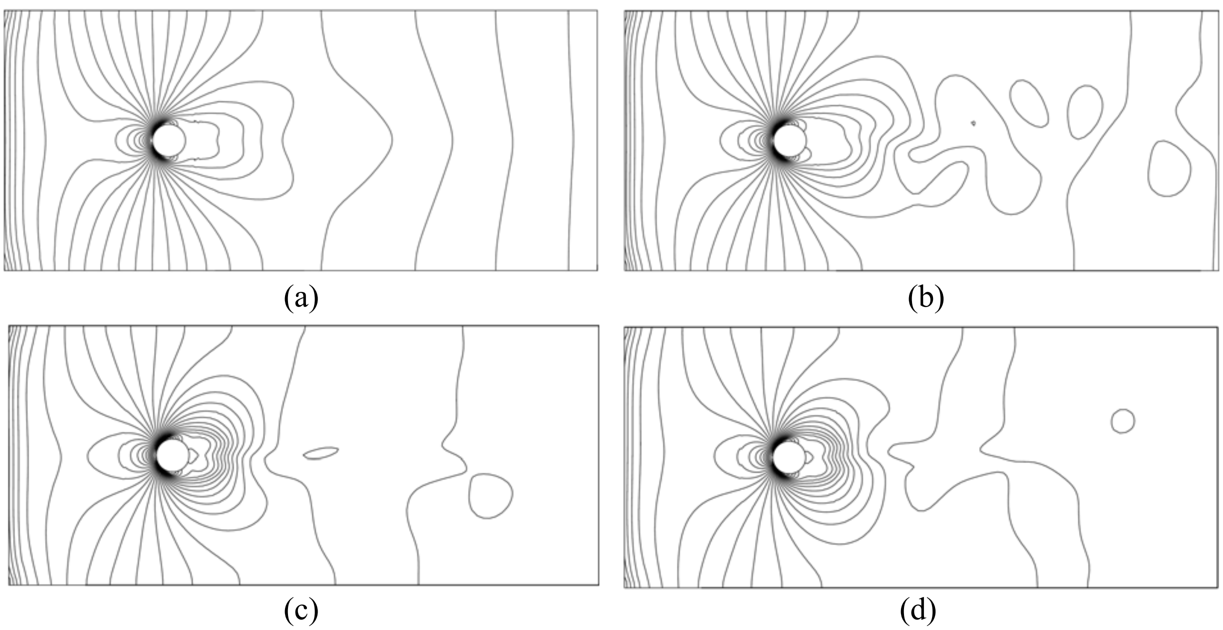

Fig. 6.23: Instantaneous static pressure distribution for different H/D values: (a) H/D = 1, (b) H/D = 2, (c) H/D = 5 and (d) H/D = 10 at same span wise location z/D = 0.25. Note in particular the absence of vortex shedding for H/D = 1.

6.5. FLOW PAST 3D CYLINDER WITH ACCELERATED BOTTOM

In order to investigate the effect of accelerated bottom on the free surface velocity since the reactor pool bed is not flat, flow past a finite circular cylinder (H/D = 10) with accelerated bottom is also studied. The domain considered for the present study is shown in Figure 6.24

wherein inclination of the bottom plate is 15° with respect to horizontal. The mesh pattern and the other numerical details are in accord with the case of flat plate bottom.

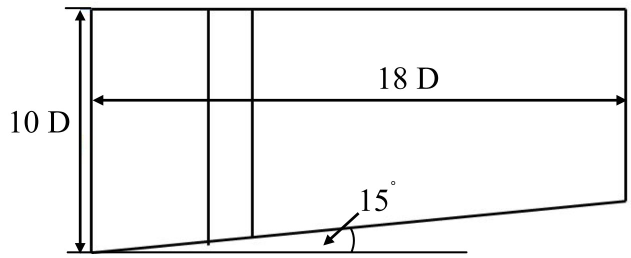

Fig. 6.24: Flow domain considered to access the effect of accelerated bottom.

Various phases of vortex shedding prevailing at different span wise heights for H/D=10 are depicted in Fig. 6.25. The fluid flow features are modified due to introduction of wall friction on the accelerated bottom plate. The periodic vortex shedding behind the cylinder has completely ceased for smaller aspect ratio (z/D = 0.05). Two symmetric standing vortices are observed for aspect ratio z/D = 1 of the cylinder, while the size of the vortex pair grows away from the surface along the span wise direction. Alternate shedding is observed at a higher aspect ratio where bed friction has no significant effect as evident from Fig. 6.25.

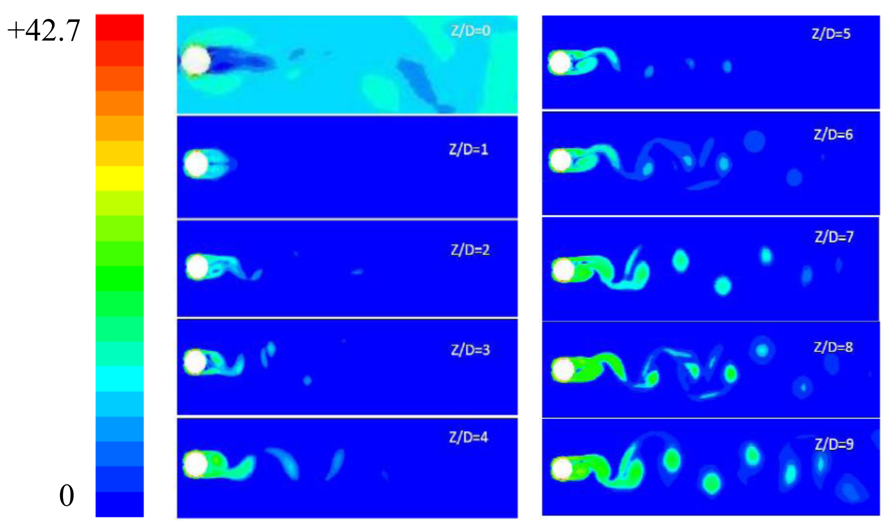

Fig. 6.25: Vorticity contours at different span wise positions, along the axial length of the circular cylinder with bed friction for aspect ratio H/D = 10.

The magnitude of velocity contours for accelerated bottom plate is compared with the flat plate bottom, and is depicted in Fig. 6.26. The effect of bed friction and span wise correlation with independent cellular pattern can be clearly noticed.

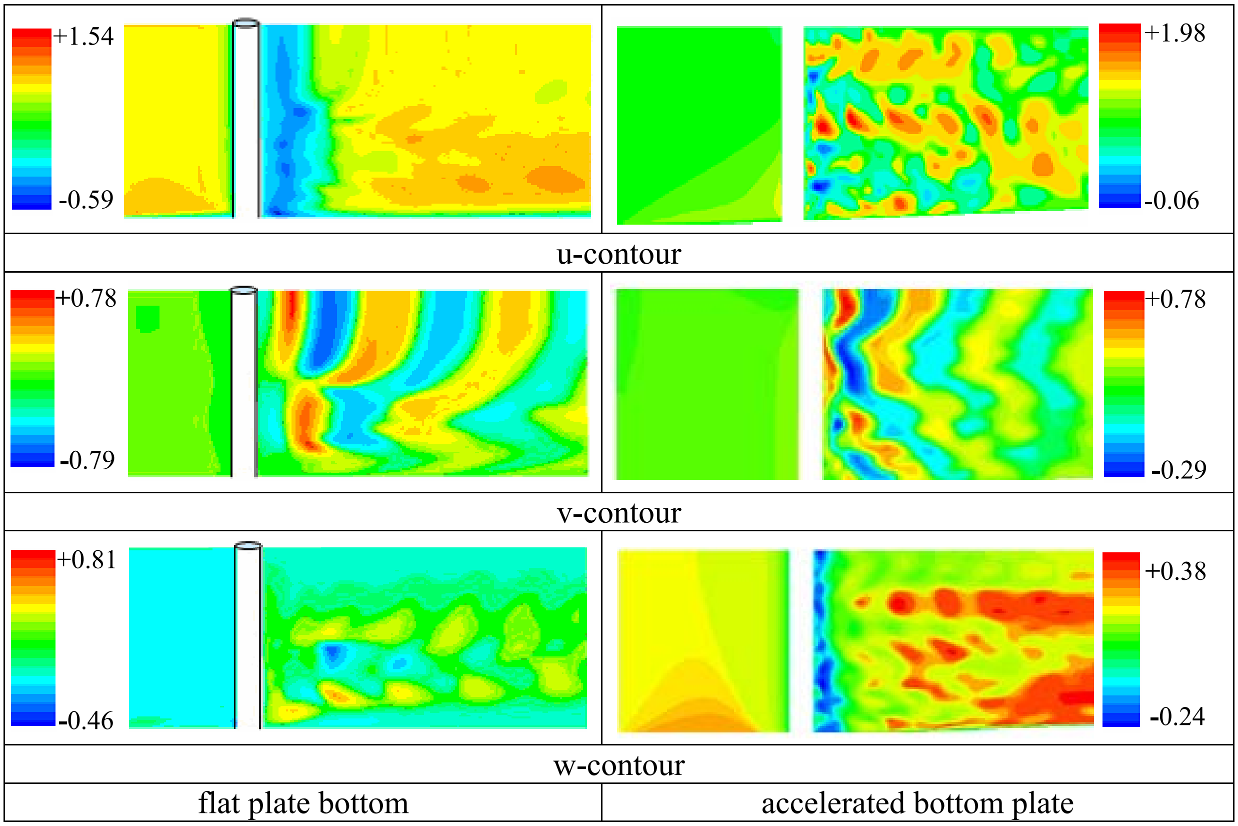

Fig. 6.26: Comparison of velocity contours in a vertical plane (y/D = 0) through the cylinder for H/D = 10 (with bed friction) at Re=200.

The formation of horseshoe vortex around the cylinder is reflected in streak line plots as shown in Fig. 6.27 for H/D = 10. The presence of a horseshoe vortex has been clearly captured in figure. Flow past the cylinder with an accelerated bottom results in an intense street formation which contributes to higher surface velocities than that in flat beds.

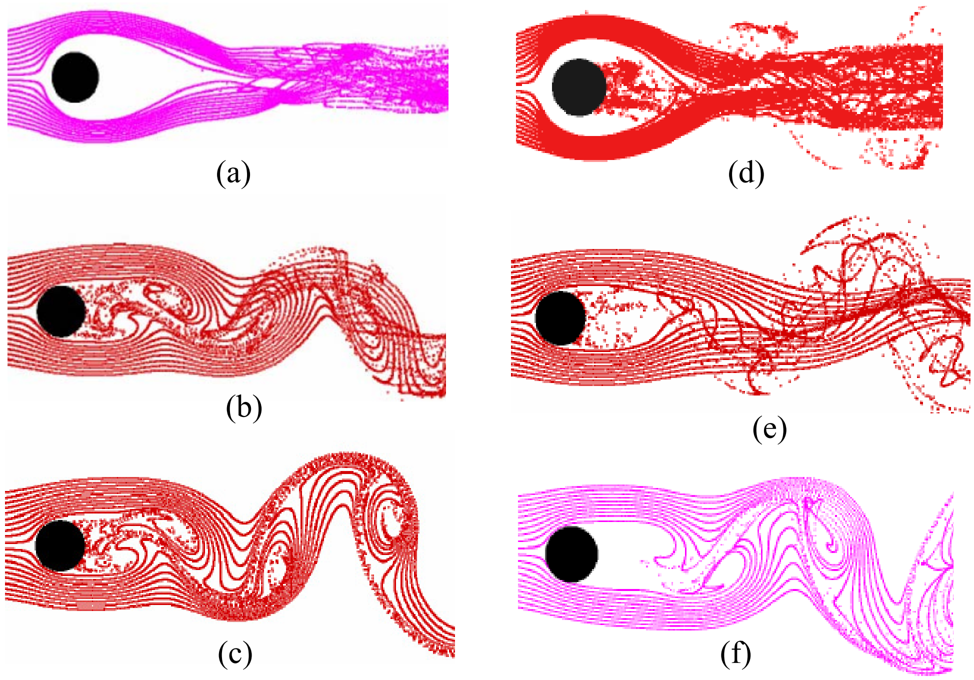

Fig. 6.27: Streak lines released from different span wise heights (H/D=10). Left side represents the streak visualization for accelerated bottom where as right side represents for flat bottom (a) & (d) Z/D = 0.01, (b) & (e) Z/D =5 and (c) & (f) Z/D = 10.

6.6. CLOSURE

3-D laminar flow past a finite circular cylinder mounted on a flat plate is numerically investigated. The influence of bed friction on the junction flow between the flat plate and the circular cylinder results in the formation of the horseshoe vortex system. Streamwise and transverse forces on the cylinder are determined to study the finite size effects, for different liquid depths. Parametric study is conducted for cylinder aspect ratios (H/D) = 0.5, 1.0, 2.0, 5.0, and 10.0 at Re = 200. Based on the numerical simulations conducted in the present study, the following conclusions can be drawn.

- Flow past a circular cylinder without any end effects results in vortex formation and shedding. However, when this cylinder is mounted on a flat plate with its axis perpendicular to the fluid stream, wake boundary-layer interaction effects would dominate at low H/D (< 1) compared to high H/D values (> 2).

- Although horseshoe vortex is present for all H/D values, the unsteady wake characteristics are not affected for H/D ≥ 2.0, where vortex shedding still prevails at different spanwise heights.

- Vortex shedding is completely suppressed for cylinder heights below H/D ≤ 1.0, due to interaction between the horseshoe vortex at the junction and vortex formation region of the cylinder.

- Accelerated bottom wall is seen to increase the free surface velocity without affecting the vortex shedding process.

CHAPTER 7

INVESTIGATION OF TURBULENT VORTEX SHEDDING PAST A FINITE CIRCULAR CYLINDER MOUNTED ON A FLAT PLATE

7.0. FOREWORD

In the previous chapter, laminar flow around a circular cylinder mounted vertically on a flat plate and with an accelerated bottom plate has been studied. The flow condition prevailing in the reactor is in turbulent regime. Turbulence model plays a vital role in the prediction of flow characteristics behind circular components. Hence, it is essential to identify a suitable turbulence model that is capable predicting required flow features during vortex shedding. Towards this, 3-D flow field around a finite circular cylinder having H/D = 2 has been investigated using various turbulence models. Based on the conclusions from laminar flow investigations, the span wise aspect ratio of 2 has been chosen since, the unsteady wake characteristics are largely not influenced by bed friction beyond H/D = 2.0. To start with, detailed validation of 2-D flow around a circular cylinder at Re = 5×10^4 is carried out using various turbulence models. Flow characteristics viz., Strouhal periodicities, forces acting on the cylinder, mean pressure coefficients are compared with the published literature. It is found that SST *k-ω* model performs better in simulating turbulent unsteady flow features in the vicinity of the cylinder than other eddy viscosity based turbulence models. Following the 2-D studies, detailed 3-D studies on force coefficients, pressure distribution on the cylinder and the spatio-temporal dynamics of interaction between the wake and the boundary-layer have been investigated. The wake characteristics are investigated through streak line visualizations. The numerical results extracted from these simulations have good agreement with the experimental data.

The flow fields around cylindrical bodies are of great interest to a wide range of engineering applications apart from a nuclear reactor. The physics of flow around a circular cylinder is very complex at high Reynolds number. The flow pattern is asymmetric and it shows vortex shedding in the wake region. Additionally, the flow contains different scales of turbulent eddies. To capture these eddy structures, various methods of turbulent flow simulations such as, Reynolds Average Navier Stokes (RANS), Large Eddy Simulation (LES), and Direct Numerical Simulation (DNS) have been used by previous researchers. DNS and LES can provide time accurate turbulent dynamics, but they require very large computational effort due to the fine grid resolution near the solid surface. Therefore they have not been adopted in the present study in spite of the higher accuracy. Instead, RANS approach with various turbulence models have been employed for solving flow around a circular cylinder at high Reynolds number.

An extensive review on flow transition has been discussed by Zdravkovich [124] and Williamson [92]. A critical analysis of numerical predictions of flow past a circular cylinder over a wide range of Reynolds numbers (10^4 to 10^7) was carried by Celika and Shaffer [125] using the standard k-ε turbulence model. Steady flow past a circular cylinder for sub-to-supercritical Reynolds number was simulated by Saghafian et al., [126] using a nonlinear eddy-viscosity model. The model predicted the phenomena of drag crisis at sub critical Reynolds number which is in approximate agreement with the experimental measurements [127]. Travin et al., [128] numerically investigated the flow separation from Re = 5×10^4 to 3×10^6 using detached eddy simulation (DES) technique. It was found that, unsteady Reynolds-averaged simulations are less accurate than DES for laminar separation cases. But they are reasonable to simulate turbulent separation cases. Various aspects of turbulence modeling by varying the turbulent length scale at the inlet using SST k-ω model were studied by Young and Ooi [129] for Re = 1.4×10^5. It was found that the variation in flow parameters such as mean drag coefficient and Strouhal number were influenced by changes in the turbulent boundary conditions.

The turbulent flow field around bridge piers was studied by various authors through experimental [106-107, 118, 130] and numerical simulations [131-133]. Their work was mainly focused on the junction flow and the associated phenomena, viz., formation of horseshoe vortex and scouring mechanisms. Three dimensional numerical simulations of turbulent flow in the wake of a circular cylinder were extensively studied by Persillion and Braza [134]. Their study revealed that, unsteady flow structures get affected depending on the location of the bluff body. A number of investigators [96-100] have studied the aspect ratio effect and the effect of end plates on vortex shedding for finite sized cylinders. While a number of investigators have studied the nature of the wake region, a few have focused on the swirl pattern and free end effects on the cylinder [108, 135-136]. An artificial compressibility based split (CBS) method was presented by Nithiarasu and Liu [137] for the solution of steady and unsteady turbulent flow problems at moderate Reynolds numbers using three different RANS models. It appears that the CBS scheme is very well suited for turbulent flow calculations at moderate Reynolds numbers.

In most of the past studies it is observed that, numerical simulations of turbulent flow past a circular cylinder largely confined to 2-D and 3-D flows at very high and low Reynolds numbers with LES/DNS approach. Limited studies have been performed in the range of sub-critical Reynolds numbers with eddy viscosity based model. The main purposes of the present study are (i) to analyze turbulent unsteady flow field for different Reynolds numbers, (ii) to assess the capability of various Reynolds averaged turbulence models in terms of computing force coefficients along the surfaces of the cylinder and (iii) to compare predicted results with other published experimental and numerical results.

7.1. SOLUTION METHODOLOGY

7.1.1. Governing Equations

The general governing equations have already been described in Chapter-3. Pressure-velocity coupling between the incompressible Navier-Stokes and continuity equations is resolved using the SIMPLE algorithm [79]. The convective and diffusive fluxes are combined using the second order upwind scheme. The temporal part has been solved by an implicit time marching technique with time step (Δt) determined by the CFL condition. To declare convergence at any time step, the absolute error in the discretized momentum and continuity equations is set to below 10^{-4}.

7.1.2. Initial and Boundary Conditions

The boundary conditions for two-dimensional simulations are:

(a). Inlet located at a distance of 7D on the upstream of the cylinder, is imposed with a uniform velocity U_∞

(b). Outlet located at a distance of 18D downstream of the cylinder with zero traction and is specified with a constant pressure

(c). no-slip boundary condition on the cylinder wall, and

(d). no-slip condition on the side confining channel walls located at 7D away from the centre of the cylinder.

For 3-D simulations, additional boundary conditions are needed for the top and bottom walls. The bottom wall is imposed with a no-slip boundary, while a free slip condition is enforced on the top surface. The flow domain of interest with boundary conditions is depicted in Fig. 7.1.

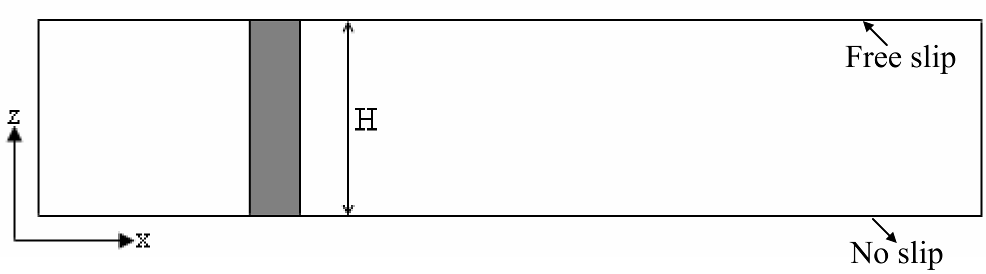

Front view

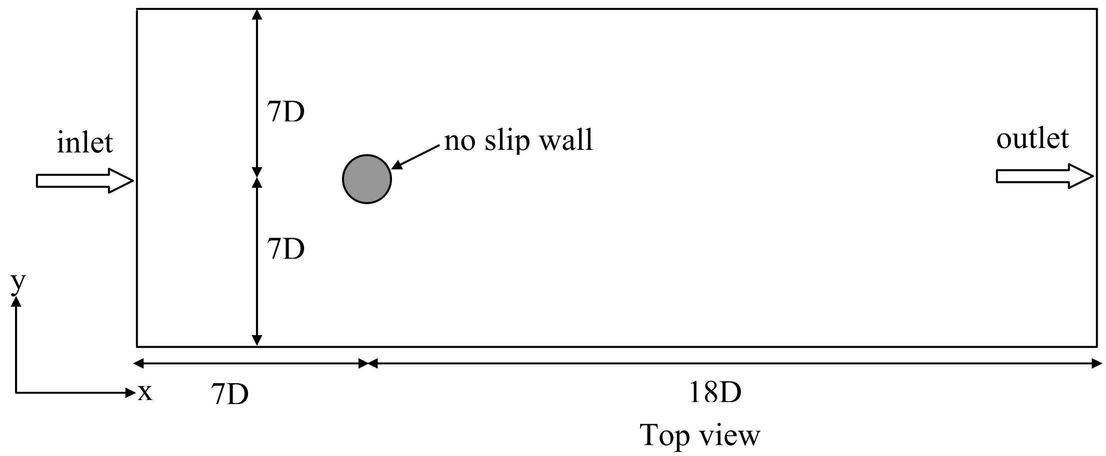

Fig. 7.1: Computational domain of interest with boundary conditions to study 3-D vortex shedding

7.2. RESULTS AND DISCUSSION

7.2.1. Simulation of 2D Flow past a Circular Cylinder

Numerical simulation of turbulent flow past a 2-D circular cylinder at Re = 5×10^4 has been chosen for validation. The Reynolds number is chosen keeping in view that the flow regimes will undergo a transitional change [138]. Numerous experimental and numerical 2-D studies on turbulent flow around bluff bodies have been reported by many researchers [139, 140]. All the studies have some common characteristics: they solve the unsteady Navier-Stokes equation in 2-D formulation and describe the relevant flow by the global parameters such as Strouhal number as a main feature of the unsteady wake, drag and lift coefficients in the wall region. In the present simulation, standard k-ε, RNG k-ε and SST k-ω turbulence models are employed to assess the capabilities of capturing the complex flow features.

7.2.2. Grid Sensitivity Check

Grid sensitivity tests were carried out for Re = 5×10^4, with three different mesh sizes. The flow domain of interest with a non-homogeneous grid pattern is depicted in Fig. 7.2(a). The close–up view of the mesh around the cylinder surface, shown in Fig. 7.2(b) reflects fine mesh is clustered around the cylinder.

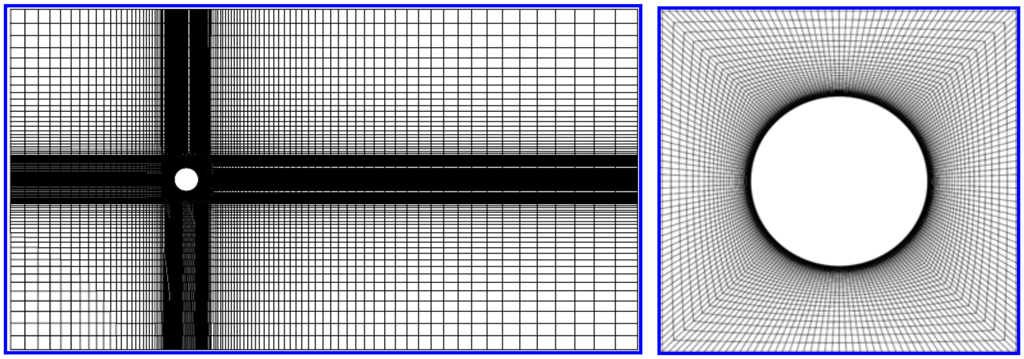

(a) Top view (b) close-up view

Fig. 7.2: Typical global grid pattern around the cylinder adopted for numerical simulation: (a) a view of the top surface and (b) close-up view around the periphery of the cylinder.

Different mesh sizes employed for the grid sensitivity study are shown in Table-7.1. Furthermore, to capture the junction flow features, appropriate grid size is considered at the junction between the bottom wall and the cylinder, keeping y^+ value into consideration. Here, the force coefficients (C_D and C_L), Strouhal number (St) and CPU time requirements associated with grid sizes are presented. It can be noticed that the difference between the results obtained with mesh M2 and M3 is very small, thus justifying the use of the M2 mesh for further investigations.

Table-7.1: Grid sensitivity study for Re = 5×10^4.

Mesh	No. of 2D control volumes	Min. Radial grid spacing	C_D	C_L	St	CPU Time per iteration (s)
M1	24,144	0.018D	1.024±0.07	±1.0	0.23	5
M2	30,144	0.015D	1.052±0.081	±1.03	0.23	7
M3	36,944	0.013D	1.055±0.085	±1.04	0.24	9

7.2.3. Validation of Unsteady Wake Characteristics

Spatio-temporal dynamics of the wake behind the circular cylinder is investigated using a mesh of size M3. The predicted Strouhal number and mean drag coefficient are compared with other published experimental and numerical investigations and are presented in Table-7.2. It can be seen from Table-7.2 that the C_D value predicted from the present study compares well with the literature data.

Table-7.2: Comparison of Strouhal number and drag coefficient for flow past a circular cylinder at Re = 5×10^4.

Reference	St	C_D
Rosoko [91]	0.19	1.20
Samapao and Coutinho [141]	0.22	1.55
Travin et al., [128]	0.22	1.05
Achenbach [138]	--	1.04
Present study (SST k-ω)	0.23	1.03
RNG k-ε	0.24	1.32
Standard k-ε	0.23	1.22

Pressure distribution around the cylinder for different turbulence models is depicted in Fig. 7.3. It is seen that the flow separates around $\theta = 80^\circ$ (θ is measured from the front stagnation point of the cylinder) in the present turbulence models where as it deviates from the experimental values. The differences between the numerically predicted C_p value and experiment can be attributed to the fact that the present two equation turbulence models have limitations in predicting local pressures. The inability of these models to predict the bluff body flows is due to the assumption of homogeneous and isotropic turbulence. These models often produce excessive eddy viscosity, which induces more damping, thus delaying separation.

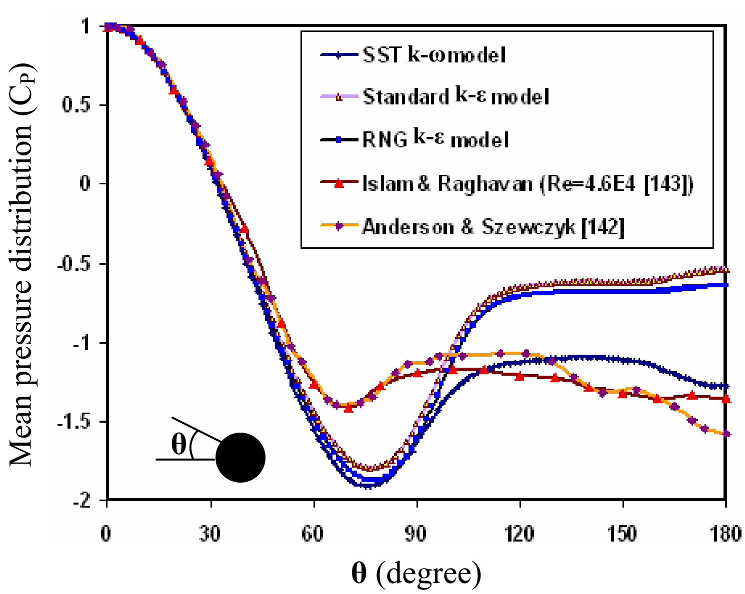

Fig. 7.3: Time averaged mean pressure coefficient distribution around the cylinder for different turbulence models.

It is found that SST k-ω model agrees better with the experimental data than the other turbulence models, viz., standard k-ε model and RNG k-ε model. From the above numerical results, it is clear that SST k-ω model is capable of simulating the complex flow structures around a circular cylinder at high Reynolds number, with reasonable accuracy.

7.2.4. Finite Aspect Ratio Effects of Flow past a Circular Cylinder

Three-dimensional flow on a wall mounted circular cylinder can be influenced by the aspect ratio, i.e. the ratio of cylinder height to the diameter (H/D). This produces three-dimensional effects by interaction with the wall boundary layer, which also affects the flow behind a cylinder. The growth of boundary-layer (δ) on the flat plate influences the vortex shedding past the cylinder leading to wake-boundary-layer interaction.

7.2.4.1. Forces on the Circular Cylinder

The temporal evolutions of lift and drag forces on the cylinder for various turbulence models are given in Table-7.3.

Table-7.3: lift and drag force coefficients for Re = 2×10^4 and 4×10^4 in 3D flow past a circular cylinder

Turbulence model	Reynolds number	C_D	C_L
RNG k-ε	20,000	0.7	± 0.1
SST k-ω		0.96	± 0.3
Szczepanik et al, [Re = 21,580, 144]		0.985	-
RNG k-ε	40,000	0.66	± 0.1
SST k-ω		0.90	± 0.2
Travin et al, [128]		1.05	±0.21

Two Reynolds numbers (2×10^4 and 4×10^4) have been chosen for this numerical study. From the table it is seen that, the value of C_D obtained from SST k-ω model closely matches with the reported result where as RNG k-ε model underpredicts the lift and drag coefficient values. The temporal variation of C_D and C_L at Re = 4×10^4 is depicted in Fig. 7.4. The deviation in C_L value from 2-D values is due to the effect of bed friction imparted to the cylinder, as observed in laminar vortex shedding (see Fig. 6.12).

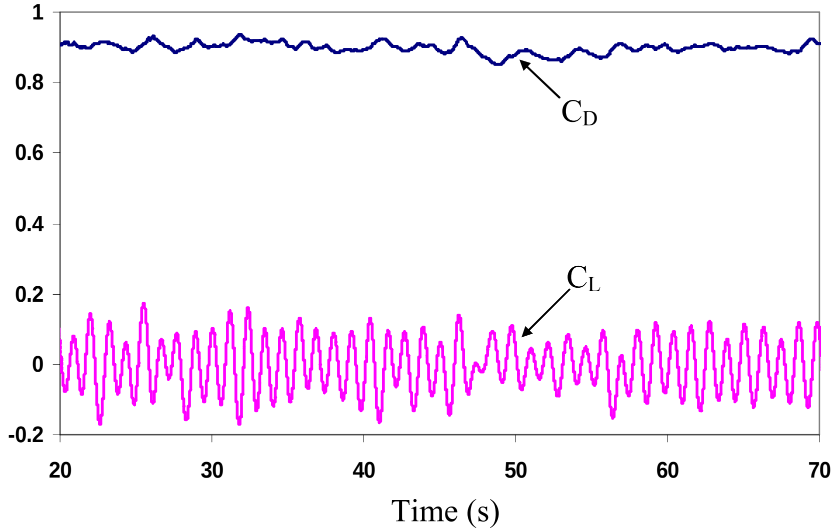

Fig. 7.4: Temporal variation of drag and lift coefficients for Re = 4×10^4 (SST k-ω model).

7.2.4.2. Vorticity Contours

The contours of the vorticity magnitude at a given time instant and at various span wise heights for Re = 2×10^4 are depicted in Fig. 7.5.

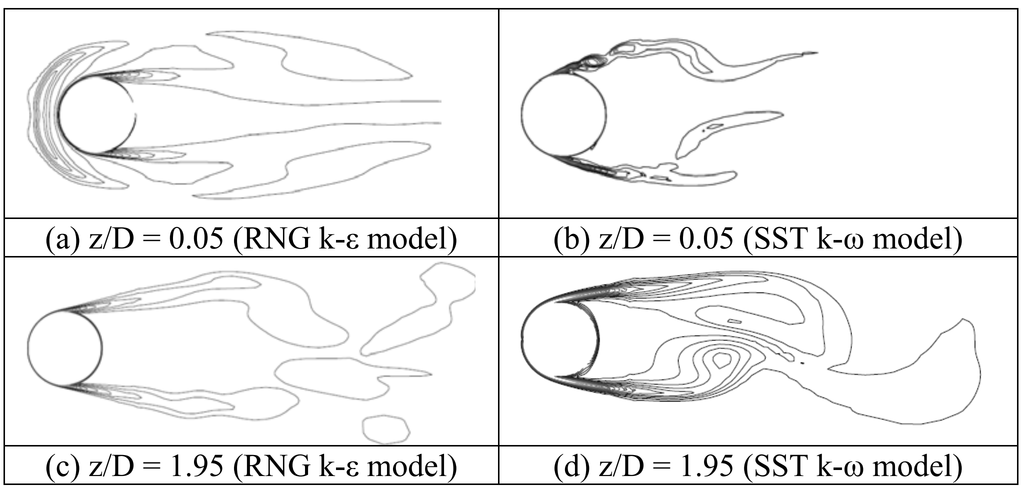

(a) z/D = 0.05 (RNG k-ε model) (b) z/D = 0.05 (SST k-ω model)

(c) z/D = 1.95 (RNG k-ε model) (d) z/D = 1.95 (SST k-ω model)

Fig. 7.5: Contours of voriticity at different spanwise heights at Re = 2×10^4 using different turbulence models.

At a span wise height of z/D = 0.05 from the bed, vortex shedding is completely suppressed due to bed friction in both the turbulence models, which are evident from Fig. 7.5(a) and 7.5(b).

Standing vortex is formed behind the cylinder showing the suppression of vortex shedding. Coherent structures are visible in the wake at the free surface, i.e, z/D = 1.95 for SST k-ω model where as the process of vortex shedding is weakly captured through RNG k-ε model. The boundary-layer separation is much delayed and the wake is narrower, resulting in a much smaller drag and lift force coefficients. It is well known that standard k-ε model is inadequate for separation dominated bluff body flows.

7.2.4.3. Capturing Horseshoe Vortex

Bed friction forms the necessary condition for the generation of horseshoe vortex system, at the junction between upstream of the circular cylinder and the flat plate. However, an adverse pressure gradient is needed for triggering the sufficiency condition for the flow separation to take place, which in turn would generate horse shoe vortex. In order to visualize the spatio-temporal dynamics of the near wake, a group of particles are injected at certain position on the upstream of the cylinder surface at z/D = 0.02. The formation of horseshoe vortex around the cylindrical structure may be surmised to be present, as the streakline plot in Fig. 7.6 reflects the enveloping region.

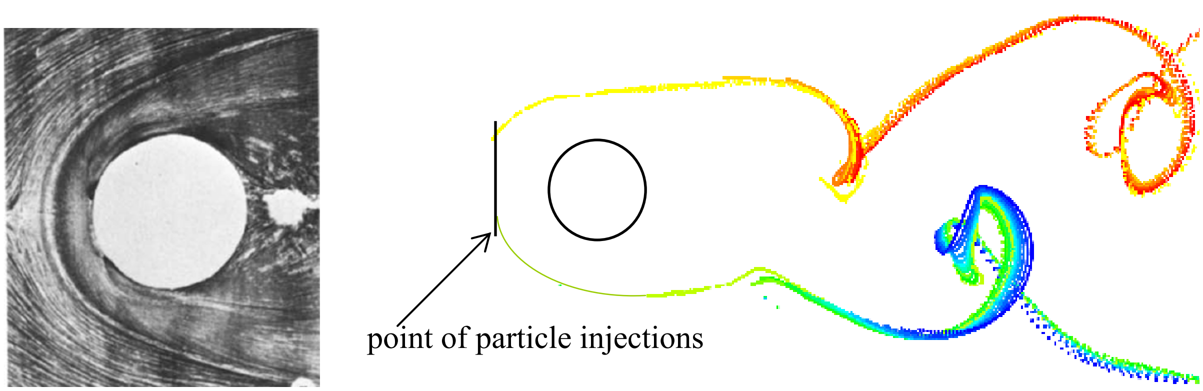

(a) Oil-flow visualization (b) Present simulation

Fig. 7.6: Flow visualization: (a) Baker [108] at Re = 1.1×10^5 and (b) present streakline visualization for Re = 4×10^4 using SST k-ω model.

The necklace vortex, at the junction between the flat plate and the circular cylinder, constrains the released particles on the upstream of the cylinder, to avoid necking around the circular cylinder. The numerical streak line visualization is compared with the experimental oil-flow visualization carried out by Baker at Re = 1.1×10^5 [108].

Time averaged velocity vectors predicted by SST k-ω model in a vertical plane through the cylinder for H/D = 2 at Re = 2×10^4 is depicted for the upstream side in Fig. 7.7.

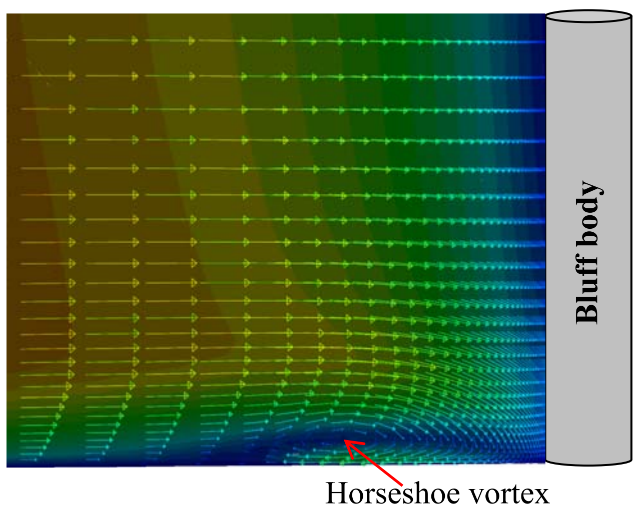

Fig. 7.7: Time average velocity vectors along the vertical plane (y/D = 0) through the cylinder for H/D = 2, Re = 2×10^4.

The streamline patterns superimposed on velocity vectors illustrate how the free stream and near-wall fluid migrates towards the end wall junction as a result of the relatively low static pressure that exists at the junction. In addition, the streamlines close to the end-wall demonstrate that the incident flow first turns towards the wall, then reverses to move upstream. This explains the origin of the circulation associated with the horseshoe vortex system. Similar pattern has already been described by Dargahi [119]. The instantaneous velocity vectors at free surface are depicted in Fig. 7.8 at Re = 2×10^4. Regular vortex shedding can be noticed on the free surface. However, using the same turbulence model, vortex street gets suppressed for z/D = 0.05. This result amply demonstrates the influence of aspect ratio effects on a circular cylinder mounted on a flat plate.

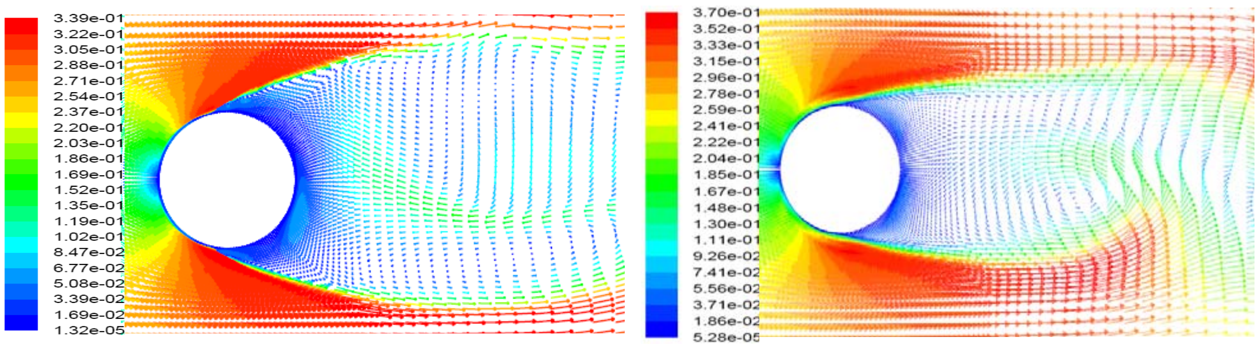

(a) z/D = 0.05 (b) z/D = 1.95

Fig. 7.8: Velocity vectors at Re = 2×10^4 predicted by SST k-ω model: (a) z/D = 0.05 and (b) z/D = 1.95.

7.3. CLOSURE

The 3-D flow field around a circular cylinder mounted vertically on a flat plate has been numerically investigated using different turbulence models for an aspect ratio of 2. Detailed validation studies for 2-D flow around a circular cylinder at Re = 5×10^4 are carried out. Flow characteristics viz., Strouhal periodicities, forces acting on the cylinder, mean pressure coefficients are compared with the published literature. It is found that SST k-ω model better predicts the unsteady flow features at high Reynolds number than other eddy viscosity based turbulence models. Force coefficients, vorticity distribution around the cylinder and the spatio-temporal dynamics of interaction between the wake and the boundary-layer have been investigated for 3-D flows. The numerical results extracted from these simulations have shown good agreement with the experimental data.

CHAPTER 8

INVESTIGATION OF GAS ENTRAINMENT IN THE HOT POOL FREE SURFACE DURING CROSS FLOW OVER A CYLINDRICAL COMPONENT

8.0. FOREWORD

Flows past a free surface piercing cylinder are numerically investigated in order to understand the vortex activated gas entrainment phenomena inside the sodium pool of a fast breeder reactor. In general, the presence of free surface adds complexities to the flow due to the generation of waves in various forms and their interaction with the bluff body, vortex formation and interfacial effects like bubble entrainment. Several experimental and numerical studies on flow past an interface piercing cylinder are reported by various authors, describing the effect of Reynolds number and Froude number, which are major parameters influencing the structures of the flow.

Akilli and Rockwell [105] investigated the near wake of a surface piercing cylinder in shallow water at Re=10,052 using a combination of visualization marker with PIV techniques. They observed significant distortion of the free surface due to a horizontal vortex induced by the upward ejection of fluid through the center of a Kármán vortex. Lang and Gharib [145] studied the wake behind a surface-piercing cylinder for a clean and contaminated free surface at low Reynolds numbers ranging from 350 to 460 and Froude numbers (Fr) below 1.0, to investigate the effect of varying free surface conditions. For the clean surface case, a zigzag vortex pattern was observed due to large surface deformation. When the free surface was contaminated by surfactants, the surface was no longer stress-free and a horseshoe vortex was generated from the surface. Experimental studies conducted by Inoue et al., [146] at Re=27,000 and 29,000 with Fr = 0.8 and 1.0 showed that the periodic vortex shedding was apparent in the deep flow, whereas the periodic component of fluctuations was reduced and random fluctuations of higher frequency were more prominent near the free surface. Kawamura et al., [147] and Suh et al., [148] studied the cases of Re=27,000 and Fr = 0.2, 0.5 and 0.8 using Large Eddy Simulation based Smagorinsky subgrid-scale (SGS) model. They observed that wave–wake interaction becomes stronger as Froude number increases and predicted significant surface fluctuations inside the recirculation zone immediately after the surface wave crest. In addition, they were able to visualize the attenuation of vortex shedding near the free surface. Similarly, Yu et al., [149] studied flow past a free surface piercing cylinder at Froude numbers up to 3.0 and Reynolds numbers up to 10^5 using LES based Smagorinsky SGS model with VOF method. Tezduyar [150] highlighted interface-tracking and interface-capturing techniques developed for computation of flows with moving boundaries and interfaces.

Zanden et al., [151] and Thomas and Williams [152] have separately applied LES to open channel flows. Salvetti et al., [153] have studied the decay process of turbulence under a free surface by LES with dynamic-type SGS models. Most of the previous studies on flow past a free surface piercing cylinder have been dealt with by LES formulation. However, very little work has been using two equation turbulence models on wave-wake interaction phenomena, and this is one of the motivations for the current study. The two equation model demands only a limited computational resource compared to the LES model [154]. Based on the recommendation of the previous studies discussed in Chapter - 7 on the choice of turbulence model the SST k-ω turbulence model is adopted in the present study. A two-phase volume of fluids (VOF) technique is employed to simulate the air-water interface. The predicted result is validated with the published LES result. The effect of the free surface on the vortex structure is investigated in detail at various Reynolds and Froude numbers. For various inflow velocities, the re-submergence angle and the free surface velocity at the point where the surface slope changes abruptly are measured.

8.1. GOVERNING EQUATIONS

The fluid flow around partially submerged cylindrical structure is governed by 3-D transient incompressible form of Navier-Stokes equations and continuity equation. The standard transport equations for turbulent kinetic energy (k) and specific dissipation (ω) are given by Wilcox [59]. VOF method is used to track the interface between the liquid and gas phases [15]. PISO algorithm [52] is used to solve the pressure velocity coupling between the incompressible Navier-Stokes and continuity equations. First order upwind scheme is used to combine the convective and diffusive fluxes. The temporal part has been solved by an implicit time marching technique with time step (Δt) determined by the CFL condition. From phase fraction information, geometric reconstruction of the interface shape is obtained. To declare convergence at any time step, the absolute error in the discretized momentum and continuity equations is set to $< 10^{-4}$.

8.1.1. Validation of VOF Problem

Flow past a cylinder close to a free surface is an apt problem to validate the dynamics of interface capture. The numerical model closely resembles the experimental setup of Hyot and Sellin [155]. The flow domain of interest consists of an open channel of width 1.2 m and height 0.3 m of which the bottom two-thirds is maintained with water and the rest with air, which is open to atmosphere. A cylinder of 0.067 m diameter (with its axis perpendicular to flow direction), is placed at a distance of 0.15 m from the inlet side of the channel. The fluid flow velocity remains constant for all the simulations at 0.43 m/s. This in turn results in constant values of Reynolds and Froude numbers. The depth of the top surface of the cylinder is h. Values of the parameter $h^*= h/D$ ranges from 0 to 0.75. The parametric details related to the benchmark problem are shown in Fig. 8.1(a). Tracking of flow lines is performed by injecting a group of particles from upstream side of the cylinder during the simulation. The particle tracks depicting bent interface between water and air are compared in Fig. 8.1(b) for $h^* = 0.0$. A good visual comparison against Hyot and Sellin [155] can be noticed. It can also be seen that the tracer provides an entirely similar picture of the major flow structure compared with the PIV display. A mixing layer emanating from the lower surface of the cylinder, together with a jet-like flow issuing from the upper surface region, wrapp around the downstream region of the cylinder which is depicted in Fig. 8.1(b). A Coanda like effect on the top-side is particularly promoted by the air-water interface. These features are in accord with the description given by Sheriden et al., [156].

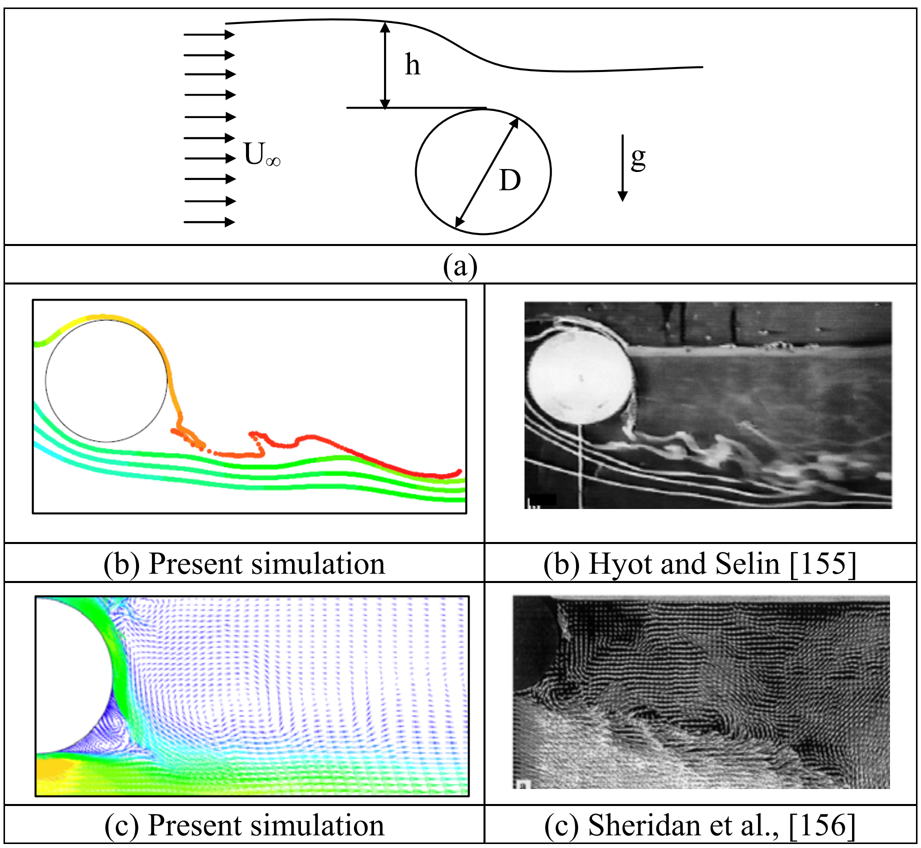

Fig. 8.1: (a) Flow past a horizontal circular cylinder placed in a partially filled channel (b) streaklines around the cylinder at the interface for $h^* = 0$ and (c) velocity field for $h^* = 0.3$.

Further a quantitative comparison of PIV and tracer results was made by measuring flow angles at a point defined by a vertical line tangent to the rear of the cylinder, as shown in the sketch, inside Table-8.1. The measurement certainly had a subjective aspect, but an attempt was made to estimate the angle at the midpoint between the free surface and the shear layer leaving the cylinder, and also a similar region from the lower side of the cylinder. A comparison of the measured angles of flow leaving the top and lower regions of the cylinder is given in Table-8.1. The comparison shows that the tracer, PIV measurements and the present simulations are in reasonable agreement with each other. The percentage of deviation of the present simulation for some of the cases of the tracer and PIV results are within 15 %. Furthermore the comparison between the present numerical studies and the PIV measurements indicate that at angle $\alpha_2 < 12^{\circ}$, air entrainment is almost negligible. This demonstrates the validity of the VOF method employed.

Table–8.1: Comparisons of flow angles (α_1) and (α_2) against published data.

h^*	α_1^0			α_2^0		
	Tracer [155]	PIV [156]	Present study	Tracer [155]	PIV [156]	Present study
0	24	24	26	-	-	-
0.25	21	19	21	-	-	-
0.30	15	14	14	37	45	45
0.75	-	-	-	12	12	14

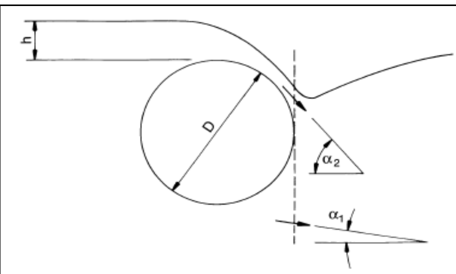

8.1.2. Initial and Boundary Conditions

The computational flow domain for a partially submerged vertical cylinder is depicted in Fig. 8.2. The mesh pattern adopted is similar to that used in the previous turbulent flow studies. Uniform velocity condition is maintained at inlet and outlet is specified with a constant pressure. No-slip boundary condition is imposed on the cylinder wall, whereas free slip conditions are imposed on the side walls of the channel. Top wall is open to the atmosphere and the bottom wall is imposed with a no-slip condition. Water and air are used as the fluids. The depth of water column is 2D whereas the height of the air column which is maintained above water is 1D. The water depth at outlet is initialized to a pressure value in order to keep the water level constant throughout the simulation.

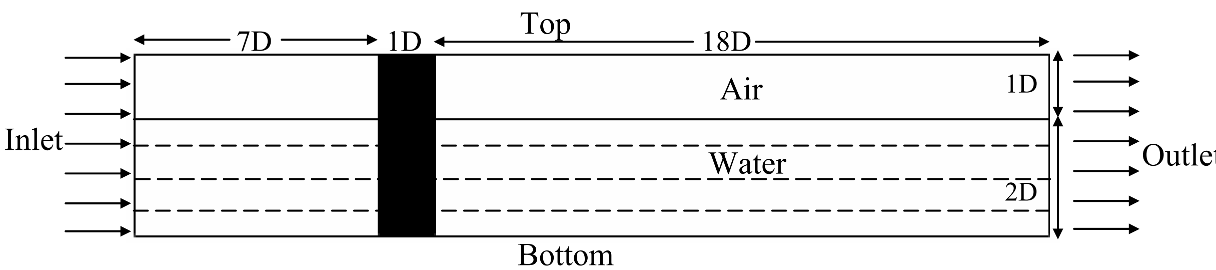

Fig. 8.2: Flow domain for partially submerged vertical cylinder.

8.2. RESULTS AND DISCUSSION

8.2.1. Flow past a Free Surface Piercing Circular Cylinder

Simulating the fluid flow features past a free surface piercing cylinder forms a good test case where dynamics of free surface interactions with the wave are typically reported. The present 3D study is further validated with the reported result of Yu et al., [149] using the standard SST k-ω model at Re = 2.7×10^4 with Fr = 0.8. All variables are non dimensionalized with respect to the cylinder diameter (D) and the free stream velocity (U_∞). The Reynolds numbers are 1.25×10^4, 1.8×10^4, 2.7×10^4 and 3.75×10^4. The corresponding Froude numbers are 0.3, 0.5, 0.8 and 1.0 respectively.

8.2.2. Grid Sensitivity Check

Towards establishing the independent nature of the solution on the grid size used in the calculations, an attempt is made to determine optimum mesh for three dimensional simulations. Fine mesh is clustered near the cylinder surface in order to capture the boundary layer and flow separation. The grid close to the interface was also refined to resolve the interface deformations. Different mesh sizes employed for the grid sensitivity study are shown in Table 8.2.

Table-8.2: Grid sensitivity study at Re = 12,500, Fr = 0.3.

Sl. No	No of Control Volumes	C_D	St	CPU time per iter
M1	7, 23,456	0.93	1.16	30 sec
M2	8,44,032	1.2	0.2	40 sec
M3	9,64,608	1.19	0.19	50 sec

It can be noticed that there exists a large difference between the values of drag coefficient and Strouhal number predicted by mesh M1 and M3 whereas the difference in 'C_D' and 'St' values between M2 and M3 is very small. But The CPU time per iterations required for M3 is large as compared to M1 and M2, thus justifying the use of the M2 mesh employed in the present study. The time step considered is 0.0001 s for all the cases. The temporal variation of forces acting on the cylinder at Re = 12,500 is depicted in Fig. 8.3.

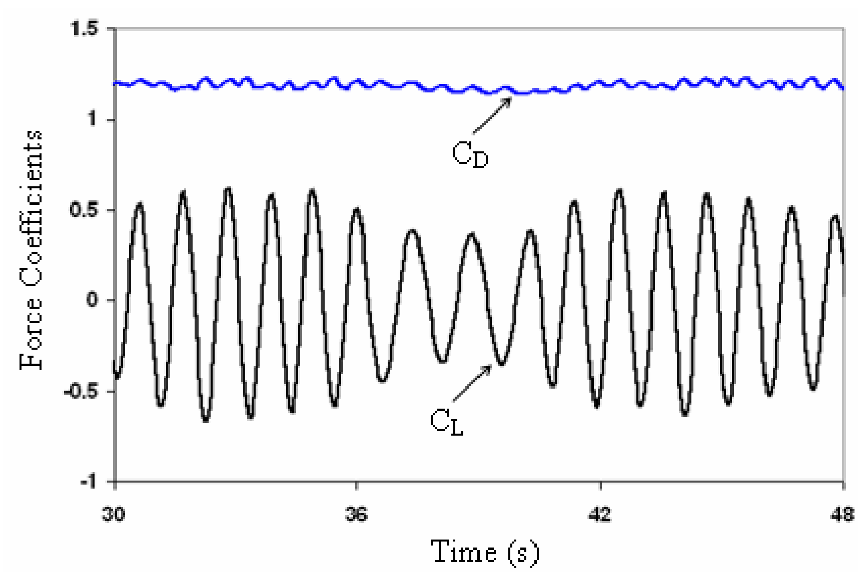

Fig. 8.3: Temporal evolution of drag and lift force coefficients at Re_D = 12,500.

In Table 8.3, the predicted Strouhal number (St), mean drag coefficient (C_D) and lift coefficient fluctuation (C_L) are compared against other experimental and numerical results. Overall, a good comparison can be seen between the present simulations with the published results.

Table-8.3: Comparison of Strouhal number, drag coefficient and fluctuating lift coefficient for flow past a circular cylinder at Re = 12,500.

Reference	C_D	C_L	St
Sampaio and Coutinho [141], Re = 10,000 (Expt.)	1.2	--	0.2
Dong and Karniadakis, [157], Re = 10,000 (Numerical)	1.143	0.45	0.203
Catalano et al., [158], Re = 12,500	1.04	--	--
Benim et al., [159], Re = 12,500	1.15	--	--
Present Simulation	1.2	0.55	0.2

8.2.3. Dynamics of Free Surface Characteristics

8.2.3.1. Interface Interactions

In this section, spatio-temporal dynamics of the wake behind the circular cylinder is investigated using mesh M2. This particular grid size is chosen after performing a detailed grid sensitivity study which was discussed in section 8.2.2. The instantaneous air–water interfaces are depicted in Fig. 8. 4 for Fr = 0.8 and Fr = 0.3. The SST k-ω is able to capture bow waves in front of the cylinder at Fr = 0.8. On the other hand, the Kelvin waves are almost unnoticeable for Fr = 0.3. The vertical structures could be captured in Suh et al., [148] primarily due to the exact simulation of large scale eddies through an SGS based LES simulation. On the contrary the RANS based simulations have a limitation in capturing small scale structures in the wake region.

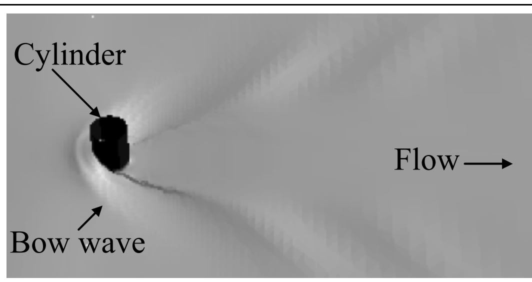	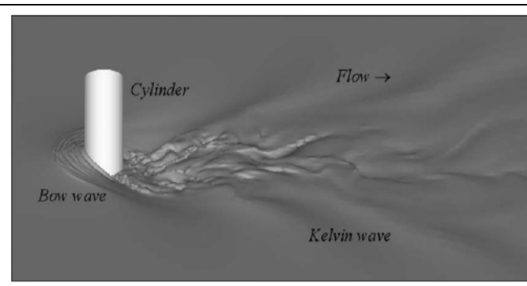
Present Simulation (Fr = 0.8) for H/D=3	Suh et al., [148] (Fr = 0.8,)
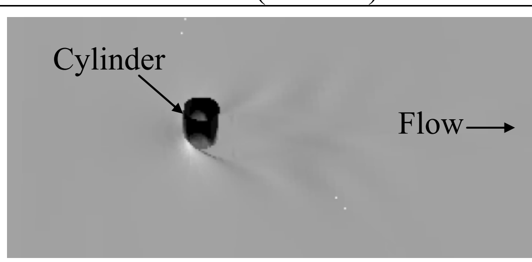	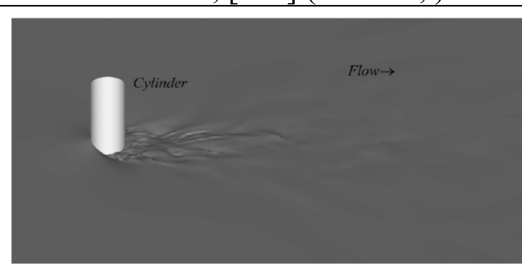
Present Simulation (Fr = 0.3) for H/D=3	Suh et al., [148] (Fr = 0.2,)

Fig. 8.4: Instantaneous water–air interface elevation.

Contours of the instantaneous vertical vorticity at different horizontal planes and the interface are presented in Fig. 8.5. Organized vortex shedding, which is very similar to that from an infinitely long cylinder in a single phase flow, is observed in the deep flow where as free surface inhibits the vortex generation near the interface, thereby reducing the vorticity and vortex shedding near the interface for all range of Froude numbers, which is evident from Fig. 8.5(c).

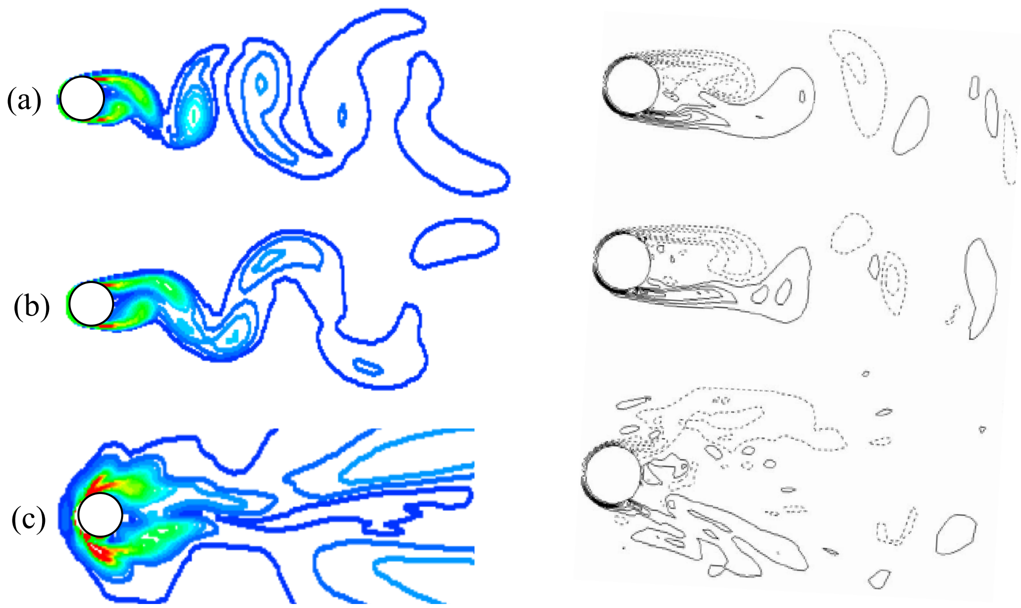

Present Simulation Yu et al., [149]

Fig. 8.5: Contours of the instantaneous vorticity magnitude for $Re_D = 2.7\times10^4$ (a) on the plane adjacent to the bed (b) at the mid plane and (c) near the free surface: (left) present simulation and (right) Yu et al., [149].

8.2.3.2. Time Average

Figure 8.6 shows the time-averaged volume fraction (α = 0.5) on a vertical plane (y = 0). A maximum bow wave height of about 0.28D above the still water level is seen in front of the cylinder. The fountain heights from the present numerical simulation agrees reasonably well with the analytical value, i.e., the maximum possible surface elevation the liquid could reach is $U^2/2g$ at low Froude numbers (up to Fr_D = 0.5). Computational results show the presence of a recirculation zone starting at the point where the surface slope changes discontinuously. Above this zone, the surface elevation fluctuates intensively. The level difference between the upstream and downstream of the cylinder is measured in terms of submergence angle made by the bow wave on the upstream of the cylinder. The measured re-submergence angle (shown in Fig. 8.6) and the corresponding free surface velocity at the interface, for various Froude numbers studied are presented in Table – 8.4.

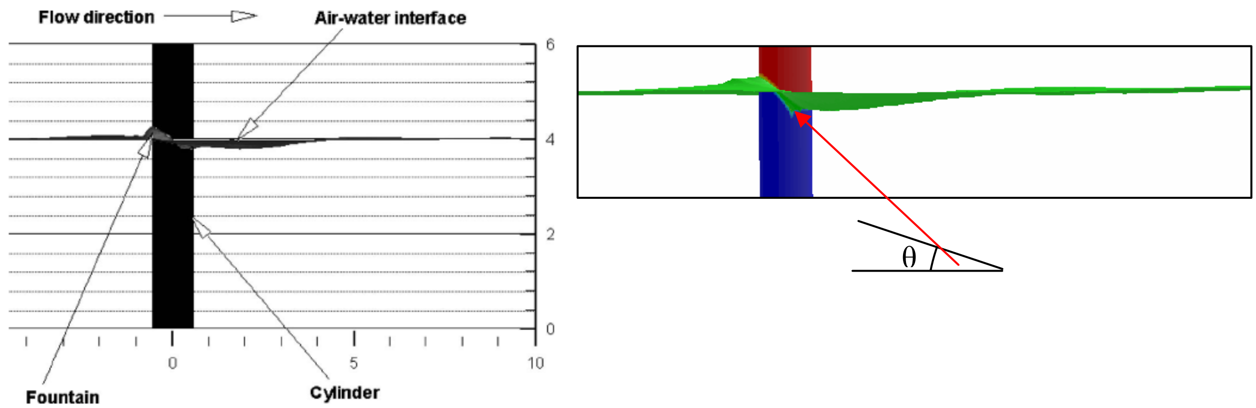

Yu et al., [149] Present Simulation (here H/D = 3)

Fig. 8.6: Time-averaged air-water interface for volume fraction of 0.5 at $Re_D = 2.7\times10^4$ (left) Yu et al [149] and (right) present simulation (total height of the cylinder is 3D).

Table-8.4: Measured submergence angles and free surface velocity at different Froude numbers.

Sl. No	Fr_D	Re_D	Resubmergence angle (degree)	Free surface velocity (m/s)
1	0.3	12,500	9°	0.33
2	0.5	18,000	11.3°	0.414
3	0.8	27,500	28.8°	0.584
4	1.0	37,500	47.7°	0.821

It is seen that, for $Fr_D \leq 0.5$, the re-submergence angle is below 12°, suggesting no risk of gas entrainment due to vortex activation. The measured free surface velocity at the interface is less than 0.42 m/s, which falls within the limit of the previous findings. Above $Fr_D > 0.5$, the value of re-submergence angle and the free surface velocity exceed the limiting values. Furthermore, increase in the intensity of level fluctuations at higher Froude numbers is prone to onset of gas entrainment. Time-averaged streamwise velocity contours at two transverse sections in the downstream of wake region (x_1 = 1D and x_2 = 2.5D from center of the cylinder) for Fr_D = 0.5 and 0.8 are depicted in Fig. 8.7.

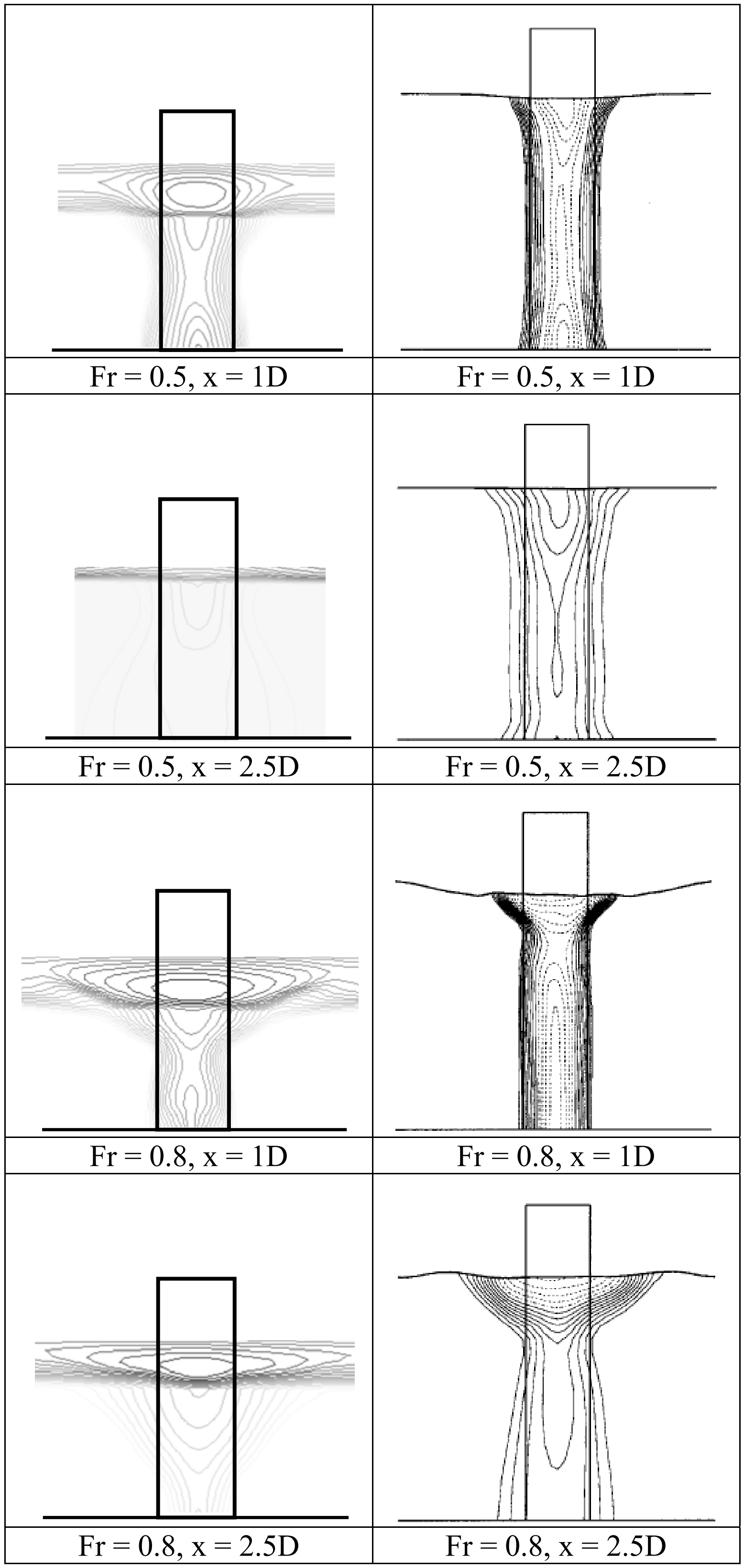

Present Simulation   Kawamura et al., [147]

Fig. 8.7: Time-averaged streamwise velocity contours at various positions

The computed velocity contours match well with the reported result of Kawamura et al., [147] at $x_1 = 1$ (x = 1D and 2.5D) for $Fr_D = 0.5$. The wake distribution is almost symmetrical at a distance of 1D from the center of the cylinder in the downstream region whereas, the wake distribution is spreading at x = 2.5D in the present simulation which is deviating from symmetry as shown by Kawamura et al., [147]. On the other hand, the lateral width of the wake increases rapidly for $Fr_D = 0.8$ demonstrating the influence of the surface deformation in the wake region.

Figure 8.8 illustrates the time-averaged pressure distribution on the plane 3.4D above the bed for $Fr_D = 1.0$. It is seen that, a negative pressure zone behind the cylinder is created. The free surface in the wake near the cylinder acts as a cavity leading to an abrupt force change on the cylinder near the free surface. Further down below the surface, a positive pressure zone builds up in the deep wake for $Fr_D = 1.0$.

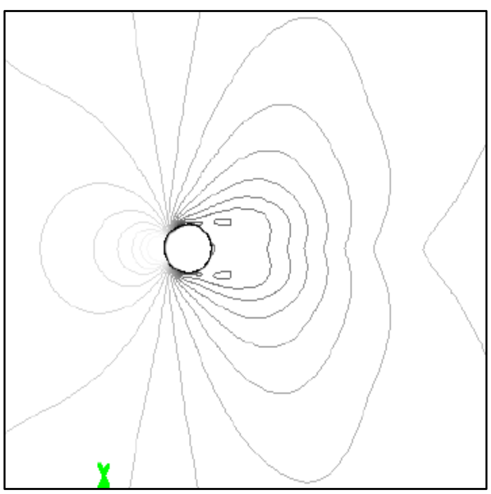

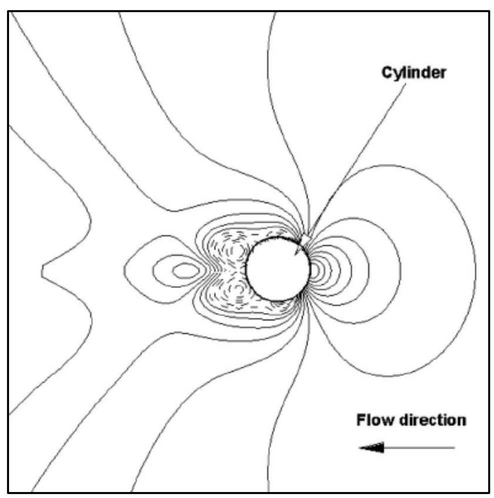

Present simulation ($Fr_D = 1.0$) Yu et al., [149] at $Fr_D = 2.0$

Fig. 8.8: Time-averaged pressure distribution on the plane 3.4D above the bed.

8.3. CLOSURE

Turbulent flow around a surface piercing circular cylinder is simulated by SST k-ω turbulence model. 3D mass and momentum conservation equations are solved to capture the air-water interface through VOF approach. Further, the flow past a cylinder located close to free surface is validated against available literature. In order to examine the influence of free surface on vortex activation, computations have been performed for various Froude numbers, Fr_D = 0.3, 0.5, 0.8 and 1.0 and the corresponding Reynolds numbers are 1.265×10^4, 1.8×10^4 2.7×10^4 and 3.75×10^4 respectively.

- Organized vortex shedding, which is very similar to that from an infinitely long cylinder in a single phase flow, is observed in the deep flow where as free surface inhibits the vortex generation, thereby reducing the vorticity and vortex shedding near the interface for the entire range of Froude numbers

- Time-averaged stream wise velocity contours at two transverse sections in the downstream of wake region show that at low Fr_D, the wake distribution is almost symmetrical whereas the lateral width of the wake increases for higher Froude numbers demonstrating the influence of the surface deformation in the wake region.

- Instantaneous air-water interface shows the formation of bow wave at high Froude number. Time average volume fraction on a vertical plane shows the presence of a recirculation zone starting at the point where the surface slope changes discontinuously.

- For various inflow velocities, the re-submergence angle and the free surface velocity at the point where the surface slope changes abruptly are measured. It is found that, for $Fr_D \leq 0.5$, there is no risk of entrainment due to vortex activation.

CHAPTER 9

CONCLUSIONS AND SCOPE FOR FUTURE STUDIES

9.0. FOREWORD

In the previous chapters, gas entrainment in the hot sodium pool of Liquid Metal Fast Breeder Reactor (LMFBR) was investigated with the aid of both 2-D and 3-D CFD models. The focus of the present study is to understand (i) liquid fall induced gas entrainment and (ii) vortex induced gas entrainment. Both fundamental and application specific problems have been analyzed and results are discussed in Chapters 4 – 8. The numerical solutions for the conservation equations have been obtained by the finite volume based CFD software FLUENT 6.3. Reynolds Stresses are modelled by employing various two equation models. Detailed grid independency tests and validation studies for the computational models have been performed. Major observations and conclusions drawn from the results of Chapters 4 to 8 are summarized below.

9.1. NUMERICAL STUDIES ON LIQUID FALL INDUCED GAS ENTRAINMENT

- Gas entrainment in pools by liquid fall induced mechanism has been numerically investigated by 2-D transient simulations on ideal hot pool models. The VOF method is employed to capture the free surface deformation. Validity of the 2-D simulation has been established through 2-D fixed grid simulation and 3-D transient VOF simulations.
- Parametric studies indicate that liquid fall induced entrainment primarily depends on free surface velocity, re-submergence angle and a modified Froude number (Fr^*).
- It is seen that gas entrainment into reactor hot pool is possible, if the value of Fr^* exceeds 2.0. The free surface velocity to avoid gas entrainment during liquid fall is found to be ~ 0.41 m/s.

9.2. IDENTIFICATION OF A PASSIVE DEVICE FOR REACTOR HOT POOL

- Following 2-D studies, 3-D CFD studies have been carried out on reference reactor hot pool and the maximum free surface velocity has been estimated to be about 1.15 m/s which is conducive to argon gas entrainment into sodium pool.

- Towards mitigating this velocity, a horizontal baffle plate has been proposed as a passive solution. A systematic study of baffle depth and width was conducted and an optimal configuration was reached.

- A baffle of 0.5 m width at a depth of 1.3 m from the free surface was found to be optimal to bring down the free surface velocity within acceptable limit. The CFD results are validated against published $1/4^{th}$ scale water model tests.

9.3. LAMINAR FLOW PAST A FINITE SIZED CIRCULAR CYLINDER MOUNTED ON A FLAT PLATE

- In order to understand the gas entrainment due to vortex activation, laminar flow past a circular cylinder mounted on a flat or accelerated bottom plate is numerically investigated. The influence of bed friction on the junction flow between the plate and the circular cylinder results in the formation of horseshoe vortex system.

- Streamwise and transverse forces on the cylinder are determined to study the finite size effects, for different liquid depths. Parametric study is conducted for cylinder aspect ratios (H/D) = 0.5, 1.0, 2.0, 5.0, and 10.0 at Re = 200.

- Vortex shedding is completely suppressed for cylinder heights below $H/D \leq 1.0$, due to interaction between the horseshoe vortex at the junction and vortex formation region of the cylinder.

- Although horseshoe vortex is present for all H/D values, the unsteady wake characteristics are not affected for $H/D \geq 2.0$, where vortex shedding still prevails at different spanwise heights.

- Accelerated bottom wall which closely resembles reactor conditions, is seen to increase the free surface velocity without affecting the vortex shedding process.

9.4. TURBULENT VORTEX SHEDDING PAST A FINITE CIRCULAR CYLINDER MOUNTED ON A FLAT PLATE

- Turbulent flow past a vertical circular cylinder mounted on a flat plate has been numerically investigated using different turbulence models for an aspect ratio of 2.

- Detailed validation studies for two dimensional flow at $Re = 5\times10^4$ has been performed. Flow characteristics, viz., Strouhal periodicities, forces acting on the cylinder, mean pressure coefficients are compared with the published data. It is found that SST k-ω model is better than other turbulence models in simulating unsteady flow at high Reynolds numbers.

- 3-D CFD studies on force coefficient, vorticity distribution around the cylinder and the spatio-temporal dynamics of interaction between the wake and the boundary-layer have been investigated.

9.5. INVESTIGATION OF GAS ENTRAINMENT IN THE HOT POOL FREE SURFACE DURING CROSS FLOW OVER A CYLINDRICAL COMPONENT

- Turbulent flow around a surface piercing circular cylinder is simulated by SST k-ω turbulence model. 3D mass and momentum conservation equations are solved to capture the gas-liquid interface through the VOF approach. Further, 2D flow past a horizontal cylinder located close to free surface is validated against available literature.

- To examine the influence of free surface on vortex activation, computations have been performed for various Froude numbers (Fr_D = 0.3, 0.5, 0.8 and 1.0). The computed results are found to be in good agreement with the published results.

- Organized vortex shedding, which is very similar to that from an infinitely long cylinder in a single phase flow, is observed in the deep flows whereas free surface is seen to inhibit the vortex generation, thereby reducing the vorticity and vortex shedding near the interface for all range of Froude numbers.

- Time-averaged stream wise velocity contours at two transverse sections in the downstream of wake region have shown that, at low Fr_D, the wake distribution is almost symmetrical where as the lateral width of the wake increases for higher Froude numbers demonstrating the influence of the surface deformation in the wake region.

- Instantaneous air-water interface shows the formation of bow wave at higher Froude number. Time average volume fraction on a vertical plane shows the presence of a recirculation zone starting at the point where the surface slope changes discontinuously.

- For various inflow velocities, the re-submergence angle and the free surface velocity at the point where the surface slope changes abruptly are measured. It is found that, for $Fr_D \leq 0.5$, there is no risk of entrainment due to vortex activation.

9.6. SCOPE FOR FUTURE WORK

The present studies focus only on liquid fall and vortex activation mechanisms of gas entrainment. Additional studies on vortex activated entrainment may be carried out to further consolidate the present findings, by adopting Very Large Eddy Simulation methods. Other mechanisms, viz., formation of drain type vortex and shear induced gas entrainment may be investigated in detail. By employing parallel CFD tools, VOF simulations may be carried out for complete reactor hot pool to enhance the understanding of complex gas entrainment phenomena. Efficacy of other types of anti gas entrainment devices other than horizontal baffle may be investigated.

REFERENCES

[1] S.C. Chetal, V. Balasubramaniyan, P. Chellapandi, P. Mohanakrishnan, P. Puthiyavinayagam, C.P. Pillai, S. Raghupathy, K. Shanmugham, C. Sivathanu Pillai, The design of the prototype fast breeder reactor, *Nuclear Engineering and Design*, **236**, 852 – 860, 2006.

[2] R.H.S. Winterton, Cover-gas bubbles in recirculating sodium primary coolant, *Nuclear Engineering and Design*, **22**, 262 - 271, 1972.

[3] K. Velusamy, P. Chellapandi, S.C. Chetal, B. Raj, Overview of pool hydraulic design of Indian prototype fast breeder reactor, *Sādhanā*, **35**(2), 97 – 128, 2010.

[4] M. Greaves, K.A.H Kobbaccy, Surface aeration in agitated vessels, *Institute of Chemical Energy Symposium Series*, **64**, H1, 1981.

[5] S. Sverak, M. Hruby, Gas entrainment from the liquid surface of vessels with mechanical agitators, *International Journal of Chemical Engineering*, **21**, 519 – 526, 1981.

[6] H. Madarame, T. Chiba, Gas entrainment inception at the border of a flow-swollen liquid surface, *Nuclear Engineering and Design*, **120**, 193 – 201, 1990.

[7] H. Kobus, *Introduction to air-water flows*, edited by I.R. Wood, IAHR Hydraulic structures design manual, A.A. Balkema Publishers, Rotterdam, Netherlands, 1991.

[8] M.R. Baum, M.E. Cook, Gas entrainment at the free surface of a liquid: entrainment inception at a vortex with an unstable gas core, *Nuclear Engineering and Design*, **32**, 239 – 245, 1975.

[9] M. Takahashi, A. Inouye, M. Aritomi, Y. Takenaka, K. Suzuki, Gas entrainment at free surface of liquid, (I): Gas entrainment mechanism and rate, *Journal of Nuclear Science and Technology*, **25**(2), 131 – 142, 1988.

[10] M.W. Clark, T. Vermeulen, Incipient vortex formation in baffled agitated vessels, *AIChE Journal*, **10**, 420 – 422, 1964.

[11] D.A. Ervine, H.T. Falvey, Behavior of turbulent water jets in the atmosphere and in plunge pools, *Proc. Institution of Civil Engineers*, **83**(2), 295 – 314, 1987.

[12] F.H. Harlow, J.E. Welch, Numerical calculation of time dependent viscous incompressible flow of fluid with free surfaces, *Physics of Fluids*, **8**, 2182 - 2188, 1965.

[13] Y. Eguchi, N. Tanaka, Experimental study on scale effect on gas entrainment at free surface, *Proc. NURETH-5*, Salt Lake City, USA, 1391 - 1398, 1991.

[14] M.R. Smith, Techniques for the investigation of scaling criteria for gas entrainment mechanisms in liquid metal cooled fast reactors, *GEC Journal of Research*, **8**, 49 - 56, 1990.

[15] C.W. Hirt, B.D. Nichols, Volume of Fluids (VOF) method for the dynamics of free boundaries, *Journal of Computational Physics*, **39**, 201 – 225, 1981.

[16] J.M. Laithwaite, A.F. Taylor, Hydraulic problems in the PFR coolant circuit, *Symposium on Progress in Sodium Cooled Fast Reactor Engineering*, IAEA, Monaco, 75 - 85, 1970.

[17] T. Hagiwara, K. Okamoto, H. Madarame, A prediction of bubble entrainment by submerging flow beneath a free surface, *Proc. FR-91*, Kyoto, Japan, 10.8.1–10.8.8, 1991.

[18] Y. Eguchi, K. Yamamoto, T. Funada, N. Tanaka, S. Moriya, K. Tanimoto, K. Ogura, T. Suzuki, I. Maekawa, Gas entrainment in the IHX of top entry loop type LMFBR, *Nuclear Engineering and Design*, **146**, 373 – 381, 1994.

[19] N. Kimura, T. Ezure, A. Tobita, H. Kamide, Experimental study on gas entrainment at free surface in reactor vessel of a compact sodium-cooled fast reactor, *Journal of Nuclear Science and Technology*, **45**(10), 1053 – 1062, 2008.

[20] M.R. Baum, Gas entrainment at the free surface of a liquid: entrainment inception at a laminar vortex, *Journal of British Nuclear Energy Society,* **13**(2), 203 - 209, 1974.

[21] S. Sakai, H. Madarame, K. Okamoto, Flow distribution around a bathtub vortex, *Proc. ICONE-3*, Japan, 583 - 588, 1990.

[22] K.H. Ardron, W.M. Bryce, Assessment of horizontal stratification entrainment model in RELAP5 / MOD2 by comparison with separate effects experiments, *Nuclear Engineering Design*, **122**, 263 - 271, 1990.

[23] T. Shiraishi, H. Watakabe, K. Nemoto, Fundamental study on gas entrainment due to vortex, *Proc. ICONE 3*, Japan, 577 - 582, 1990.

[24] H. Monji, T. Akimot, D. Miwa, Behavior of free surface vortices in cylindrical vessel under fluctuating flow rate, *Proc. 11th International Topical Meeting on Nuclear Reactor Thermal Hydraulics*, Avignon, Paper - 429, 2005.

[25] T. Ezure, N. Kimura, K. Hayashi, H. Kamide, Transient behavior of gas entrainment caused by surface vortex, *Heat Transfer Engineering*, **29**(8), 659 – 666, 2008.

[26] J. Guidez, G. Gognet, Simulation by water-test of the argon entrainment in the sodium breeder, *Proc. 2nd International Symposium on Gas Transfer at Water Surfaces*, Minneapolis, Minnesota, USA, 1990.

[27] T. Funada, K. Yamamoto, Y. Eguchi, N. Tanaka, S. Moriya, K. Tanimoto, K. Ogura, T. Suzuki, I. Maekawa, Gas entrainment in the IHX vessel of Top-Entry loop type LMFBR, *Proc. NURETH-5*, Salt Lake City, USA, 1399 - 1406. 1991.

[28] M. Miura, T. Inagaki, Y. Kumaoka, N. Nakao, T. Meshii, M. Matsuda, Present status of the DFBR conceptual design studies, *Proc. FR-91*, Kyoto, Japan, 11.5.1-11.5.11, 1991.

[29] J.C. Astegiano, C. Tenchine, B. Braquilanges, EFR primary system thermal hydraulics status on R&D and design studies, *Proc. FR-91*, Kyoto, Japan, 1991.

[30] B.H.L Gowda, B.V.S.S.S. Prasad, Gas entrainment in LMFBR phase 1: Inception of air entrainment in laboratory models, *Collaborative Research Project Report*, Applied Mechanics Department, IIT-Madras, Chennai, 2000.

[31] P. Volkart, The mechanism of air bubble entrainment in self aerated flow, *International Journal of Multiphase Flow*, **6**, 411 – 423, 1980.

[32] S. Bhattacharya, D. Hebert, M.S. Kresta, Air entrainment in baffled stirred tanks, *Chemical Engineering Research and Design*, **85**(A5), 654 – 664, 2007.

[33] R.G. Mali, A.W. Patwardhan, Characterization of onset of entrainment in stirred tanks, *Chemical Engineering Research and Design*, **87**, 951 – 961, 2009.

[34] A.P. Durve, A.W. Patwardhan, Numerical and experimental investigation of onset of gas entrainment phenomenon, *Chemical Engineering Science*, **73**, 140 – 150, 2012.

[35] R. Yahalom, J. Bennett, Gas entrainment experiments in a water model of an LMFBR outlet plenum, *Transaction American Nuclear Society*, **43**, 782 - 783, 1982.

[36] H. Chanson, Self-aerated flows on chutes and spillways, *Journal of Hydraulics Engineering*, **119**, 220 – 243, 1993.

[37] G. Govindaraj, C. Raju, R. D. Kale, G. Vaidyanathan, Gas Entrainment in surge tank of liquid metal fast breeder reactors, *Journal of Nuclear Science and Technology*, **30**, 712 – 716, 1993.

[38] T. Masuzaki, T. Fujimoto, H. Nishikawa, M. Tanji, DFBR design study on RV and IHX plenum structure from the point of thermal transients, *Proc. ICONE-4*, 227 - 238, 1996.

[39] H. Sun, Z.S. Mao, G. Yu, Experimental and numerical study of gas hold up in surface aerated stirred tanks, *Chemical Engineering Science*, **61**, 4098 – 4110, 2006.

[40] *STAR-CD (http://www.cd-adapco.com/products/STAR-CD).*

[41] M. Hori, A.J. Friedland, Effect of gas entrainment on thermal–hydraulic performance of sodium cooled reactor core, *Journal of Nuclear Science and Technology*, **7**(5), 256 – 263, 1970.

[42] H. Ueda, A. Takizawa, H. Terasaka, Y. Horikawa, N. Shirakawa, and K. Ogura, Experimental investigation on free surface movements of pool-type FBRs, *Proc. FR - 91*, Kyoto, Japan, 17.1-17.8, 1991.

[43] B. Menant, M. Villand, G. Grand, Detailed numerical studies of the thermal hydraulics in the hot plenum of a liquid metal fast breeder reactor, *Proc. NURETH-6*, Grenoble, France, 1169 - 1177, 1993.

[44] G.M. Qing, Evaluation of effects of ring plate device to eliminate free surface gradients in liquid metal fast breeder reactor vessel using multi-dimensional thermo hydraulics computer code, *Report: PNC TN9410*, Oarai Engineering Centre, PNC, Japan, 1997.

[45] K. Okamoto, H. Madarame, Fluid dynamics of a free surface in liquid metal fast breeder reactors, *Progress in Nuclear Energy*, **32,** 195 – 207, 1988.

[46] M. Iida, Numerical analysis of self-induced free surface flow oscillation by fluid dynamics computer code splash-ale, *Nuclear Engineering and Design*, **200**, 127 - 138, 2000.

[47] T. Sakai, Y. Eguchi, H. Monji, K. Ito, H. Ohshima**,** Proposal of Design Criteria for Gas Entrainment from Vortex Dimples Based on a Computational Fluid Dynamics Method, *Heat Transfer Engineering*, **29**(8), 731 – 739, 2008.

[48] K. Ito, T. Sakai, Y. Eguchi, H. Monji, H. Ohshima, A. Uchibori, Y. Xu, Improvement of gas entrainment prediction method, introduction of surface tension effect, *Journal of Nuclear Science and Technology*, **47**(9), 771 – 778, 2010.

[49] S. Moriya, Estimation of Hydraulic Characteristics of free surface vortices extension vortex theory and fine model test measurements, Central Research Institute of Electric Power Industry, *Report, No. U93004*, Tokyo, Japan, 1998.

[50] D. Tenchine, Some thermal hydraulic challenges in sodium cooled fast reactors, *Nuclear Engineering and Design*, **240**, 1195 – 1217, 2010.

[51] *PHOENICS (http://www.cham.co.uk)*.

[52] H.K Versteeg., W. Malalasekara, *An introduction to computational fluid dynamics*, **2nd** Edition, Pearson Education, 1995.

[53] *Ansys Fluent 6.3* User Guide, 2006, Ansys, Inc.

[54] W.F. Hughes., E.W. Gaylord., *Basic equations of engineering science*. McGraw-Hill, New York. 1964.

[55] C.J. Chen, S.Y. Jaw, *Fundamentals of turbulence modeling*, Taylor and Francis Publishers, Washington, 1997.

[56] M. Brewer, Large Eddy Simulation of the sub critical flow past a circular cylinder: Numerical and modeling aspects, *International Journal for Numerical Methods in Fluids*, **28**, 1281 – 1302, 1998.

[57] J.H. Ferziger, and M. Peric, *Computation methods for fluid dynamics*, Heidelberg, Springer, 1996.

[58] J. Smagorinsky, General circulation experiments with the primitive equations – I, The basic experiment, *Monthly Weather Review*, **91**, 99 – 164, 1963.

[59] D.C. Wilcox, *Turbulence modeling for CFD*, **3rd** Edition, DCW Industries, La Canada CA, 2006.

[60] B.E. Launder, D.B. Spalding, The numerical computation of turbulent flows, *Computer Methods in Applied Mechanics and Engineering*, **3**, 269 – 289, 1974.

[61] A.J. Baker, *Finite Element Computational Fluid Mechanics,* Taylor & Francis, Washington DC, 1983.

[62] J. Blazek, *Computational Fluid Dynamics: principle and applications*, Elsevier Science Ltd., Oxford, England, 2001.

[63] P.R. Spalart, Detached-eddy simulation, *Annual Review of Fluid Mechanics*, **41**, 181 - 202, 2009.

[64] E. Launder, W. Rodi, Progress in the development of a Reynolds stresses Turbulence Closure, *Journal of Fluid Mechanics*, **68**, 537 – 566, 1975.

[65] K. Shimada, T. Isihara, Application of a modified k-epsilon model to prediction of aerodynamics characteristics of rectangular cross-section cylinder, *Journal of Fluids and Structures*, **16**(4), 465 – 485, 2002.

[66] V. Yakhot, S.A. Orszag, Renormalization group analysis of turbulence-1, Basic theory, *Journal of Scientific Computing*, **1**, 3 – 51, 1986.

[67] F.R. Mentor, Two-equation eddy-viscosity turbulence models for engineering applications, *AIAA Journal*, **32**(8), 1994.

[68] M. Isshii, *Thermo-fluid dynamic theory of two-phase flow*, Eyrolles-06741 - 1, 1975.

[69] L. Chen, S.V. Garimela, J.A. Reizes, E. Leonardi, Analysis of bubble rising using the VOF method: Isolated bubbles, *HTD – National Heat Transfer Conference, ASME*, **326**, 161 - 171, 1996.

[70] K. Muralidhar, T. Sundararajan, *Computational fluid flow and heat transfer*, Narosa Publishers, New-Delhi, 1995.

[71] S. Osher, J.A. Sethian, Fronts propagating with curvature dependent speed: algorithm based on Hamilton-Jacobi formulations, *Journal of Computational Physics*, **79**, 12 – 49, 1988.

[72] J.U. Brackbill, D.B. Kothe, C.A. Zemac, Continuum method for modeling surface tension, *Journal of Computational Physics*, **100**, 335 - 354, 1992.

[72a] J.T.M. Glimm, M.J. Graham, J. Grove, X.L. Li, T.M. Smith, D. Tan, F. Tangerman and Q. Zhang, Front tracking in two and three dimensions, *Computers Math. Applic.* **35**(7), 1 - 11, 1998.

[73] W.F. Noh, P.R. Woodward, SLIC (Simple Line Interface Method), *Lectures notes in Physics*, **59**, 330 – 340, 1976.

[74] J.D. Ramshaw, J.A. Trapp, A numerical technique for low speed homogeneous two phase flow with sharp interfaces, *Journal of Computational Physics*, **21**, 438 - 453, 1976.

[75] S. Zaleski, J. Li, S. Succi, R. Scardovelli, G. Zanetti, Direct numerical simulation of flows with interfaces, *Proc. of 2nd International conference on multiphase flow*, Kyoto, April 3 - 7, 1995.

[76] D. Gueyffer, S. Zaleski, Full Navier-Stokes simulations of droplet impact on thin liquid films, *Proc. 3rd International conference on multiphase flow*, Lyon, France, Jan 8 - 12, 1998.

[77] J.C. Martine, W.J. Moyce, An experimental study of the collapse of liquid columns on a rigid horizontal plane, *Philosophical Royal Society of London*, *Series A*, **244**, 312 - 324, 1952.

[78] D.L. Youngs, Time dependent multi material flow with large fluid distortion, *in K. W. Morton and M. J. Baines (eds), Numerical methods for fluid dynamics*, Academic, New York, 273 – 285, 1982.

[79] S.V. Patankar, *Numerical heat transfer and fluid flow*, Hemisphere, 1980

[80] M. S. Annaland, N.G. Deen, J. A. M. Kuipers, Numerical Simulation Of Gas Bubbles Behaviour Using A Three-Dimensional Volume Of Fluid Method, *Chemical Engineering Science*, **60**, 2999 – 3011, 2005.

[81] C.A.J. Fletcher, *Computational techniques for fluid dynamics-2: Specific techniques for different flow categories*. Springer Publications, Verlag, 1987.

[82] S. Koshizuka, Y. Oka, Moving-particle semi-implicit method for fragmentation of compressible fluid, *Nuclear Science Engineering*, **123**, 421 - 434, 1996.

[83] D. Violeau, R. Issa, Numerical modeling of complex turbulent free-surface flows with the SPH method: an overview, International. *Journal for Numerical Methods in Fluids*, **53**(2), 277 – 304, 2007.

[84] R.W. Fox, A.T. McDonald, *Introduction to Fluid Mechanics*, **5th** Edition, John Willy and Sons, New Dehli, 2001

[85] Y.A. Cengel, *Heat Transfer-A practical approach*, **3rd** Edition, Tata Mcgrail, 2004.

[86] A. Zukauskas, R. Ulinskas, *Heat Exchanger Design Hand Book*, **2**, 2.2.4, Hemisphere Publishing Company, 1983.

[87] I. Banerjee, K. Rajesh, M. AnandaRaj, J. Venkata Ramanan, C.A. Gopal, G. Padmakumar, V. Prakash, G. Vaidyanathan, Experimental determination of coolant flow

pattern in coolant pool of PFBR using a large scale model, *Proc. 11th Int. Topical Meeting on Nuclear Reactor Thermal-Hydraulic*, Avignon, France, October 2 – 6, 2005.

[88] A.W. Patwardhan, R.G. Mali, S.B. Jadhao, K.D. Bhor, G. Padmakumar, G. Vaidyanathan, Argon entrainment into liquid sodium in fast breeder reactor, *Nuclear Engineering and Design*, 2011 (doi: 10.1016/j. nucengdes. 2011.07.046).

[89] T. Von Kármán, *Aerodynamics*, McGraw-Hill, 68 - 72, 85, 1963.

[90] J.E. Richardson, V.G. Pancheng, Three dimensional Simulation of Scour Inducing Flow at Bridge Piers, *Journal of Hydraulic Engineering*, **124**(5), 530 – 540, 1998.

[91] A. Roshko, On the development of turbulent wakes from vortex streets, *NACA-Report* 1191, 1954.

[92] M. S. Bloor, The transition to turbulence in the wake of a circular cylinder, *Journal of Fluid Mechanics*, **19**, 290 – 304, 1964.

[93] C.H.K. Williamson, Vortex dynamics in the cylinder wake, *Annual Review of Fluid Mechanics*, **28,** 477 - 539, 1996.

[94] M. Van Dyke, *An album of fluid motion*, Parabolic Press, Stanford, 1988.

[95] W.J. Davenport, Separation bubbles at high Reynolds number: measurement and computation, *PhD thesis*, Department of Engineering, University of Cambridge, 1985.

[96] C.W. Park, S.J. Lee, Free end effects on the near wake flow structure behind a finite circular cylinder, *Journal of Wind Energy and Industrial Aerodynamics*, **88**, 231 – 246, 2000.

[97] A. Slaouti, J.H. Gerrard, An experimental investigation of the end effects on the wake of a circular cylinder towed through water at low Reynolds numbers, *Journal of Fluid Mechanics*, **112**, 297 - 314, 1981.

[98] H. Eisenlohr, H. Eckelmann, Vortex splitting and its consequences in the vortex street wake of cylinders at low Reynolds number, *Physics of Fluids A*, **1**, 189 - 192, 1989.

[99] S. Szepessy, P.W. Bearman, Aspect ratio and end plate effects on vortex shedding from a circular cylinder, *Journal of Fluid Mechanics*, **234**, 191 - 217, 1992.

[100] C. Norberg, An experimental investigation of the flow around a circular cylinder: influence of aspect ratio, *Journal of Fluid Mechanics*, **258,** 287 – 316, 1994.

[101] S. Okamoto, Y. Sunabashiri, Vortex shedding from a circular cylinder of finite length placed on a ground plane, *Trans ASME, Journal of Fluid Engineering*, **114**, 512, 1992.

[102] J. Fröhlich, W. Rodi, LES of the flow around a circular cylinder of finite height, *International Journal of Heat and Fluid Flow*, **25**, 537 – 548, 2004.

[103] R. Balachandar, M.F. Tachie, V.H. Chu, Concentration profiles in shallow turbulent wakes, *Trans ASME, Journal of Fluid Engineering*, **121**, 34 - 43, 1999.

[104] V.H. Chu, J.H. Wu, R.E. Khayat, Stability of transverse shear flows in shallow open channels, *Journal of Hydraulic Engineering*, **117**(10), 1370 - 1388, 1991.

[105] H. Akilli and D. Rockwell, Vortex formation from a cylinder in shallow water, *Physics of Fluids*, **14**, 2957 – 2967, 2002.

[106] C.V. Seal, C.R. Smith, O. Akin, D**.** Rockwell, Quantitative characteristics of a laminar, unsteady necklace vortex system at a rectangular block-flat plate juncture, *Journal of Fluid Mechanics*, **286**, 117 - 135, 1995.

[107] R.L. Simpson, Junction flows, *Annual Review of Fluid Mechanics*, **33**, 415 - 443, 2001.

[108] C.J. Baker, The laminar horseshoe vortex, *Journal of Fluid Mechanics*, **95**, 347 - 367, 1979.

[109] T. Kawamura, M. Hiwada, T. Hibino, I. Mabuchi, M. Kamuda, Flow around a finite circular cylinder on a flat plate, *Bulletin of JSME*, **27**, 2142 – 2151, 1984.

[110] G. Bosch, W. Rodi, Simulation of vortex shedding past a square cylinder with different turbulence models, *International Journal of Numerical Methods in Fluids*, **28**, 601 – 616, 1998.

[111] J.C. Kalita, R.K. Ray, A transformation-free hoc scheme for compressible viscous flows past an impulsively started circular cylinder, *Journal of Computational Physics*, **228**, 5207 – 5236. 2009.

[112] G.X. Wu, Z.Z. Hu, Numerical simulation of viscous flow around unrestrained cylinders, *Journal of Fluids and Structures*, **22**, 371 - 390, 2006.

[113] P.A. Berthelsen, O.M. Faltinsen, A local directional ghost cell approach for incompressible viscous flow problems with irregular boundaries, *Journal of Computational Physics*, **227**, 4354 – 4397, 2008.

[114] T. Farrant, M. Tan, W.G. Price, A cell boundary method applied to laminar vortex hedding from circular cylinders, *Computer and Fluids*, **30**(2), 211 - 236, 2001.

[115] W. Bai, C.G. Mingham, D.M. Causon, L. Qian, Finite volume simulation of viscous free surface waves using the cartesian cut cell approach, *International Journal of Numerical Methods in Fluids*, **63**, 69 - 95, 2010.

[116] Y. Lecointe, J. Piquet, On the use of several compact methods for the study of unsteady incompressible viscous flow around a circular cylinder, *Computer and Fluids*, **12**(4), 255 - 280, 1984.

[117] C.T. Chan, K. Anastasiou, Solution of incompressible flows with or without a free surface using the finite volume method on unstructured triangular meshes, *International Journal of Numerical Methods in Fluids*, **29**, 35 – 57, 1999.

[118] M.R. Flynn, A.D. Eisner, Verification and validation studies of the time-averaged velocity field in the very near-wake of a finite elliptical cylinder, *Fluid Dynamics Research*, **34**, 273 – 288, 2004.

[119] B. Dargahi, The turbulent flow field around a circular cylinder, *Experiments in Fluids*, **8**, 1 - 12, 1989.

[120] B.M. Sumer, J. Fredsøe, *The mechanics of scour in the marine environment*, World Scientific, Singapore, 2005.

[121] K. Marakkos, J.T. Turner, Vortex generation in the cross-flow around a cylinder attached to an end–wall, *Optics and Laser Technology*, **38**, 277 - 285, 2006.

[122] R. J. Goldstein, J.Karni, The effect of a wall boundary on local mass transfer from a circular cylinder in cross flow, *Trans ASME, Journal of Heat Transfer*, **106**, 260 – 267, 1984.

[123] S. Tiwari, G. Biswas, P.L.N. Prasad, S. Basu, Numerical prediction of flow and heat transfer in a rectangular channel with a built–in circular tube, *Trans ASME, Journal of Heat Transfer*, **125**, 413 – 421, 2003.

[124] M.M. Zdravkovich, Conceptual overview of laminar and turbulent flows past smooth and rough circular cylinders, *Journal of Wind Engineering and Industrial Aerodynamics,* **33**, 53 – 62, 1990.

[125] I. Celika, F.D. Shaffer, Long time-averaged solutions of turbulent flow past a circular cylinder**,** *Journal of Wind Engineering and Industrial Aerodynamics*, **56**, 185 - 212, 1995.

[126] M. Saghafiana, P.K. Stansby, M.S. Saidia, D.D. Apsley, Simulation of turbulent flows around a circular cylinder using nonlinear eddy-viscosity modeling: steady and oscillatory ambient flows, *Journal of Fluids and Structures*, **17**, 1213 – 1236, 2003.

[127] T. Sarpkaya, Force on a circular cylinder in viscous oscillatory flow at low Keulegan–Carpenter numbers, *Journal of Fluid Mechanics*, **165**, 61 – 71, 1986.

[128] A. Travin, M. Shur, M. Strelets, P. Spalart, Detached-eddy simulations past a circular cylinder, *Journal Flow, Turbulence and Combustion*, **63**, 293 – 313, 1999.

[129] M.E. Young, A. Ooi, Turbulence models and boundary conditions for bluff body flow, *Proc. 15th Australasian Fluid Mechanics Conference*, University of Sydney, Australia 13 – 17, December 2004.

[130] B. Sahin, N.A. Ozturk, H. Akilli, Horseshoe vortex system in the vicinity of the vertical cylinder mounted on a flat plate, *Flow Measurement and Instrumentation*, **18**, 57 – 68, 2007,

[131] M.H. Tseng, C.L. Yen, C.C.S. Song, Computation of three dimensional flow around square and cylinder piers, *International Journal of Numerical Methods in Fluids*, **34**, 207 – 227, 2000.

[132] J. Paik, C. Escauriaza, F. Sotiropoulos, On the bimodal dynamics of the turbulent horseshoe vortex system in a wing-body junction, *Physics of Fluids*, **19**, 045107, 2007.

[133] C. Escauriaza, F. Sotiropoulos, Reynolds number effects on the coherent dynamics of the turbulent, horseshoe vortex system, *Journal of Flow, Turbulence, and Combustion*, **86**(2), 231 - 262, 2011.

[134] H. Persillon, M. Braza, Physical analysis of the transition to turbulence in the wake of a circular cylinder by three-dimensional Navier–Stokes, simulation, *Journal of Fluid Mechanics,* **365**, 23 – 88, 1998.

[135] S. Roh, S. Park, Vortical flow over the free end surface of a finite circular cylinder mounted on a flat plate, *Experiments in Fluids*, **34**, 63 – 67, 2003.

[136] R.J. Pattenden, E.S.R. Turnock, E.X. Zhang, Measurements of the flow over a low-aspect-ratio cylinder mounted on a ground plane, *Experiments in Fluids*, *39*, 10 – 21, 2005

[137] P. Nithiarasu, C.B. Liu, An artificial compressibility based characteristic based split (CBS) scheme for steady and unsteady turbulent incompressible flows, *Computer Methods in Applied Mechanics and Engineering*, **195**, 2961 – 2982, 2006.

[138] E. Achenbach, Distribution of local pressure and skin friction around a circular cylinder in cross-flow up to $Re_D = 5\times10^6$, *Journal of Fluid Mechanics*, **34**(4), 625 – 639, 1968.

[139] C. Norberg, Flow around a circular cylinder aspects of fluctuating lift, *Journal of Fluids and Structures*, **15**, 459 - 469, 2001.

[140] M. Breuer, Large eddy simulation of the subcritical flow past a circular cylinder: Numerical and modeling aspects, *International Journal of Numerical Methods in Fluids,* **28,** 1281 – 1302, 1998.

[141] P.A.B. de Sampaio, A.L.G.A. Coutinho, Simulating vortex shedding at high Reynolds numbers, *Proc. 10th International Offshore and Polar Engineering Conference*, Seattle, USA, May 28-June 2, 2000.

[142] E.A. Anderson, A.A. Szewczyk, Effects of a splitter plate on the near wake of a circular cylinder in 2 and 3 dimensional flow configurations, *Experiments in Fluids*, **23**, 161 - 174, 1997.

[143] W.S. Islam, V.R. Raghavan, Numerical Simulation of High Sub-critical Reynolds Number Flow Past a Circular Cylinder, *International Conference on Boundary and Interior Layers*, BAIL, 2006

[144] K. Szczepanik, A. Ooi, L. Aye, G. Rosengarten, A numerical study of heat transfer from a cylinder in cross flow, *15th Australasian Fluid Mechanics Conference,* The University of Sydney, Sydney, Australia, 13 - 17 December 2004.

[145] A.W. Lang, M. Gharib, Experimental study of the wake behind a surface-piercing cylinder for a clean and contaminated free surface, *Journal of Fluid Mechanics*, **402**, 109 – 136, 2000.

[146] M. Inoue, N. Baba, Y. Himeno, Experimental and numerical study of viscous flow field around an advancing vertical circular cylinder piercing a free surface, *Kansai Society Naval Architects*, **220**, 57–64, 1993.

[147] T. Kawamura, S. Mayer, A. Garapon, L. Sorensen, Large Eddy Simulation of a flow past a free surface piercing circular cylinder, *Trans ASME, Journal of Fluids Engineering*, **124**, 91–101, 2002.

[148] Suh J., Yang J. and Stern F., The effect of air–water interface on the vortex shedding from a vertical circular cylinder, *Journal of Fluids and Structures*, **27**, 1 – 22, 2011.

[149] G. Yu, E.J. Avital, J.J.R. Williams, Large Eddy Simulation of flow past free surface piercing circular cylinders, *Trans ASME, Journal of Fluids Engineering*, **130**, 101304, 2008.

[150] T.E. Tezduyar, M. Behr, S. Mittal, J. Liou, A new strategy for finite element computations involving moving boundaries and interfaces, *Computer Methods in Applied Mechanics and Engineering*, **94**(3), 353 - 371, 1992.

[151] J.V. Zanden, H. Simons, F.T.M. Nieuwstadt, Application of large-eddy simulation to open-channel flow, *European Journal of Mechanics B (Fluids)*, **11**(31), 337 – 347, 1992.

[152] T.G. Thomas, J.J.R. Williams, Turbulent simulation of open channel flow at low Reynolds number, *International Journal of Heat and Mass Transfer*, **38**(2), 259 – 266, 1995.

[153] M. Salvetti, Y. Zang, R. Street, S. Banerjee, Large-eddy simulation of decaying free-surface turbulence with dynamic mixed subgrid-scale models, *Proc. 21st Symposium on Naval Hydrodynamics*, Trondheim, Norway, 1018 – 1032, 1996.

[154] A.G. Kravchenko, P. Moin, Numerical studies of flow over a circular cylinder at Re_D = 53900, *Physics of Fluids*, **12**, 403 – 417, 2000.

[155] J.W. Hoyt, R.H.J. Sellin, A comparison of tracer and PIV results in visualizing water flow around a cylinder close to the free surface, *Experiments in Fluids*, **28**, 261 - 265, 2000.

[156] J. Sheridan, J.C. Lin, D. Rockwell, Flow past a cylinder close to a free surface, *Journal of Fluid Mechanics*, **330**, 1 – 30, 1997.

[157] S. Dong, G.E. Karniadakis, DNS of flow past a stationary and oscillating cylinder at Re = 10 000, *Journal of Fluids and Structures*, **20**, 519 – 531, 2005.

[158] C. Pietro, W. Meng, L. Gianluca, M. Parviz, Numerical simulation of the flow around a circular cylinder at high Reynolds numbers, *International Journal of Heat and Fluid Flow*, **24**, 463 – 469, 2003.

[159] A.C. Benim, M. Cagan, A. Nahavandi, E. Pasqualotto, RANS Predictions of Turbulent Flow Past a Circular Cylinder over the Critical Regime, *Proc. 5th International Conference on Fluid Mechanics and Aerodynamics*, Athens, Greece, August 25 - 27, 2007.

NOMENCLATURE

C_D *drag coefficient*

C_L *lift coefficient*

D *cylinder diameter*

f *vortex shedding frequency*

F_{sx} , F_{sy} *Source term in momentum equations due to surface tension force*

g *acceleration due to gravity*

h_i *inlet width of the tank*

h_o *outlet width of the tank*

H *depth of the liquid*

H *height function*

H_o *initial height of water*

ℓ_m *Prandtl's mixing length*

k *turbulent kinetic energy*

p *Pressure*

Fr^* *Non-dimensional Froude number* $Fr^* = V_{ss}\left(\dfrac{\rho}{\sigma g}\right)^{1/4}$

Re *Reynolds Number* $\left(\rho V_{in}W/\mu\right)$

R *strain rate*

St *Strouhal number,* $(fD)/U_\infty$

t *time*

t_0 *time when periodic vortex shedding is initiated*

T *vortex shedding period*

$\overline{u}$ *time average velocity*

u_i' *fluctuating velocity*

u *velocity component in x direction*

U_∞ *inlet velocity*

v *velocity component in y direction*

V_{in} *Inlet velocity*

V_{ss} *free surface velocity at start of entrainment*

W *Width of the tank*

w *velocity component in z direction*

x_i *spatial coordinate*

n *unit normal direction*

GREEK SYMBOLS

δ *boundary-layer thickness*

ε *rate of dissipation*

φ *solution variables*

η *characteristics length*

α *volume fraction*

μ *dynamic viscosity of liquid*

ν_t *turbulent eddy viscosity*

ν *kinematic viscosity*

θ_{ss} *starting angle of entrainment*

θ *angular coordinate around the cylinder*

ρ *density of the fluid*

σ *surface tension*

τ *non-dimensional time,* $\tau = \dfrac{tU_\infty}{D}$

υ *kinematic viscocity*

ω *rate of dissipation per unit energy*

ACRONYMS

2-D *two dimensional*

3-D *three dimensional*

CP *control plug*

DHX *decay heat exchanger*

FFT *fast fourier transform*

IHX *inter mediate heat exchanger*

PFBR *prototype fast breeder reactor*

PIV *particle image velocimetry*

PSP *primary stand pipe*

SA *subassembly*

PUBLICATIONS BASED ON THE THESIS

INTERNATIONAL JOURNAL

- **K. Satpathy**, K. Velusamy, B.S.V. Patnaik, P. Chellapandi, Numerical investigation of vortex shedding past a finite circular cylinder mounted on a flat plate, *Numerical Heat Transfer-A*, **59**(11), 882 – 909, 2011.

- **K. Satpathy**, K. Velusamy, P. Chellapandi, Computational fluid dynamic studies on gas entrainment in fast breeder reactors, *Energy Procedia*, **7**, 333 – 339, 2011.

- K. Velusamy, P. Chellapandi **K. Satpathy**, N. Verma, G.R. Raviprasan, M. Rajendrakumar, S.C. Chetal, A fundamental approach to specify thermal and pressure loadings on containment buildings of sodium cooled fast reactors during a core disruptive accident, *Annals of Nuclear Energy*, **38**, 2475 – 2487, 2011.

- **K. Satpathy**, K. Velusamy, B.S.V. Patnaik, P. Chellapandi, Numerical simulation of liquid fall induced gas entrainment and its mitigation, *International Journal of Heat and Mass Transfer* (Revised version submitted to the Editor).

- **K. Satpathy**, K. Velusamy, B.S.V. Patnaik, P. Chellapandi, Gas entrainment at free surface of a pool during cross flow over partially submerged component, (communicated).

CONFERENCE PROCEEDINGS

- **K. Satpathy**, K. Velusamy, P. Chellapandi, Condensation behaviour of fuel vapour in sub-cooled liquid sodium during a severe accident in a fast breeder reactor, *International Conference on Modeling and Simulation*, Coimbatore, India, 27th – 29th August 2007.

- **K. Satpathy**, K. Velusamy, P. Chellapandi, Computational fluid dynamic studies on gas entrainment in fast breeder reactors", , *2nd International Conference on Asian Nuclear Prospects (ANUP-2010)*, Mamallapuram, Chennai, India, 11th -13th October 2010.

- **K. Satpathy**, K. Velusamy, B.S.V. Patnaik, P. Chellapandi, CFD simulation of gas entrainment in a liquid pool by VOF method, *Proceedings of the 4th International*

Conference on Fluid Mechanics and Fluid Power, IIT-Madras, India, 16th - 18th December 2010.

- **K. Satpathy**, K. Velusamy, B.S.V. Patnaik, P. Chellapandi, Investigation of argon gas entrainment in liquid sodium at free surface during cross flow over cylindrical components, *IUTAM-2011*, IIT-Kanpur, India, 12th -16th December 2011.

IGCAR DESIGN REPORTS

- Condensation time and migration height of core bubble in primary sodium during a CDA, PFBR/31050/DN/1000/R-A/2010.
- Benchmarking of OpenFOAM based CFD tool: study- numerical simulation of flow around bluff bodies, PFBR/30000/DN/1106/R-A/2010.
- Effect of welding of anti-gas entrainment baffle on inner vessel, PFBR/31240/DN/1016/R-A/2010/R-A/2011.
- Optimization of anti-gas entrainment baffle attached to inner vessel, PFBR/32100/DN/1012/R-A/2011.
- Effect of manufacturing deviation in inner vessel on hot-pool thermal hydraulics, PFBR/32100/DN/1013/R-A/2011.
- Benchmarking Of OpenFOAM Based CFD Tool: Study–2, PFBR/30000/DN/1110/R-A/2012.